Technische Universität München
Fakultät für Physik

Studies of high voltage breakdown phenomena on ICRF (Ion Cyclotron Range of Frequencies) antennas

Volodymyr Bobkov

Vollständiger Abdruck der von der Fakultät für Physik
der Technischen Universität München
zur Erlangung des akademischen Grades eines
Doktors der Naturwissenschaften (Dr. rer. nat.)
genehmigten Dissertation.

Vorsitzender:	Univ.-Prof. Dr. A. J. Buras
Prüfer der Dissertation:	1. Hon.-Prof. Dr. R. Wilhelm
	2. Univ.-Prof. Dr. K. Krischer

Die Dissertation wurde am 13.02.2003 bei der
Technischen Universität München eingereicht und
durch die Fakultät für Physik am 05.05.2003 angenommen.

Abstract

Coupling of ICRF (Ion Cyclotron Range of Frequencies) power to the plasma is one of the standard methods to heat plasmas in toroidal devices with magnetic confinement. However voltage limits on the ICRF antenna used to launch the waves sometimes lead to a limitation of the power. These limits are related to a variety of high voltage breakdown phenomena in the presence of plasma that depend, in particular, on spatial charge effects and particle fluxes to the electrodes.

An ICRF probe has been developed to study the high voltage phenomena. The open end of a coaxial line models the high voltage region of the antenna. The voltage limits were studied in well defined conditions in a test facility without magnetic field and in the real conditions of the peripheral plasma of the ASDEX Upgrade divertor tokamak.

The ICRF probe was installed in the test facility and conditioned in vacuum by high power pulses to reliable operation with 60 kV, 200 ms or 80 kV, 20 ms pulses. During the conditioning, vacuum arcs occur mainly at the probe head. The arcs appear often when dark field emission currents are measured. The presence of a plasma density of 10^{15} m^{-3} (delivered by a high aperture ion source) does not affect the voltage stand-off of the probe unless the pressure of working gas is increased beyond a critical level: a semi-self-sustained glow discharge is ignited at a pressure of 0.15 Pa for He and 0.03 Pa for air. These pressures are about one order of magnitude lower than the pressures required for ignition of a self-sustained glow discharge at 80 kV. Cathode spots on the surface of the inner conductor are formed in the semi-self-sustained discharge and often lead to the formation of the arc discharge.

When the ICRF probe is installed in ASDEX Upgrade and is well conditioned (to the maximal voltages achieved in the test facility), high voltage breakdown on the probe often correlates with activity of edge localized modes (ELMs). The breakdown characteristics are similar to that of the cathode spots formation in the semi-self-sustained discharge glow discharge. The maximal RF voltage on the ICRF probe increases from shot to shot, i.e. an additional conditioning effect is observed during plasma operation. The voltage limit of the probe can be increased by application of a positive DC bias to the inner conductor while at the same time the rectified current associated with the collection of ions across magnetic field is suppressed. It was found that the appearance of ELMs and other intermittent events in the scrape-off-layer (SOL) plasma in the region of the probe head lead to a local dissipation of a high fraction of RF power.

The role of ELMs as RF breakdown trigger is confirmed by observations during operation of the full-size AUG ICRF antenna. A reliable arc detection system is required for the ICRF antennas (not every breakdown triggered by ELMs is easy to detect), otherwise the overall performance of the antennas degrades due to appearance of quasi-stationary arc discharges. The antennas operates more reliably when the antenna conductors are conditioned with plasma.

Measures to improve the antenna voltage stand-off in the presence of plasma are suggested: an optically closed Faraday screen; glow discharge conditioning; a form of antenna conductors to minimize ion collection across the magnetic field and minimize asymmetry of electrodes along the field; neutral density reduction inside the antenna. Further work should be focused on the choice of the antenna materials, parasitic absorption of the RF power and the antenna-plasma interaction for different DC boundary conditions of the antenna circuit.

Contents

Chapter 1

Introduction

The reduction or complete substitution of energy produced from fossil fuels needs reliable alternatives. Nuclear fusion, in particular, *thermonuclear fusion*, is one of the most promising candidates despite the fact that further research and development is needed.

1.1 Fusion research

The so-called mass-defect is the difference between the sum of the masses of the isolated protons and neutrons and the mass of a nuclei formed by the same number of the protons and neutrons. The mass defect increases when the mass number of the nuclei is increased for a range of mass numbers below 62 and decreases for a range of mass numbers above 62. Therefore fusion of light nuclei or fission of heavy nuclei leads to an increase of the mass defect. According to the equivalence of mass and energy, the change in mass-defect represents an energy which is released during the reaction.

To initiate fusion of two nuclei, the nuclei have to overcome the Coulomb repulsive forces to come as close to each other as required for the short-range nuclei attraction forces to act. The Couloumb potential barrier is proportional to the product of the nuclei charge numbers. This makes fusion of the nuclei with low charge numbers easier [2, 3, 4].

The reactions of interest for the controlled nuclear fusion are:

$$\begin{aligned} D + D &\rightarrow He^3 + n + 3.27 \text{ MeV}, \\ D + D &\rightarrow T + H + 4.05 \text{ MeV}, \\ D + He^3 &\rightarrow He^4 + H + 18.34 \text{ MeV}, \\ D + Li^6 &\rightarrow He^4 + He^3 + 4 \text{ MeV} \end{aligned}$$

The power released as a result of a fusion reaction is proportional to a reaction rate coefficient $\langle \sigma_{fus}\ v \rangle$ [2, 3] which is maximal for the following reaction for temperature range from 1 keV to 100 keV:

$$D + T \rightarrow He^4 + n + 17.58 \text{ MeV} \tag{1.1}$$

The reaction rate coefficient has a certain temperature dependence. For the *D*-*T* (deuterium-tritium) reaction it has a maximum at a temperature of about 60 keV.

The first reaction product of (1.1) He^4 (α-particle) is completely inert. Furthermore the energy of the α-particles can be used to sustain fusion reaction (see next section). The second product of (1.1) are fast neutrons which are collected by a blanket around the plasma [2, 3]. Neutrons heat the blanket and the heat can be converted into electricity. However the first wall of the fusion device can be activated by energetic neutrons. To minimize the negative influence of neutrons, low-activation materials should be used in the blanket. There exists a positive aspect of the neutron production: neutrons from the D-T reaction can be used for the production of T in a tritium breeding blanket by reacting with Li (lithium):

$$\begin{aligned} Li^6 + n &\rightarrow T + He^4 + 4.8 \text{ MeV}, \\ Li^7 + n &\rightarrow T + He^4 + n - 2.5 \text{ MeV}. \end{aligned}$$

D and Li can be isolated from seawater in significant amounts. Therefore there would be no problem to get easily accessible and cheap resources. Also for environment there is no CO_2 production and no danger of an uncontrolled reactor. The products of fusion reactions are not radioactive. The radioactive waste can come from the activation of the walls of a fusion reactor but is much smaller than that for a fission reactor.

1.2 Fusion of energetic particles

There are three main parameters describing the efficiency of a fusion device:

1. energy of the reacting particles, should be high to overcome the Couloumb barrier *in thermonuclear fusion, particles get energy by increasing of temperature of plasma (at the required temperatures matter is in plasma state)*;

2. density of the plasma particles n (power released as a result of fusion reactor is dependent on n^2);

3. energy confinement time τ_E (introduced by Lawson [1] for a pulsed fusion device), a characteristic timescale of the loss of energy carried by the plasma particles after external energy sources are switched off.

Different concepts of fusion device rely either on pulsed or steady-state operation. In pulsed systems the conditions to get fusion reaction started should be achieved for each pulse. Therefore every pulse should produce enough fusion to cover the energy costs for the plasma build-up. For sufficiently long operation the primary plasma energy input obviously becomes negligible. Nevertheless also a steady-state system may require a permanent power input from external sources.

For simplicity we describe a steady-state system. For convenience one introduces Q, a ratio of power of the fusion products P_{fus} to the power P_{ext} used for the plasma heating:

$$Q_{fus} = \frac{P_{fus}}{P_{ext}} \tag{1.2}$$

The condition:

$$Q_{fus} = 1 \tag{1.3}$$

is defined as the so-called "break-even" – when the power released during the fusion reactions in plasma becomes equal to the power delivered to plasma by external heating systems.

To get an idea about values of Q_{fus} required for total production of power we introduce an efficiency of energy conversion from fusion energy to electric energy $\eta_{\ thermal}$ and an efficiency of conversion from electric energy to energy delivered by heating systems $\eta_{\ ext}$. The total efficiency of conversion of the fusion power to electricity $\eta_{\ total}$ is given by:

$$\eta_{\ total} = \eta_{\ thermal} - \frac{1}{Q_{fus} \cdot \eta_{\ ext}} \tag{1.4}$$

The efficiency $\eta_{\ thermal}$ has typically values of 0.3 to 0.4. Value of $\eta_{\ ext}$ depends on the type of the fusion device and heating systems used. For equality of the energy produced in the fusion device that is converted into electricity and the energy consumed by the heating systems ($\eta_{\ total} = 0$), $Q_{fus} \approx 10$ is required for systems with magnetic confinement while $Q_{fus} \approx 100$ is required for systems with inertial confinement and laser heating.

Only 20% of the fusion energy released from a single fusion reaction goes to the energy of α-particles ϵ_α while 80% of the energy is carried by neutrons (e.g. for $Q_{fus} = 1$ α-particle power $P_{\alpha,fus}$ constitutes 20% of the heating power P_{ext}). The concept of a steady-state fusion device deals with the so-called ignition or burn condition. This means that the fusion reaction is self-sustained, i.e. the required temperature of fuel is sustained solely by α-particles heating. The power balance in the steady-state fusion device can be written as:

$$P_{\alpha,fus} + P_{ext} = P_{loss} \tag{1.5}$$

where P_{loss} is the power of losses from the plasma characterized by the empirical energy confinement time τ_E. For the burn condition $P_{ext} = 0$ (or $Q_{fus} = \infty$) and:

$$P_{\alpha,fus} > P_{loss} \tag{1.6}$$

For a 50% mixture of deuterium and tritium one gets the condition:

$$\frac{1}{4}\ n_i^2\ \langle \sigma_{fus}\ v \rangle\ \epsilon_\alpha V > 3 n_i T_i V / \tau_E \tag{1.7}$$

where n_i is the density of the deuterium/tritium mixture, T_i – temperature, V – volume where the reaction takes place, ϵ_α – energy of α-particle produced by the fuion reaction. The expression is transformed to:

$$n_i\ \tau_E > \frac{12}{\langle \sigma_{fus}\ v \rangle} \frac{T_i}{\epsilon_\alpha} \tag{1.8}$$

Within 10% accuracy one can represent the reaction rate in the temperature range 10-20 keV as: $\langle \sigma_{fus}\ v \rangle \approx 1.1 \cdot 10^{-24} \cdot T_i^2$ m^{3}s^{-1} (T_i in keV). Using $\epsilon_\alpha = 3.5$ MeV one gets an approximate condition for ignition:

$$n_i\ T_i \tau_E > 3 \cdot 10^{21}\ \ \mathrm{m}^{-3}\ \mathrm{keV\ s} \tag{1.9}$$

Getting condition (1.9) we assumed that temperature and density are the same for the whole volume where the fusion reaction takes place.

Even if ignition is not achieved, the conditions for total power production may be achieved when Q_{fus} is sufficiently high. The total energy conversion efficiency (1.4) should be as close to the efficiency of fusion energy conversion $\eta_{\ thermal}$ as possible. There are different experimental approaches which are distinguished by types of particle confinement and heating systems.

Inertial confinement fusion

The inertia of the fuel mass provides confinement.

1. *Fusion in colliding beams.* Nuclei of D or T can be accelerated to the required energies by standard particle accelerators, e.g. Van de Graaf generators. The two beams can fire at each other (or one beam at a target) to achieve fusion. However the probability of particle scattering is thousands times greater than that for particles to fuse. The scattered particles represent an energy loss which can not be recovered from fusion reactor. Also the energy density produced by such a reactor is too low for practical interest.

2. *Laser fusion and ion fusion.* In these systems [5, 6] the conditions for the thermonuclear burn are achieved by bombarding a target (a $D-T$ pellet) by a laser beam or beam of ions. Fueling is realized via repetitive usage of many targets, i.e. this type of systems are pulsed. The target is a capsule with frozen or liquid deuterium-tritium. The target should be symmetrically compressed by implosion process to the conditions of high energy and temperature and very high density (≈1000 times the density of liquid $D-T$). The confinement times are of the order of nanoseconds. This leads to the high power requirements of the "driver" (beam) systems which should deliver more than 1 MJ of energy during the confinement time. Because of low efficiency of driver systems, in particular laser heating systems: $\eta_{\ ext} < 0.1$, the so-called target gain (that is actually an analog of Q_{fus} in terms of energy) is required to be higher than 100 to achieve positive energy gain. Use of particle accelerators to heat the target can improve the efficiency: $\eta_{\ ext} = 0.2 - 0.35$. There are two approaches to optimize target gain: a direct drive - where a target is directly bombarded by laser beam or ion beam and heated; an indirect drive - when the energy from beams is first absorbed by a high-Z enclosure and up to 80% of it is converted to the energy of X-rays which drive the implosion. During the last decade a large progress has been made in understanding the underlying physics of inertial confinement and targets with high gain have been designed. Experiments are planned, in particular at the National Ignition Facility, U.S.A., to reach ignition and fusion power P_{fus} >100 MW during a quasi-steady-state operation (repetition frequency of ≈ 10 Hz).

Fusion in magnetically confined plasma

A different approach is confining plasma in a magnetic field. From a variety of systems using the principle of magnetic confinement, toroidal systems have proven to produce the most successful results. In these machines, namely of a *tokamak* [3, 7, 2] and a *stellarator* [8, 2, 9] type, the confining magnetic field in the torus is obtained by superposition of toroidal and poloidal field components. For good confinement the magnetic field lines need to create nested magnetic flux surfaces. In the stellarator the magnetic field is completely created by external coils: either by helical coils or by toroidal coils with a complicated three-dimensional form. In the tokamak the toroidal field coils form the main toroidal magnetic field and the poloidal field is created by the toroidal plasma current induced by the ohmic-heating (OH) transformer.

According to the condition (1.9), plasma densities of 10^{20} m^{-3} and ion temperatures of about 10-20 keV and energy confinement time of few seconds are required to initiate ignition in both types of machines. Up to now the required densities, temperatures and confinement times have been obtained but not simultaneously. In general, tokamaks have come closer to ignition conditions than stellarators and the experimental part of this thesis was made on the tokamak ASDEX Upgrade. Therefore we concentrate mainly our description on results from the operation of tokamaks.

Achievement of the required density in tokamaks is often limited by an empirical "Greenwald density limit" [10, 11]. Many tokamaks including ASDEX Upgrade can operate at densities about $1 \cdot 10^{20}$ m^{-3}. However ion temperatures at this density are relatively low. On the other hand ion temperature of up to 30-40 keV can already be reached in tokamaks but at lower densities. In the experiments at the Joint European Torus (JET) in England [12] in D and T mixture, $Q_{fus} = 0.62$ was achieved. This value corresponded to the produced fusion power P_{fus} = 16 MW. The next-step device - ITER (International Thermonuclear Experimental Reactor) [13] is a tokamak and is designed to reach Q_{fus} >10. This will demonstrate that a positive total energy gain (i.e. $\eta_{\ total} > 0$) is achievable. For an economically efficient fusion reactor $Q_{fus} > 40$ is required.

The magnetic confinement fusion is one of the most successful principles aiming for the prototype of the future nuclear fusion power station [14].

1.3 Tokamak concept and plasma heating

The scheme of a tokamak is illustrated in Fig. 1.1. In addition to toroidal field coils and an OH-transformer, vertical field coils are installed for plasma positioning and shape control. The induced plasma current produces a poloidal magnetic field. Magnetic flux surfaces are formed by magnetic field lines.

The shape of the magnetic flux surfaces may have a "limiter" or a "divertor" configuration. In the limiter case the outer boundary of the plasma is defined by wall structures of the vacuum chamber - limiters. Divertor configurations allow to divert the magnetic field lines at the plasma boundary away from the plasma core by modification of the magnetic field. That helps to solve the problem of particle and energy exhaust. The boundary between the confined and edge plasma is called *separatrix.*

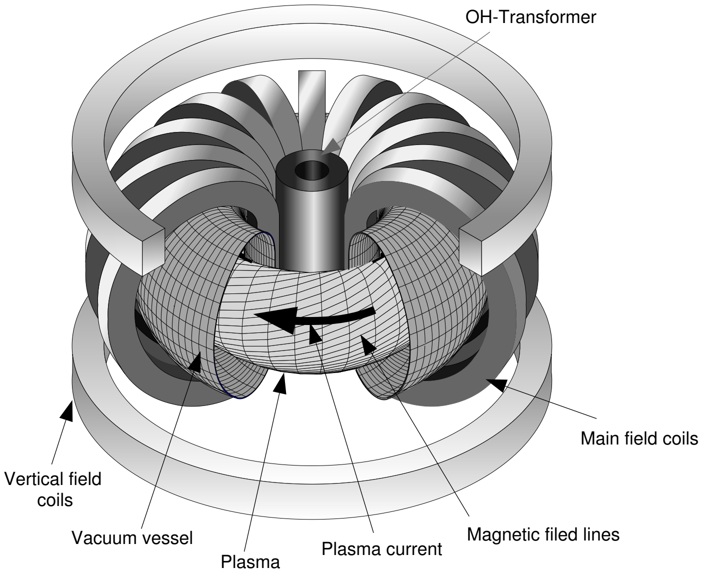

Figure 1.1: *Scheme of a tokamak and magnetic field configuration.*

Particle motion

The basic principles of particle movement are shown in Fig. 1.2. The charged particles in a magnetic field move along the magnetic field lines and have a circular orbit in the plane perpendicular to the field lines. The radius of the orbit is called gyroradius.

The toroidal magnetic field created by external (poloidal) coils is non-uniform and is decreasing from the center of the torus to the outer wall (low-field side). Therefore if only the toroidal field is present, a vertical drift of particles appears having opposite directions for different charge polarity. The separated charges produce a vertical electric field which results in an additional drift of the plasma radially towards the low field side. The scheme of this charge separation and the plasma drift is illustrated in Fig 1.2a.

To avoid the radial plasma drift, a poloidal component of the magnetic field is created by a toroidal plasma current (Fig. 1.2b). The magnetic lines connect top and the bottom sides of the torus. Since the plasma has high electrical conductivity along the magnetic field lines, the regions of different excess charges are short circuited, thus the vertical electric field is reduced and the radial drift is decreased.

A particle moving in a non-uniform magnetic field changes the distribution of its energy between the velocity perpendicular and velocity parallel to the magnetic field depending on the magnitude of the field. The parallel velocity decreases when particle goes to the high field side. Therefore particles having high initial parallel velocity may pass the high field side and circulate continually around the torus. These are called *passing*. The particle with initially low parallel velocity are reflected to the low field side and are *trapped*. The trajectories of guiding centers (centers of gyromotion) of a passing and a trapped particles are shown in Fig. 1.2b. The diagrams for the movement projected into the poloidal plane are shown in the right part of the figure. The trapped particles

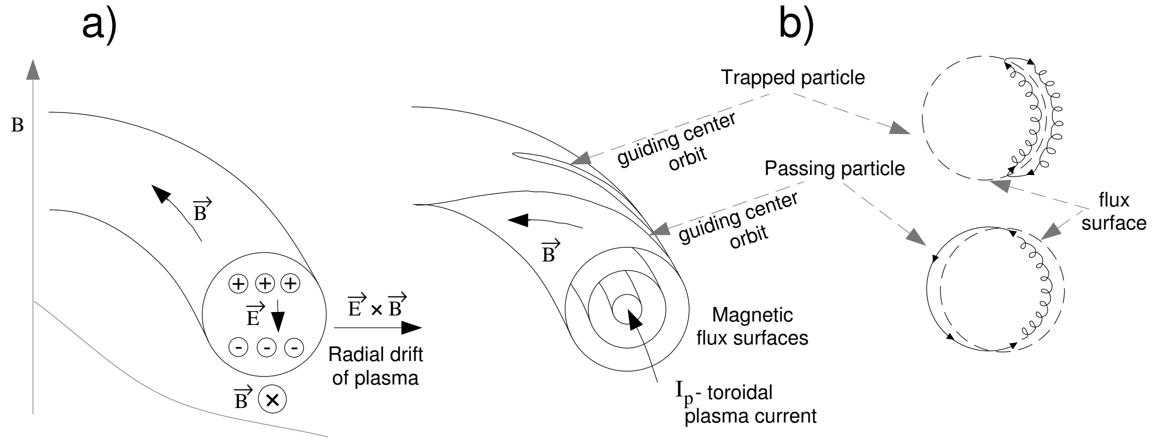

Figure 1.2: *Main particle motion in a tokamak: a) only toroidal magnetic field, b) in the presence of toroidal and poloidal magnetic fields.*

move along the so-called *banana* orbit. The presented picture of particle movement is realized when collisions are rather rare, so passing particles make more than one toroidal turn and trapped particles execute more than one banana orbit before they collide with other species.

Heating systems

For a fusion reactor, in particular based on the tokamak principle, the heating systems [2, 3] are important for:

1. initial heating to ignition temperatures (condition (1.9));
2. control and stabilization of the **reactor operation**:
    - drive of a non-inductive toroidal current for a steady state operation of tokamak: current drive (CD);
    - burn control and control of the plasma confinement;
    - stabilization of magnetohydrodynamic (MHD) instabilities;

In most present experiments the achieved fusion power is negligible compared to the heating power. Therefore it is important to simulate the conditions at which fusion reactors will operate. Use of the heating systems in the **fusion experiments** allows to:

- sustain plasma at reactor relevant parameters;
- simulate α-particle heating to get a valuable experience for operation of the future fusion reactors;
- conduct studies of transport properties of plasma;

- test systems for stabilization of MHD instabilities, current drive and avoidance of impurity accumulation in the central plasma.

The plasma heating in magnetically confined plasmas is realized by using heating systems which may be classified as follows:

1. ohmic heating
   joule heating by the induced toroidal current in tokamaks; usually not sufficient to reach ignition conditions;

2. injection of energetic neutrals into plasma
   the heating is accompanied by fuelling of plasma, at low energies of injection predominantly ions are heated, at higher - electrons;

3. heating by launching waves in different frequency ranges into plasma (*no fuelling of the plasma*), the most important ones are:
   (a) electron cyclotron range of frequencies
   electrons are heated;
   (b) lower hybrid range of frequencies
   typically electrons are heated;
   (c) Ion Cyclotron Range of Frequencies (ICRF)
   ions and electrons are heated (depending on scenario).

In fusion reactors working in the conditions when the power of the external heating amounts to a small fraction of produced fusion power, it will unfortunately not be possible to provide a central plasma fuelling. Therefore for a correct simulation of the reactor operation a heating system without particle input should be used. α-particles in the reactor heat mainly electrons. Since α-particle heating power density is proportional to the fusion reaction rate $\langle \sigma_{fus}\, v \rangle$, and therefore to T_i^2, the heating profiles are peaked. Thus for the correct simulation of α-particle heating a central electron heating is required, e.g. electron-cyclotron or ICRF heating. In addition to electron heating, ICRF heating produces energetic ions which firstly, can help to reach ignition parameters, and secondly allow to model existence of fast α-particles and α-particle heating simultaneously.

Let us describe basic principles and problems of ICRF heating.

1.4 Heating of plasma with ICRF

Frequencies

Ion cyclotron frequency or ion gyrofrequency is the frequency of rotation of an ion in a magnetic field (gyromotion) in the plane perpendicular to the magnetic field direction and is given by:

$$\omega_c = \frac{Z_i e B}{m_i} \tag{1.10}$$

where Z_i is ion charge number, e is the elementary charge, m_i is ion mass. The frequency range used for operation in the magnetic fields typical for the fusion devices with magnetic confinement is typicaally from 20 (fundamental frequency of H at 1.3 Tesla) to 120 MHz (second harmonic of H at 4 T). The vacuum wavelength of RF waves at these frequencies is $\lambda = 15$ m and $\lambda = 2.5$ m respectively.

Principle of heating

The heating principle relies on the excitation of the waves at the plasma edge that propagate into the plasma [3, 15]. The power of the waves is absorbed inside the plasma. Two types of waves can be used for the heating [15]:

- slow wave (shear Alfvén wave)
  exists only on one magnetic flux surface defined by generator frequency, magnetic field and plasma density and propagates tangentially to that surface, damped on the electrons;

- fast wave (compressional Alfvén wave)
  propagates across magnetic flux surfaces, can be damped on the ions if its polarization coincides with rotation of ions around magnetic field lines, can be damped on the electrons at high electron temperatures due to small but finite parallel (to magnetic field) electric field.

Heating by fast waves is used often in the so-called *minority heating* scenario. Heating of ions requires left-hand polarization of the electric field. When one has a plasma of one sort of ions, the fast wave at the fundamental frequency is right hand polarized and the wave is poorly absorbed in the ion cyclotron resonance layer. To overcome the problem of polarization, it is possible to fill in a small fraction of another sort of ions (minority ions) and use fundamental frequency for this sort of ions. The polarization is mainly determined by majority ions while at the resonance layer for minority ions the wave contains a right hand polarized component and the minority ions absorb energy efficiently.

There are also other heating scenarios involving, e.g. a heating by fast waves on the second harmonic or a conversion of the fast wave into ion-Bernstein wave (an electrostatic wave that is efficiently damped on electrons) in the region of ion-ion hybrid resonance when the concentration of the second sort of ions is relatively high. The minority heating (e.g. by minority hydrogen in deuterium plasmas) has become a routinely used ICRF heating scenario due to its relative simplicity and reliability.

Typically the fast wave is launched by an antenna that situated at the low field side of a tokamak (see Fig. 1.3 showing ICRF antenna in ASDEX Upgrade). The electromagnetic fields corresponding to the fast wave field are excited by one or many poloidal straps. Use of a Faraday screen with rods oriented along the external magnetic field reduces electric field of the waves along the magnetic field and therefore reduces the excitation of slow waves.

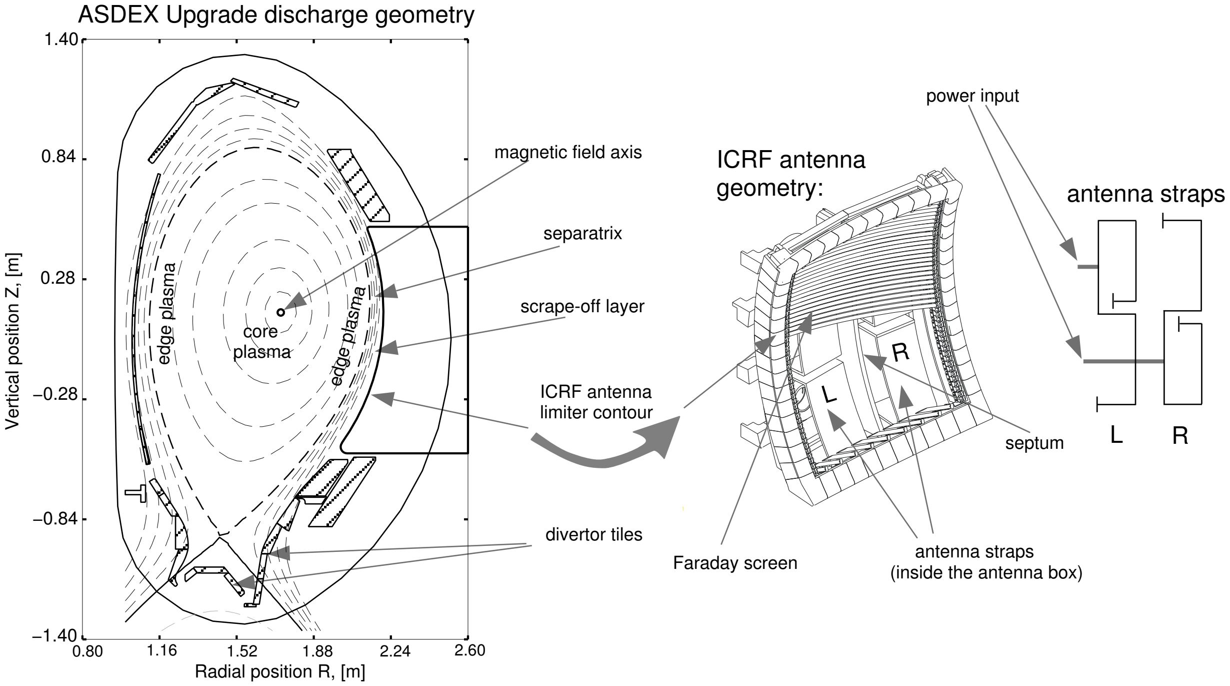

Figure 1.3: *Geometry of ICRF antennas on ASDEX Upgrade*

ICRF system at ASDEX Upgrade

The geometry of the ASDEX Upgrade experiment and the ICRF antennas is shown in Fig. 1.3. The antenna includes two current-carrying straps (the right part of the figure shows that each strap consists of two loops) made of stainless steel and separated by a septum. The straps are mounted in an antenna box with a back plate playing a role of the RF return conductor (behind the straps in Fig. 1.3). Limiters (plasma facing graphite tiles, see the antenna limiter contour in the figure) protect the stainless steel and copper components from the plasma. A Faraday screen is constructed from molybdenum rods typically with TiC coating on the rods.

The strap is grounded and has a length from $\lambda/8$ to $\lambda/4$ depending on the frequency of operation. This means that a spatial distribution of RF voltage exists along the strap. For this reason a range of the voltages is present on the antenna strap, starting from zero at the position of the ground to a maximum at the side where it is connected to the transmission line.

The plasma geometry in Fig. 1.3 corresponds to AUG discharges of a special plasma shape, the so-called edge optimized configuration (EOC) characterized by relatively small distance (from 2.5 to 4 cm) between the separatrix and the antenna limiter along the antenna contour. This plasma shape fits the antenna contour relatively well. Many plasma discharges of ASDEX Upgrade which were performed during this work used the EOC plasma shape.

1.5 Power limitations of ICRF antennas

To start propagating in the magnetically confined plasma, the wave must tunnel through an evanescent region between the antenna and the radial position where plasma density reaches approximately $2 \cdot 10^{18}$ m^{-3}. Thus for a good *coupling* of the RF power to the plasma a small distance between the edge plasma and the ICRF antenna is required. The coupling is characterized by a coupling resistance R_0.

The plasma density in front of the antenna and the density profile is very important for coupling. However even if the plasma shape allows for closeness to the antenna, one has to design a large area ICRF antenna to achieve the coupling resistance of a few Ω. For ASDEX Upgrade ≈ 1 m^2 ICRF antenna typical coupling resistance of $\lesssim 4\ \Omega$ are measured.

The power coupled to the waves excited by a two-strap antenna and propagated to plasma is determined by a formula:

$$P = \frac{R_0}{2Z_0^2} V^2 \tag{1.11}$$

where Z_0 is the characteristic impedance of a transmission line, R - the coupling resistance, V - the peak value of the maximum voltage on the transmission line. One can see that for a given R_0, an increase of the coupled power should be made by an increase of voltage, furthermore the dependence on the voltage is quadratic. For example, for ASDEX Upgrade antennas the resistance of 2 Ω and delivery of 2 MW power to plasma correspond to a voltage on the transmission line of 25 kV. Since for typical frequencies used for ICRF heating the antenna strap length is somewhat larger than $\lambda/4$, the corresponding voltage on the antenna straps is a few kV less than 25 kV. The voltage on the ASDEX Upgrade antenna is presently limited for reliable operation to about 20-25 kV. Higher voltages should allow higher power and thus higher power densities.

Therefore *voltage stand off, i.e. the maximum voltage sustained without a breakdown, is an important issue to increase the power launched on the antenna and/or to decrease an area occupied by the ICRF launchers in the fusion devices with magnetic confinement.*

In experiments it is often observed that the maximal voltage on the antenna is affected by the presence of plasma. The plasma conditions in the region of the ICRF antenna in the fusion device are very specific due to complex stationary and transient processes which take place at the plasma boundary.

Specific conditions of the scrape-off-layer (SOL) plasma

As the confinement of plasma is not ideal, particles and heat are transported across the magnetic field. The total transport in the devices with magnetic confinement has three contributions [3]:

1. neo-classical, it is subdivided into three regions depending on the frequency of electron-ion collisions:

   (a) *low collisionality banana regime*, the particles move as described in 1.3, the trapped particles are displaced by the width of the banana orbit due to a collision and contribute to transport dominantly, diffusion grows with collisionality;
   (b) *highly collisional regime*, transport is defined by resistive plasma diffusion in torus, the collisions are so frequent that the trapping of particles is negligible, diffusion grows with collisionality;
   (c) *plateau regime*, a transition region from low to high collisionality regimes, is characterized by an approximately constant diffusion coefficient;

2. *turbulent*, is associated with the appearance of instabilities, not yet well understood;

3. *ripple losses*, the losses caused by particles toroidally trapped in a magnetic field ripple between toroidal field coils.

The neo-classical transport is higher than transport described by the classical diffusion - a diffusion across the magnetic field in a cylindrical plasma where diffusion coefficient is defined by collision time and gyroradius (the latter is the appropriate scale of particle displacement after a collision in the classical case). However the measured diffusion coefficients are usually even higher than neo-classical, mainly due to the anomalous transport. In the tokamak different instabilities may be observed which lead to the anomalous transport and are described by magneto-hydrodynamic and kinetic theory. The instabilities lead to the changes of effective transport coefficients in the core of plasma and at the plasma edge leading to losses of particles and heat from the region of confined plasma.

Thus the edge instabilities affect the plasma density profile. Since the plasma density profile is an important parameter for coupling of waves by the ICRF antenna, the instabilities affect the efficiency of launching the waves into the plasma. The instabilities may produce plasma formations (blobs) [16, 17] which can penetrate fast into the tokamak scrape-off-layer and to the antenna. One of the experimentally observed instabilities is the so-called edge localized mode (ELM, see section 5.3 of this thesis for a more detailed description). When this instability takes place, the plasma boundary is distorted in a way that is analogous to the distortion during formation of plasma protuberances on the sun. Strong turbulent particle fluxes, electric and magnetic fields interact and dense, hot plasma formations can be ejected from the main plasma boundary.

Therefore, due to uniqueness and complexity of the processes occurring at the plasma edge of tokamak, it is impossible to reproduce the real plasma conditions in a small laboratory experiment. For this reason the real plasma conditions of the plasma boundary of the fusion device with magnetic confinement (in our case - tokamak ASDEX Upgrade) are essential for the experimental studies of high voltage breakdown phenomena on the ICRF antennas.

1.6 Outline of the thesis

The main subject of this doctoral thesis is the study of the correlation between the plasma conditions and high voltage breakdown on the ICRF antenna. In chapter 2 we discuss the main aspects of the physical description of the phenomena which may take place in the presence of plasma and high RF voltage. Chapter 3 describes the treatment of electric field amplification by plasma and the role of ion flux in the breakdown phenomena as well as the influence of magnetic field. Chapter 4 describes the experimental setup of a probe devoted to studies of interaction of high RF voltage and the SOL plasma of ASDEX Upgrade. Chapter 5 presents the results of the work which are the basis for the measures to increase the maximal achievable voltage on the antenna which we propose in chapter 6.

The meaning of the abbreviations which are often used in the text is decribed in the Appendix A.

Chapter 2

Phenomenology of RF breakdown on the ICRF antenna

Arcing in a fusion device with magnetic confinement is usually associated with excitation of arcs on a plasma-wall boundary [18, 19, 20]. These arcs (called *unipolar arcs*) lead to an increase of erosion rate of the first wall and a release of impurities to the edge plasma.

We are interested in arcing that occurs on the ICRF antennas when an external RF power is applied. The arcing can be considered as *bipolar arcs*. However arcing is a final stage of a developed high voltage breakdown. Let us start with a review of the possible processes that may be responsible for the voltage limits of the ICRF antenna.

There are several types of breakdown which can be viewed as candidates leading to the voltage limitation on the ICRF antenna:

- high-voltage breakdown in vacuum or vacuum arc;
- Townsend breakdown of neutral gas leading to formation of a glow discharge [21];
- multipactor discharge which can be subdivided in two types: pure electron resonance discharge [21, 22] and multipactor discharge with gas ionization [22].

Multipactor is possible only if RF voltage is applied to the electrodes. The basic mechanisms leading to the development of a vacuum arc and a glow discharge allow them to appear both with RF and DC voltages applied.

In real conditions of interaction of a RF antenna with the peripheral plasma of a fusion device with magnetic confinement two possible approaches exist:

1. First-order approach. Effects are defined by local physical conditions. Plasma edge parameters are considered as defined by external plasma inflow and its interaction with electrode surfaces, RF voltage and RF current on ICRF antenna. The interaction does not the affect the parameters of the central plasma.
2. Second-order approach. The ICRF power affects globally the central plasma. The plasma edge parameters are affected by the changes in the central plasma. This results in an additional non-linear dependence on the ICRF power.

In the framework of this thesis the second-order approach is not considered.

2.1 Main parameters

Assuming that initial local conditions in the region of antenna are set externally and taking into account the mentioned candidates for the breakdown on the antenna, one can distinguish the most important parameters in this context.

Local plasma parameters. Presence of a plasma near the antenna is essential. The plasma can screen external electrical field by forming sheaths of space charge near the electrodes. The space charge effect may lead to an increased local electric field on the electrode surface compared to the electric field in vacuum. The plasma potential should be taken into account for the description of the electric fields. The electron temperature is an important parameter defining ion flows from quasineutral plasma. The parameters are connected self-consistently.

RF voltage/current on the antenna. The ICRF antenna operates with high currents and high voltages. High RF voltages are mainly discussed in the work.

DC boundary condition for the antenna. The fact whether the system is capable to conduct DC current or not defines the boundary condition which affects plasma parameters. The reason for this is sheath rectification and self-biasing effects which appear when RF voltage is applied to an electrode in plasma.

Electrode geometry. It is known that avoiding sharp edges of electrodes is important for voltage stand-off in vacuum [23] because the electric field on the surface of an electrode is dependent on the surface geometry. If plasma is present and a sheath is formed near an electrode, the role of the second electrode can be played by the boundary of a quasi-neutral plasma.

Magnetic field. The presence of a magnetic field affects almost every parameter in the list: local plasma parameters, effective geometry of the system of electrodes, sheath effects, multipactor conditions.

Electrode material and surface properties. Surface processes play a decisive role in the ignition of a vacuum arc and the startup of glow and arc discharges.

2.2 Power transmission

Experience from the operation of the ICRF antenna systems can only partially help for understanding the power limitation. The reason for this lies in the relative complexity to diagnose the system. For ASDEX Upgrade the system consists of two antennas with two straps each [24, 25] (see also section 5.6). In Fig. 2.1 an ICRF system is shown schematically with the distribution of the RF voltage amplitude along the line (the so-called "standing wave pattern").

The coupling of RF power to the plasma, i.e. the efficiency of generation of waves which transfer the power to the central plasma plus the so-called *parasitic absorption*,

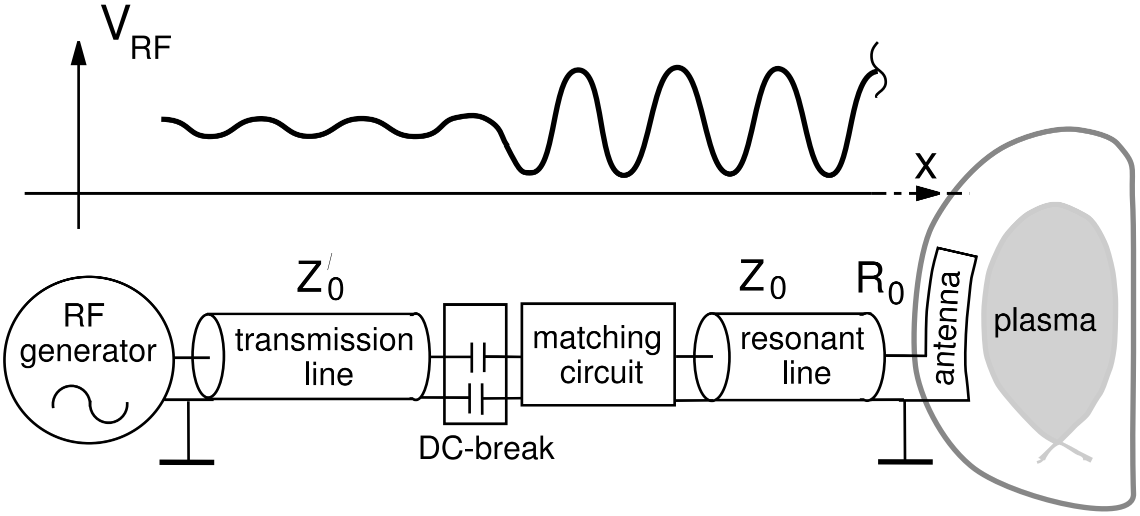

Figure 2.1: *Scheme of a simple ICRF system*

contributes to the effective load resistance R_0 of a system *antenna-plasma*. The parasitic absorption is defined as a part of the total ICRF power coupled to the plasma but absorbed at the plasma edge as a result of the processes related to interaction between RF fields and charged particles near torus walls (these processes usually take place parasitically in parallel to ICRF heating of the central plasma). Typically the magnitudes of R_0 are about few Ω.

The power is transferred to the antenna by a *transmission line*. For the noted frequency range the most suitable solution is to use coaxial transmission lines. The characteristic impedance Z_0 of the line depends on geometrical dimensions and insulation material. For high-power applications dry air is better suited as insulation medium for the pressurized lines. Also vacuum insulation should be partly used for transmission lines of an ICRF heating system. Values of Z_0 are usually set by the requirements for dimensions, losses in the lines and power handling (the maximal power the line can handle in a steady state operation). The latter is set by the formula:

$$P_{max} = \frac{V_{max}^2}{2Z_0} \tag{2.1}$$

where V_{max} is *voltage stand-off* of the transmission line. The typical values of the characteristic impedance of the transmission lines vary from 20 Ω to 75 Ω and differ from typical plasma R values. For this reason a wave carrying energy from a *RF generator* to the load (the forward wave) is partly reflected. A *matching circuit* represents an inhomogeneity which produces an additional reflection wave towards the RF generator with the same amplitude but out of phase with the wave reflected from the load. The two reflected waves interfere and in the ideal case only the forward wave exists between the matching circuit and the RF generator. Due to the presence of both forward and reflected waves a standing wave is formed (see Fig. 2.1) between the *antenna* and the matching circuit. A standing wave is characterized by voltage standing wave ratio higher than unity:

$$k = \frac{V_{max}}{V_{min}} > 1 \tag{2.2}$$

.

It is convenient to use the relations for the generalized voltage reflection coefficient ρ. According to the definition this complex coefficient is the ratio between the phasor value of voltage of the forward wave and the phasor value of voltage of the reflected wave. It can be written as:

$$\rho = \frac{Z - Z_0}{Z + Z_0} \tag{2.3}$$

where $Z = V/I$ is a complex impedance along a line (V and I the phasor values of voltage and current) and Z_0 the characteristic impedance of the line. The value of the impedance Z at any point of the line is often referred as input impedance.

If the RF system is matched perfectly the input impedance at the end of the matching circuit connected to the transmission line equals exactly to characteristic impedance Z_0 of the transmission line. This case is often referred as "traveling wave mode" ($k = 1$) for the transmission line. In reality the effective impedance R_0 of antenna-plasma system varies in time and no perfect matching is instantaneously obtainable. For this reason a standing wave is often formed between the matching circuit and the RF generator.

As a result of the mismatch higher voltages along the lines exist compared to the "traveling wave mode".

Quality of resonance is a measure which helps to understand how the resonant (unmatched) part of RF system reacts on the load changes. It is defined as:

$$Q = \frac{W_{stored}}{W_{dissipation}^{one\ cycle}} \tag{2.4}$$

The Q-value determines how much energy is dissipated during one RF oscillation compared to the amount of reactive energy stored in the system. It is important to distinguish between $Q_{no\ load}$ without load connected and Q_{load} for the resonant line with load. Applied to the ICRF system, the former notion is used for operation in vacuum with $W_{dissipation}$ defined by inherent RF losses while the latter corresponds to operation with high temperature plasma in the toroidal chamber. The Q-value without load connected can be estimated from:

$$Q_{no\ load} = \frac{\beta_p}{2\alpha_{at}} \tag{2.5}$$

where β_p – phase factor and α_{at} – attenuation factor of a wave. For a coaxial transmission line with the radii a and b of the inner and the outer electrodes respectively one has an expression for the attenuation factor defined by electrical resistance of the conductors:

$$\alpha_{at} = \frac{R_{sq}}{4\pi Z_0}\left(\frac{1}{a} + \frac{1}{b}\right) \tag{2.6}$$

where $R_{sq} = 1/\sigma\delta$ – resistance of a square meter of the surface defined by the electrical conductivity σ and the skin depth δ.

For safety issues and reliability of measurements a *galvanic separation*, (avoidance of ground loops) is mandatory. High currents which can flow between the groundings of the RF generator and the toroidal chamber during change of magnetic flux need to be avoided. The separation is realized by the use of a *DC-break*.

ICRF systems are usually more complicated than it is shown in Fig. 2.1. The main complications are in the way in which RF generators and antennas are coupled together and in the matching circuits. A description of the ICRF system for ASDEX Upgrade can be found in [24, 25, 26, 27].

General problem of voltage limitation in the ICRF system concerns the following components:

- coaxial electrodes in transmission lines
  the resonant transmission line have higher voltages and are most critical

- vacuum feedthrough and mechanical supports of the coaxial electrodes
  both for feedthrough and mechanical supports, discs made of ceramics are used: voltage stand-off of such a disc becomes unrecoverable when products of arcing form a conductive track on the insulator surface (e.g. carbon track on teflon insulator)

- antenna electrodes
  this work is mainly concentrated on studying the antenna voltage stand-off since the influence of plasma on the voltage limit is often essential.

2.3 Breakdown development on the ICRF antenna

A breakdown can be considered as a change in the antenna effective load impedance R_0. The change in turn is dependent on the location of the breakdown on the antenna since dimensions of ICRF antennas are comparable to the wavelength. If the breakdown appears close to a region with a high voltage, the real part of the input impedance jumps down from a high to a low value. The change results in a mismatch and the power is reflected back to the RF generator. The measured reflected power is used to detect the breakdown in the antenna or in the transmission lines.

When the breakdown is detected, the RF generator needs to be switched off immediately to avoid damage of the RF conductors by arcing. If for some reason the generator is not stopped after the breakdown, the input impedance at the generator connection point may differ strongly from the output impedance of the generator defined by specifications (typically 50 Ω). Modern RF generators are capable to deliver a constant power at $k < 1.5$ corresponding to the reflected power at the generator:

$$P_{reflected} = 0.04 \cdot P_{forward} \tag{2.7}$$

With a higher level of the reflected power the generator reacts on the external load by altering its output RF power from the requested values and often by starting to produce modulation of the power on low frequencies. Reflected power at the generator is decreased by:

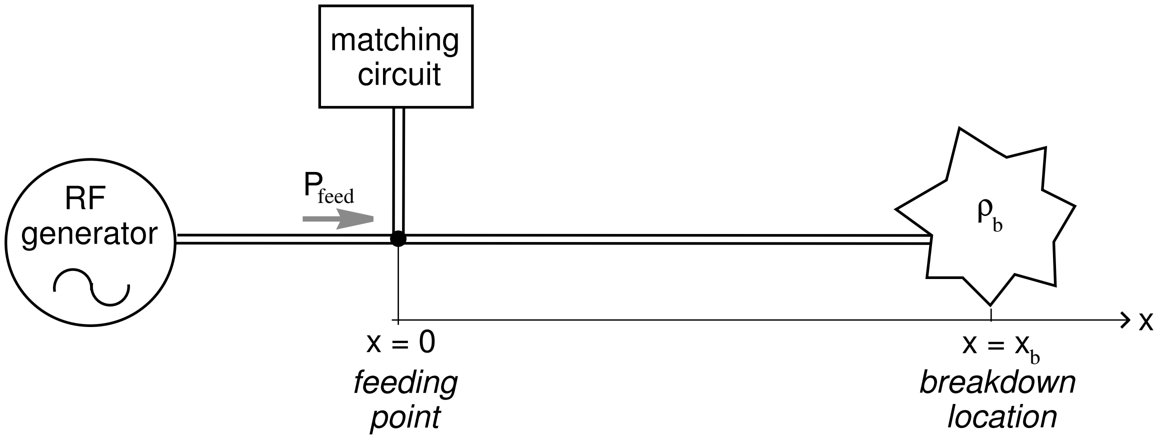

Figure 2.2: *Breakdown in a single resonant line*

- line losses add an attenuation of the order of few dB
- any "advanced" ICRF system is designed in a way to reduce reflected power at the generator.

This helps to obtain the value of the input impedance on the generator side close to 50 Ω.

For the ASDEX Upgrade ICRF system, a 3 dB hybrid power splitter on the antenna side [28, 29, 30] is used (see section 5.6). The reflected power at the generator side in this system is mostly dependent on the asymmetry of the reflected power from the two antennas. If the reflection from the two antennas is approximately the same, the reflected power at the generator is not influenced by the absolute value of the reflected power from a single antenna. Online matching circuits, such as Fast Ferrite Tuners (FFT) [31, 32] can be used to match a change in the load impedance during RF pulse as well. Thus the generator can sometimes continue to deliver power after the breakdown on the antenna has evolved into arcing.

Now we assume that the generator proceeds to deliver the same power after the breakdown. For simplicity the circuit shown on the Fig. 2.2 is considered. The type of the breakdown defines the initial value of reflection coefficient ρ_b at the load. According to transmission line theory an amplitude voltage-current (V-I) characteristic of an "external power source" at the breakdown location x_b is set by the formulas:

$$I_b = |I_{x=x_b}| = \left| \sqrt{\frac{2 \cdot P_{feed}\,(1-|\rho_{feed}|^2)}{Re\left(Z_0 \cdot \frac{1+\rho_{feed}}{1-\rho_{feed}}\right)}} \cdot \frac{\exp(-\gamma x_b) - \rho_{feed}\exp(\gamma x_b)}{1-\rho_{feed}} \right| \tag{2.8}$$

$$U_b = |U_{x=x_b}| = \left| I_{x=x_b} \cdot Z_0 \cdot \frac{1+\rho_b}{1-\rho_b} \right| \tag{2.9}$$

$$\rho_{feed} = 0.5 \cdot \left(\rho_b \cdot \exp(\gamma x_b) + \rho_{match}\right) \tag{2.10}$$

where P_{feed}, ρ_{feed} – forward power and reflection coefficient at the feeding point, ρ_{match} – reflection coefficient of the matching circuit at the feeding point, $\gamma = i\beta + \alpha$. The case $\rho_{feed} = 0$ represents a line perfectly matched for the load characterized by ρ_b.

The relations (2.8)–(2.10) for I_b and U_b should be satisfied as as well as a relation between I_b and U_b set by local physical conditions. External circuit and physical conditions at the breakdown location set the actual scenario for the development of a discharge. The amplitude V-I characteristic of the external circuit can limit the current at the load as the system is not specially matched for the loads typical for gas discharges. It may influence the discharge load impedance since the load (defined by gas discharge properties) depends on the power applied non-linearly. However equations (2.8)–(2.10) do not describe the reaction of the external circuit on transient (very fast) changes of the load. In this case the stored (circulating) RF power is available to be dissipated in a discharge. Therefore the stored power characterized by the Q-factor may influence the discharge evolution (see below in section 2.4.2). Thus the breakdown can lead either to a steady-state gas discharge (the existence of which is defined by external circuit with equations (2.8)–(2.10) or to a pulsed discharge (a discharge with fast termination the external circuit being characterized by the stored reactive energy).

The load impedance of gas discharge is one of the most interesting issues discussed in gas discharge physics. Taking in account that load impedance is a ratio between current and voltage on electrodes it is important to discuss the phenomena which may appear in an electrode gap for different neutral gas pressures.

2.4 Gas discharge phenomenology

Gas discharge physics describes phenomena in a wide range of neutral gas pressures from high-vacuum case ($P < 10^{-4}$ Pa) to a high-pressure case ($P > 10^5$ Pa) covering different voltage forms: DC, AC, RF, UHF. We are mainly interested in the pressures below 100 Pa. Higher pressures are not considered for the problem of a breakdown on the ICRF antenna in conventional operation. Here we exclude studies of high voltage breakdown in the pressurized transmission lines.

For simplicity we use a plain geometry of two parallel plates as a system of electrodes. The physical effects connected to a more complicated geometry are discussed later. For a better definition of a pressure and voltage ranges of interest we assume that the electrode gap is one centimeter large.

The terms *self-sustained discharge*, *self-sustained current* and *non-self-sustained current* are often used for the description of gas discharge phenomena. *Self-sustained discharge* can be understood as a discharge capable to sustain a current (which is called *self-sustained current*) between the electrodes by birth of charged particles in the electrode gap and on the electrodes without external influence. *Non-self-sustained current* means a current flowing between the electrodes carried by the charged particles produced by an external ionization source. However there exists no well-defined boundary between self-sustained and non-self-sustained currents. For example, the currents appearing between electrodes in vacuum due to field emission (paragraph 2.5) can be treated as

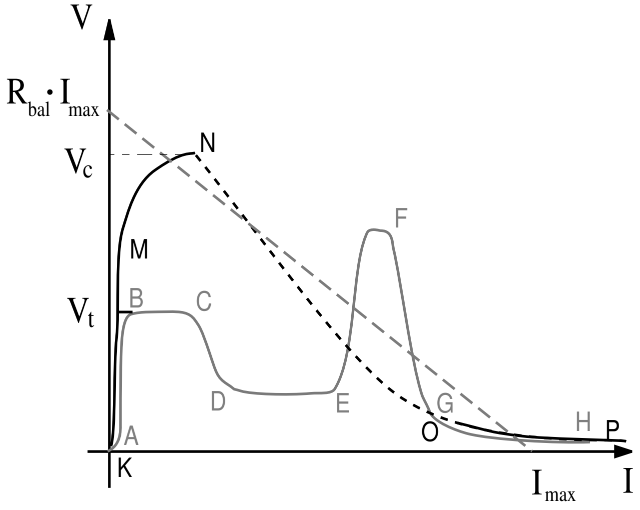

Figure 2.3: *Stationary voltage-current characteristics of the electrode gap for DC voltage. Black curve - vacuum,* $p < 0.1$ *Pa; gray curve - low-pressure,* $p \sim 0.1 \div 100$ *Pa [33, 21]. Dashed gray curve - load curve defined by the external DC circuit.*

self-sustained while the currents appearing by photoemission of electrons by external light source should be treated as non-self-sustained. Usually there is always a source for small non-self-sustained currents in laboratory conditions, for example due to the presence of background radiation.

Numerous literature is available for DC discharges. Since physical mechanisms leading to a discharge are often similar for RF and DC voltages it makes sense to start the discussion with DC discharges.

2.4.1 DC discharges

A qualitative picture summarizing the discharge phenomena with DC voltage between two parallel plates can be presented with the help of DC V-I characteristic of the electrode system [21, 33, 34]. In Fig. 2.3, the stationary characteristics for DC voltage are shown. Each point on the solid curves is a stationary point, i.e. the change along the curves happens with a characteristic time much longer than time of the dissipation of energy stored in reactive elements of the power circuit.

The black curve in Fig. 2.3 corresponds to the vacuum case or to pressures $p < 0.1$ Pa. The gray curve represents the characteristics of self-sustained discharges at the low-pressure case which is defined:

$$p \approx 0.1 - 100 \text{ Pa}. \tag{2.11}$$

Here a gas which has a negligible electron attachment coefficient in the working parameter space (electropositive gas [33, 21]) is assumed as a working medium. The lower pressure limit in the range is set by the pressure critical for ignition of self-sustained RF glow discharge.

An operational point on the stationary V-I curve is chosen by the so-called *load curve* (dashed gray line in Fig. 2.3):

$$\varepsilon = R_{bal} \cdot I_{max} = V + I \cdot R_{bal} \tag{2.12}$$

where ε - electro-motive force of an external power circuit presented as a product of the maximal current the external circuit can deliver I_{max} and balast resistance R_{bal} connected in series with the electrode gap which limits the current of the DC power source.

DC V-I characteristic (Fig. 2.3) starts from non-self-sustained current when one applies a small voltage between the electrodes. In the vacuum case (black curve) the voltage can be increased to high values (KM segment of the curve) until the dark field emission current is observed (MN). When the voltage is further increased the current grows exponentially and at some critical value V_c a *vacuum arc* appears on the cathode (NO) leading to an arc discharge (OP). A stationary arc discharge can only appear if the external DC power circuit is capable to deliver high enough power, i.e. current I_{max} as in Fig. 2.3.

If the pressure of the working gas is increased in the gap (gray curve), at some threshold V_t (ignition voltage) the current increases with increasing input power. The current is rather small ($10^{-10} \div 10^{-5}$ A), though the charge is transferred by charged particles born as a result of ignition of self-sustained discharge, the so-called *Townsend dark discharge.* The discharge is characterized by a small ionization degree and a negligible influence of the spatial charge on the electric field.

If the operational point is chosen to increase the current, the discharge goes along the unstable segment CD (*subnormal glow discharge*) to a *normal glow discharge* (DE). The latter is characterized by formation of a cathode potential drop and lower voltages on the electrodes for the discussed circuit. By localization of the potential drop near the cathode (formation of cathode sheath) a high local electric field is achieved in the sheath which provides high ionization rate, though the voltage on the electrodes becomes lower. The discharge initially does not cover the whole area of the electrodes. The current density of the normal glow discharge on the cathode stays constant in the discharge area. When the current is increased, the discharge spreads on the cathode until it covers the whole cathode surface and becomes an *abnormal glow discharge* (segment EF). For the latter a change of the current means a change of the current density at the maximum possible discharge area.

Further increase of the current up to a threshold value set by the cathode material ($\gtrsim$ 1 A) leads to a *glow-to-arc transition* (segment FG). The transition is realized by the formation of a *single cathode spot* on the cathode surface. The main reasons for the formation of a cathode spot may be:

- local high voltage breakdown produces a spark leading to an avalanche-like appearance of the cathode spots;
- the whole glow discharges collapses into a current channel (the so-called *contraction*) leading to high current densities and an arc.

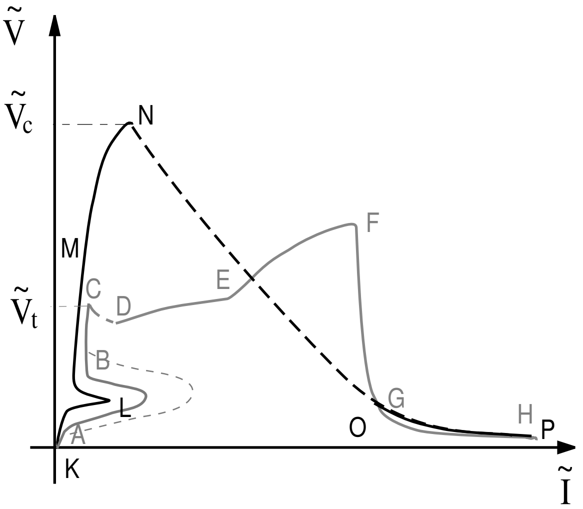

Figure 2.4: *Stationary voltage-current characteristics of the electrode gap for RF voltage. Black curve - vacuum, $P < 0.1$ Pa; gray curve - low-pressure, $P \gtrsim 0.1$ Pa. Constructed from [22, 35, 36].*

The *arc discharge* (segment GH) represents a respawning group of the cathode spots having certain properties depending mainly on the cathode material and the maximal current the circuit can deliver.

2.4.2 RF discharges

In Fig. 2.4 qualitative stationary amplitude V-I characteristics for the two-electrode system with RF voltages applied are shown. The black curve corresponds to the vacuum case $P < 0.1$ Pa. The characteristic shown by the gray curve is constructed based on the RF discharge phenomena at low-pressures from the noted range of interest (the condition (2.11)), e.g. $P \sim 10$ Pa for He. The experimental results from [35, 36] are reflected in the curve qualitatively. At the low pressures the glow discharge can be created at a high voltage which is of interest for us since we are looking for the voltage limits in the low-pressure range.

The real discharge in the electrode gap is dependent on the system details like geometry, materials of the electrodes, gas and may not include every segment from Fig. 2.4 or may include some features (see below). However we try to summarize the effects observable in the double electrode RF system at low pressures. As we already know, a real stationary amplitude V-I characteristic is defined by a load curve derived from equations (2.8)–(2.10). In comparison to the DC case the load curve is not linear and depends on the load impedance. Moreover the curve contains more parameters of the system.

Let us consider the vacuum case (black curve, Fig. 2.4). With increasing the RF voltage on the electrodes a small RF current is registered proportional to the voltage because of a non-zero capacitance between the electrodes. The possibility to conduct capacitive current through the electrode gap is one of the principal distinction of an RF discharge to the DC discharges to be discussed later.

At a RF voltage typically less than 1 kV, multipactor ([22], section 2.6.6) appearance is probable. The effect is observed as an increase of RF current in a very narrow voltage range (L) and may be a purely electron discharge or a gas amplified discharge. At high voltages (segment MN) field emission currents become detectable and at some critical voltage $\tilde{V}_c$ a vacuum arc similar to the DC vacuum arc is ignited (segment NO). Segment OP represents RF-sustained arc discharge on the electrodes.

The gray curve in Fig. 2.4 shows the behavior of the electrode system at the pressure when gas ionization starts playing a role.

When the RF voltage is increased, the RF current increases proportionally untill the voltage satisfies resonant conditions for multipactor which are influenced by gas ([22], section 2.7.3). Ionization of neutral particles by electron impact assists multipactor and makes an additional source of electrons. Gas in the electrode gap is partly ionized and the discharge is not purely electron. Gas desorption from the electrodes under conditions of electron bombardment can lead to an increase of the current (and voltage, see section 2.7.3) illustrated by the dashed gray curve in Fig. 2.4. At higher pressure than showed in Fig. 2.4, the voltage required to have conditions for the multipactor effect is of the order of the voltage $\tilde{V}_t$ to start an RF glow discharge. Therefore ignition of the RF glow discharge (CD) (paragraph 2.7) at higher pressures may be accompanied by multipactor.

At the pressures $P < 100$ Pa the glow discharge may exist in two forms: α- (DE) and γ- (EF) *discharges*. In the α-discharge the main fraction of the RF current on the electrodes has a displacement nature due to formation of sheaths near the electrodes. The α-discharge is not dependent on the material of the electrodes and is sustained only by the ionization of gas in the gap. The γ-regime of the discharge depends on processes of recycling of particles on the electrode surfaces and therefore on the electrode material. The transition from α to γ discharge for the range of low pressure is usually monotonical and rather smooth for the light gasses (e.g. He [35, 36, 37]). Experiments with heavy inert gases show that the transition form α to γ regimes may be accompanied by a hysteresis on the I-V characteristic (e.g. for Ar [38]). A more detailed discussion about the features of α and γ discharges will follow in section 2.7.

Existence and evolution of RF discharge

We see from Fig. 2.4 that a rather broad range of loads may be used as equivalent of a simple electrode gap. For a given system with $Q > 1$ the existence of the specific form of stationary discharge is defined by equations (2.8)–(2.10) which include parameters of the matching circuit. A transition to the discharge with low voltage-to-current ratio leads to a mismatch from the resonant conditions. The mismatch results in the strong reduction of the power coupled to the resonant part of the circuit. Decrease of the net power available for the discharge affects the evolution of the discharge, especially for the case of the breakdown at the location with initial high RF voltage. As a result, after the breakdown, the power input is self-regulating in a way that may lead to a self-suppression

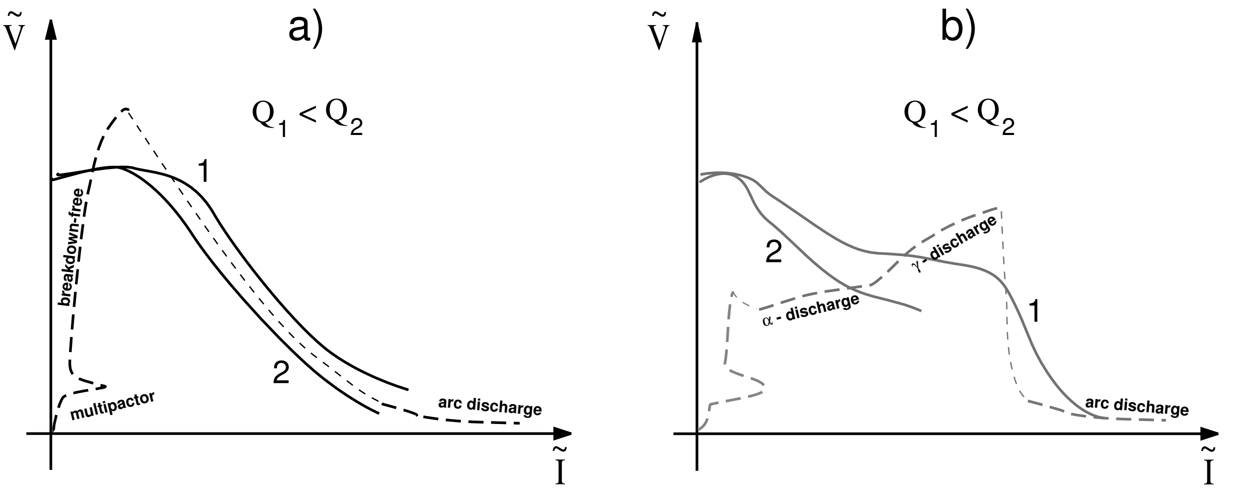

Figure 2.5: *Qualitative stationary load curves for two different systems with $Q > 1$ matched for high impedance operation: system 1 has a lower Q than system 2: a) vacuum operation, b) low-pressure, $P \gtrsim 0.1$ Pa.*

of the discharge - a pulsed discharge.

As an example of above noted features, in Fig. 2.5 the qualitative stationary load curves for two systems with $Q > 1$ are presented ($Q_1 < Q_2$). The load curves determine a possible evolution of a discharge if the systems are matched for a high impedance load (this is the case for the high voltage region of the antennas), if this evolution happens on the timescale longer than required for the reactive (circulating power) to dissipate.

The system 1 on the figure has low enough quality factor that allows in the stationary mode to fulfill the requirements for ignition of the variety discharges (the curves intersect or are above the I-V characteristic of the gap) which correspond to a rather wide impedance range. In contrary, for the system 2 it is impossible to get stationary arc discharge or even produce the glow γ-discharge (curves are below the required voltage, therefore not sufficient power is available). There is an experimental confirmation that a transition from α to γ-discharge may be difficult for high Q-circuits matched for operation with α-regime [39]. Also from the experiments with Ar [38] we know that the transition from α to γ regime may be accompanied by a jump on the I-V characteristic that can be partly explained by a mismatch of the RF system.

From the other hand, as we discussed earlier (see section 2.3), the high-Q systems may contain a high reactive power which leads to the possibility of a pulsed discharge formation. Thus a specific discharge form may appear transiently but can not be sustained in stationary regime. In other words a dynamical I-V characteristic of a high-Q system can be above the characteristics of a variety of the discharges.

The vacuum arc (see segment OP in Fig. 2.4 and *arc discharge* in Fig. 2.5) is characterized by the highest and the fastest change in the net power among all the discharges since the arc happens at voltage maximum and transforms it to a short circuit. It is often the case that a vacuum arc igniting at the voltage maximum leads to pulsed arc discharge and afterwards to self-suppression.

2.4.3 RF discharges responsible for voltage limitation

From the review of RF discharges we can determine the candidate processes which can be responsible for voltage limitations on the ICRF antennas.

In section 2.5, we discuss the vacuum arc and the underlying physics of its ignition as a possible candidate to appear on the antenna.

Different physical processes may assist in the appearance of vacuum arc. These can lead to an increase of the number of charged particles in the electrode gap. Section 2.6 makes the transition from the vacuum to plasma processes and is devoted to the description of features of particle movement at high RF voltages and mechanisms of generation of charged particles in the electrode gap.

Section 2.7 describes features of high voltage discharges from Fig. 2.4 which correspond to currents lower than that of an arc discharge. A special attention is paid to the particle birth processes.

2.5 RF vacuum arc ignition

A *vacuum arc* can be defined as RF sustained discharge accompanied by the formation of the cathode spots on the surface of the electrodes placed in vacuum with the pressure of the residual gas causing no influence on the breakdown process. A RF vacuum arc is an arc discharge which ignites as a result of the processes initiated by high electrical fields on the cathode surface.

2.5.1 Field emission

A high voltage breakdown in vacuum is initiated by *field electron emission* effect. Application of a high electrical field to the surface of an electrode with a work function ϕ makes possible the escape of electrons from the metal surface by tunneling through the potential barrier (Fowler and Nordheim, [40]). The effect is more pronounced on the microprotrusions on the electrode surface. The electric field is much higher on the top of the small spikes on the surface. The spikes on the electrode surface appear because of mechanical treatment and also by modification of the surface during plasma operation. For electric field on the surface the dimensionless parameter β is introduced which accounts for the electrical field amplification on microprotrusion. An effective emitting area of the electrode surface A is used which can be presented as the total area of emitters. The electron current mode is emitted in accordance with the Fowler-Nordheim (FN) law [21, 23, 41]. Considering effective parameters β and A_{DC} for a direct-current case, FN formula is written:

$$I_{DC} = A_{DC} \cdot \frac{1.54 \cdot 10^{-6} \beta_{DC}^2 E_{DC}^2}{\phi} \cdot \exp\left(\frac{-6.83 \cdot 10^9 \phi^{3/2}}{\beta_{DC} E_{DC}} \right) \tag{2.13}$$

where ϕ – electron work function in eV, E_{DC} – DC electrical field on the surface in V/m. Equation (2.13) is valid for rather low temperatures. At high temperatures, when an arc on the cathode exists already, the thermo-field emission should be taken into account more accurately [45]. However for the initial phase of cathode spot development we consider pure field emission, i.e. equation (2.13) is applicable.

Taking into account the sinusoidal alternating voltage on the electrode a good approximation to equation (2.13) is made [42, 43, 44] for E_{RF} as peak electric field on the electrode surface:

$$I_{RF} = A_{RF} \cdot \frac{M \cdot \beta_{RF}^{5/2} E_{RF}^{5/2}}{\phi^{7/4}} \cdot \exp\left(\frac{-6.83 \cdot 10^9 \phi^{3/2}}{\beta_{RF} E_{RF}}\right) \tag{2.14}$$

where $M = 5.27 \cdot 10^{-12} (\mathrm{V/m})^{-1/2} \cdot (\mathrm{eV})^{3/4}$ is a constant derived from the integration over the RF period. Experimentally measured dependence of field emission current is usually fitted to equation (2.14) to derive A_{RF} and β_{RF} [44]. As it can be seen from (2.14), the emitted electron current is exponentially dependent on ($\beta_{RF} E_{RF}$) and ϕ. These quantities are very sensitive to the surface conditions on the electrodes:

1. *Surface material.* In the literature different values can be found for the work functions [46]. One of the reasons lies in the different measurement techniques (by field emission, photoemission or contact potential difference). Another reason is in different finishing of the surface of the samples before the measurements are made (electrolytical or mechanical polishing, baking at different temperatures, plasma cleaning) which affect the surface purity and homogeneity (impurity inclusions, formation of oxide or nitride films) as well as surface microroughness which influences electrical field amplification. High ϕ is required to shift the effect of field emission to the higher electric fields. For the ICRF antenna the material should be chosen which do not form oxides, nitrides and carbons which have lower work function than pure bulk material. However such metals as stainless steel, Cu, Ag, Au, Ni are often used as surface electrode materials (for pure samples $\phi \approx 4-5$ eV). A majority of these materials have tendency to form oxide films on the surface and a reduction of ϕ by 1-2 eV may be the result. For instance, W and Ta as well their oxides and carbons have the high work function of $\phi > 4.5$ eV .

2. *Surface microroughness (small-scale geometry).* Small microprotrusions (sometimes called whiskers) with characteristic sizes from 1 nm to 1 mm lead to electrical field amplification factor of $\beta = 10-500$. These regions on the surface are called emission sites and the main fraction of the field emission current is carried by them. Very high local current densities ($\sim 10^6 - 10^{14}$ A/m^2) may be present on these sites. Surface microroughness is characterized by an effective height of microprotrusions R_z and written in μm. R_z is affected by the methods of electrode finishing.

3. *Surface homogeneity.* The boundaries between regions with different material densities bring an undesirable increased diffusion of impurities from bulk towards the surface along these boundaries and its accumulation on the surface. The growth of microprotrusions on the surface is often observed on grain boundaries.

4. *Surface purity.* Contamination of the surface by impurities leads to high rates of gas desorption during high power operation and also to appearance of the emitting sites [51]. Chemical and physical bonded contaminants, e.g. oxide layers, dust

microparticles [47, 48], metallic, dielectric or semiconductor [23] inclusions affect vacuum breakdown conditions. Impurities of alkali-earth metals like Na or Ka can affect the field emission directly by reducing work function of the surface material (≈ 2 eV). Dielectric (e.g. some oxides) and semiconductor inclusions on the electrode surface may give rise to the so-called non-metallic electron emission at high voltages [23, 49]: the inclusions can often make the tunneling from the metal through metal-inclusion interfaces easier. The electrode contamination explains that the electrode polishing does not always help to minimize field emission currents [49] and eventually influences the electric field limitation [50, 51].

2.5.2 Conditioning by high voltage

To reduce the effects of non-ideal surface several conditioning techniques can be used [51]. One of the methods to increase operational voltage limits is the so-called "breakdown" conditioning [52, 53]. It is based on using repetitive breakdowns initiated by short high voltage pulses. The conditioning is observed if the external power is switched off immediately after the breakdown initiation to avoid stationary arc discharge on the electrode. Sometimes this type of conditioning is called "sparking" or "spot-knocking". There are some features of the technique which should be taken into account to keep the conditioning efficient.

The breakdown conditioning of the surface is only reasonable if it leads to a reduction of number of microparticles and microprotrusions or to modification of the latter. This should lead to a decrease of the effective parameters β and A.

However, contrary to small spikes on the surface and small microparticles, large particles often may not be evaporated by Joule heating with field-emission currents, but may be welded to the surface. If the welding happens, the particles may remain as emission centers for a number of breakdowns that would lead to a reduced effect of the conditioning. This is an additional reason to decrease the pulse length and increase the voltage applied during conditioning to values higher than required for normal operation of a high voltage device. Before high voltage application the dust particles often do not have good mechanical (also chemical) and electrical connection with the surface. Therefore many particles may be removed from the surface by RF electric field since they can acquire some positive charge by emitting electrons. A particle removed from the surface can be pumped out by vacuum pumps or be divided into many small particles by an impact with the electrode surfaces after an acceleration in high electric field. The small particles can be evaporated or modified by the field emission currents.

An evaporation or a melting of the spikes of the microprotrusions or of the small particles do not necessarily lead to a breakdown initiation. If the amount of vapor released is small enough or is transported from the vacuum gap (e.g. back to the electrodes) before a high density plasma is created by ionization processes, the disintegration of such a microprotrusion leads only to a transient charge transfer between the high voltage electrodes, but not to arcing. Sometimes this kind of conditioning (called conditioning by field emission currents) is used [54], when the operational voltage is high enough to initiate field emission from microprosperities and at the same time low enough to avoid the breakdown initiation. After a certain time of such operation, the surface roughness parameter decreases and field emission currents tend to be reduced too.

Similarly an already developed cathode spot may disappear without ignition of other cathode spots if the conditions on the surface are not favorable. In other words the arcing can be terminated after some time even if the power applied to the electrode was initially sufficient for the arc sustainment. For example, the long-sustained arcing cleans the surface and the arc may vanish if it was sustained partly by the fact that impurities were present on the surface. However, even the cleaning effect of the long-term arcing does not compensate for the surface erosion produced by cathode spots. The erosion is definitely unfavorable for the high voltage operation and leads to the developement of a microstructure of the surface and at least to transient sparking, when high voltage is applied again.

We will discuss other general aspects and methods of the ICRF conditioning in the subsections 2.6.2, 2.6.3, 2.7 of this chapter.

2.5.3 Spark stage of RF vacuum breakdown

Assuming that the electrodes are conditioned and gas desorption is negligible one can name the main reasons for high-voltage RF breakdown in vacuum:

- injection of electrons into electrode gap by field emission;
- vaporization of one of the emitting sites on the cathode by Joule heating during field emission, temperature of the sites is influenced by Nottingham [55, 45] (heating/cooling) effect;
- vaporization of anode points locally heated by dense beam of electrons produced on the cathode.

The *spark stage* of a vacuum breakdown [53] is the short phase of a self-sustained discharge at high voltage, high current with falling amplitude V-I characteristic of the gap. The spark stage is characterized by a growing conductance of the gap and is a transition into vacuum arc discharge.

Considerations similar to the ones applied to the DC vacuum breakdown may be used. The case with RF voltage waveform on the electrodes at the frequency range of interest corresponds to the RF period from 8 ns to 50 ns. During each period cathode and anode are swapped. In a DC case the spark stage takes a time τ_{spark} from 10 ns to 100 ns [53]. The conductive current collected by the electrodes is defined by Child law since plasma density is high and spatial charge limits the current emitted by the plasma. The current is mainly an electron current as the ions in the gap are created by ionization of vaporized electrode material and are massive and motionless for the timescale of the spark stage. During half of a RF period when an electrode producing initial vaporization of the material acts as an anode (assuming that the evaporation happened when the electrode was a cathode), the ion density near the electrode can be reduced to:

$$\omega_{pi}^{metal} \approx \omega_0 \tag{2.15}$$

where ω_{pi}^{metal} – metal ion plasma frequency. However the value of the plasma densities of about 10^{20} m^{-3} may be still present near the electrode after the half of RF period when the plasma is assumed to consist of single-charged ions of iron. On the other hand the inverse polarity of the voltage favors further ionization of the metal vapors and heating of the surface by electron beam, created by the field emission effect on the other electrode. This may lead to the further amplification of the plasma density and makes the formation of an arc on the cathode probable for the RF case. Due to the change of the voltage polarity in a time comparable to that of the spark stage, the development of the RF spark can take longer as the combined field-thermal emission (the cathode process) should take place to sustain the arc.

The transition to a (quasi)-steady-state vacuum arc discharge happens when two main conditions are realized (both for DC and RF cases):

1. external circuit delivers a current exceeding a critical value at a voltage high enough to sustain cathode spots;

2. combined field-thermal electron emission is initiated from the cathode.

2.6 Charge particles in electrode gap in vacuum

The nature of field emission effect makes it a cathode effect, though in reality it may lead to appearance of new processes taking place not only on the cathode. The processes are especially strong for non-conditioned and contaminated electrodes.

1. *Cathode processes:*

    - heating of emitting cites: Joule heating by field emission currents and heating by ion impact;
    - gas desorption due to the heating of the emitting sites;
    - ion stimulated desorption;
    - emission of secondary electrons and ions by impact of ions and fast neutrals born in the electrode gap.

2. *Volume processes:*

    - ionization of desorbed gas by electrons accelerated in the high electric field in the gap;
    - charge exchange between desorbed neutrals and ions born in the gap and on the cathode;
    - ionization of neutrals by ion-neutral and fast_neutral-neutral collisions.

3. *Anode processes:*

    - gas desorption due to local heating by the electron beam and electron stimulated desorption (ESD) of gas from the anode;

- secondary electron emission by an electron beam produced by field emission from the cathode and high voltage between the electrodes.

Processes connected with photo-emission and photo-ionization further contribute to charged particle generation.

The listed processes need also to be considered for the further discussion of high voltage RF breakdown phenomena in the presence of external plasma and require a more detailed description.

2.6.1 Particle motion in vacuum at high RF voltage

Let an alternating voltage on one of the electrodes be: $V = V_0 \cos \omega_0 t$. We assume no collisions and no space charge in the gap, then an electron born at the cathode at $t = 0$ can pass the gap between the electrodes in the following time (initial velocities of electrons after field emission and secondary electron emission are neglected):

$$t_{pass} = \frac{1}{\omega_0} \arccos \left(1 - \frac{\omega_0^2 m_e d^2}{e V_0} \right) \tag{2.16}$$

where e – elementary charge, V_0 – amplitude value of RF voltage across the gap, ω_0 – generator frequency, m_e – electron mass, d – gap distance. The corresponding displacement of electrons is:

$$d_e = \frac{e V_0}{\omega_0^2 m_e d} \tag{2.17}$$

At relatively low RF voltages (below 5 kV) the displacement of electrons during half of RF period can be equal to the interelectrode distance d. If these conditions are fulfilled in a system with electrodes having high secondary electron emission coefficient (see below section 2.6.5), the number of electrons can be multiplied. The effects in connection to the electron multiplication are described below in sections 2.6.6, 2.7.3, 3.4.3.

Let us consider the case of high RF voltages. Electrons leave the gap in a time much smaller than RF half-period when $t_{pass} \ll \pi/\omega_0$ or:

$$\frac{d_e}{d} \gg 1, \tag{2.18}$$

i.e. when the electron displacement during RF period is much larger than the gap distance. For $\omega_0 < 120$ MHz, $d = 1$ cm criterion (2.18) is fulfilled for voltages $V_0 > 5$ kV. Assuming that the most part of electrons is emitted when field emission currents are at maximum (high-voltage phase of RF oscillation) the noted condition exists always and is valid both for field emission electrons and for the secondary emitted electrons. Therefore in vacuum for the voltages of interest ($V_0 > 10$ kV) electrons leave the electrode gap fast. The maximum velocity an electron can obtain is:

$$v_e^{max} = \sqrt{\frac{V_0}{2 m_e}} \tag{2.19}$$

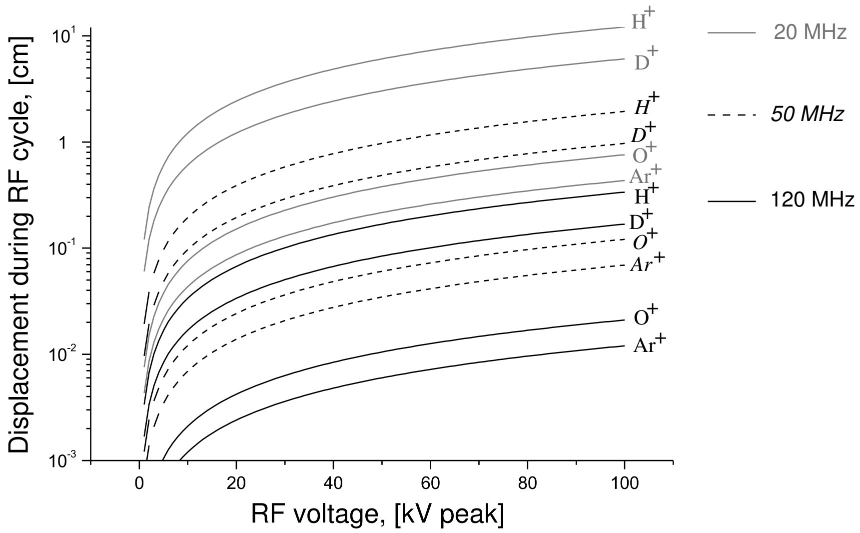

Figure 2.6: *Displacement of ions in RF half-period with zero initial velocity.*

For an estimation of a displacement of ions during RF half-period d_i without taking into account initial velocity of a single charged atomic ion, one can use the formula:

$$d_i = \frac{2eV_0}{\omega_0^2 m_i d} = 0.485\ \frac{V_0,\ [\mathrm{kV}]}{\mu_i\ (f_0,\ [\mathrm{MHz}])^2},\ [\mathrm{m}] \tag{2.20}$$

where m_i – ion mass, $\mu_i = m_i/m_p$– ion mass expressed in proton mass, f_0 – linear frequency. The simple estimation (2.20) allows to determine the reaction of different ions on high voltage in Fig. 2.6. The figure shows that light ions (H^+ and D^+) may pass the whole electrode gap, i.e. $d_i \sim d$. Heavy ions ($\mu > 10$) can be in principle assumed as motionless in vacuum during RF cycle. However displacement during half of RF cycle may be larger than d_i. For ions having an initial velocity in direction to the electrode with lower voltage comparable or higher than the velocity an ion can achieve in the voltage gap $v_i^{max} = \sqrt{(2V_0)/(m_i)}$, the effective displacement d_i is larger. Having initial velocities of the order of v_i^{max} in phase with external electric field means that ion is either back-scattered at the time close $t = n\pi/\omega, n = \pm 1, \pm 2, \pm 3, ...$ or it is born by charge exchange with fast neutrals.

Thus we can conclude that light ions of hydrogen isotopes for the parameter range considered can follow RF oscillations of electrical field in vacuum. Typical energies of these ions vary from few hundred eV to eV_0. For heavy ions which can appear in the gap by gas desorption from the electrodes (e.g. after exposure in atmosphere) one can assume that $d_i \ll d$ though a finite ion current onto the cathode exists always. It can be estimated that the maximal energies of ions collected by cathode are of the order of few keV for 10 kV< V_0 <80 kV.

The electron current onto an electrode is much larger during RF half-cycle than the ion current for the case when plasma density in the gap and ion space charge are small.

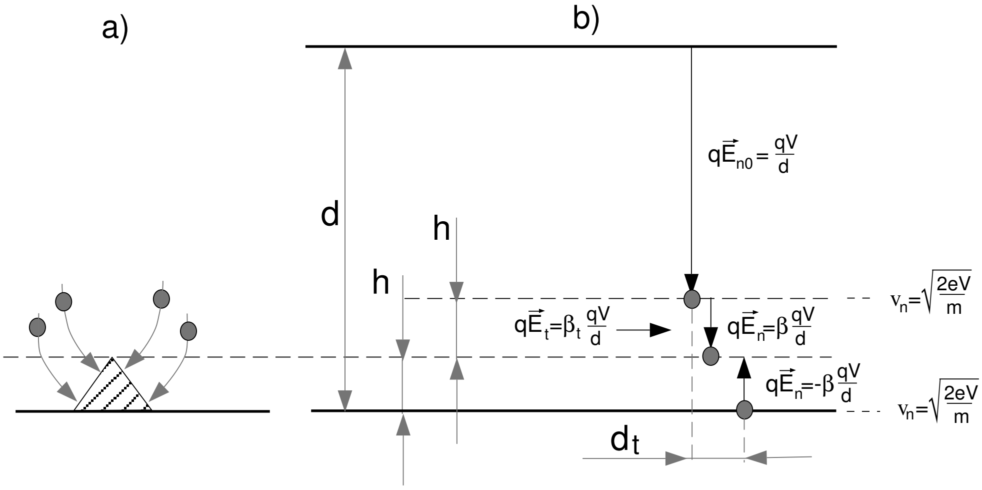

Figure 2.7: *a) Particle focusing to a microspike; b) a simple model of microprotrusion electric field to estimate the tangential displacement* d_t *of a particle with a charge q (b).*

Change of the distribution of electrical field by ion space charge in the gap can be neglected and the distribution can be assumed as in vacuum as long as:

$$d \ll \sqrt{\frac{2\epsilon_0 V}{e n_i}} \tag{2.21}$$

where n_i – ion density in the gap, V – voltage on the electrodes. Assuming n_i=const the ion density represents the density of plasma inside the gap. The screening properties of plasma are discussed in details below in chapter 3.

2.6.2 Particle flux focusing on the microscale

In the conditions of an inhomogeneous electrical field on the surface due to the existence of microprotrusions (tips) on the electrode the charged particles may be focused towards the protrusions (Fig. 2.7a). One can estimate the displacement of a particle tangentially to the surface in vacuum for a simple model on Fig. 2.7b. In the model the electrical field of the microprotrusion is approximated by the tangential field $\boldsymbol{E_t}$ and the field perpendicular to the surface $\boldsymbol{E_n}$. $\boldsymbol{E_t}$ and $\boldsymbol{E_n}$ are assumed to exist in the region starting from $2h$ from the surface, where h is the microprotrusion height, and ending on the surface. Furthermore we assume that $\boldsymbol{E_n}$ has a direction corresponding to acceleration of ions to the surface at a distance larger than h from the surface. At a distance smaller than h from the surface the field is assumed retarding. The arrows on the Fig. 2.7b present the forces qE acting on the particle, where q – particle charge. Since $h \ll d$, the particle velocity at the boundary of appearance of $\boldsymbol{E_n}$ and on the surface is considered to be $v_0 = \sqrt{(2V)/(m)}$. Fields $\boldsymbol{E_t}$ and $\boldsymbol{E_n}$ are presented as functions of the main vacuum field $E_{n0} = V/d$ by using field amplification β_t and β respectively: $E_t = (\beta_t\ V)/d$ and $E_n = (\beta\ V)/d$.

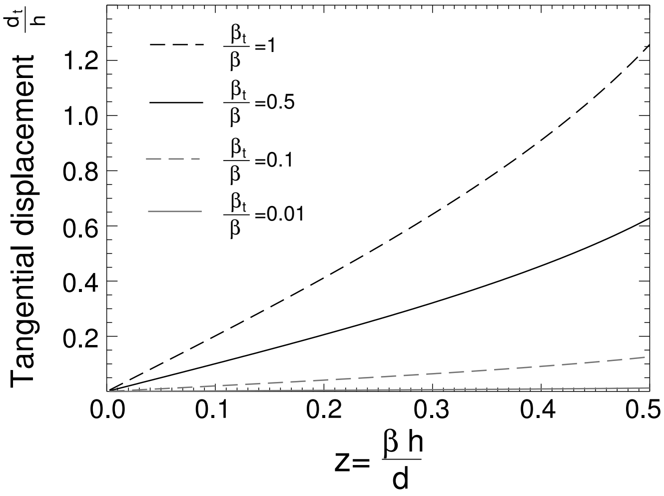

Figure 2.8: *Displacement of particle in tangential direction normalized by h.*

The tangential displacement d_t of the particle in the field $\boldsymbol{E_t}$ is:

$$d_t = \frac{e\ E_t}{m}\ t_n^2 = \beta_t \frac{v_0^2}{d}\ t_n^2, \tag{2.22}$$

where t_n – a time of flight of the particle to the surface in the fields $\boldsymbol{E_t}$ and $\boldsymbol{E_n}$. The time is written:

$$t_n = \frac{1}{\beta}\frac{d}{v_0}\left[3F_1(z) - F_1(z)\sqrt{1 - \frac{2\beta\ h}{F_1^2(z)\ d}} - 2\right], \qquad z = \frac{\beta\ h}{d} \tag{2.23}$$

where

$$F_1(z) = \frac{1}{2}\left(1 + \sqrt{1+2z}\right) \tag{2.24}$$

After substitutions we get an expression for d_t:

$$d_t = \frac{F_1^2(z)}{2\ z}\ \frac{\beta_t}{\beta}\ h \tag{2.25}$$

which does not depend on the particle energy and mass. The estimation of d_t is presented in Fig. 2.7b versus z.

Values of β_t can be comparable with the values of the field amplification factor β (section 2.5) which in turn can reach 100 or even higher. For the 1 cm gap this would mean $h = 100\ \mu$m that is already a realistic scale for a microprotrusion or a microparticle. The closeness of $z = Vh/d$ to 1 means that the potential drop over the length h in the region of protrusion is close to V.

We can see from Fig. 2.8 that the focusing of the particle flux is an effect acting on the surface area close to ($\pi\ h^2$), i.e. within the microprotrusion. The charged particle flux has a maximal value in the center of the spikes on the electrode surface which from one hand makes the spikes even more dangerous sites for initiation of breakdown, from the other - there exists another mechanism of the spikes removal in addition to the field emission effect, i.e. an additional option for conditioning.

Often an ion flux is considered to describe the cathode processes. The total effect of the ion focusing depends on the ion flux flowing towards the electrode surface. The effect can be enchanced when a high ion density is present near electrodes and one needs to account for space charge. Calculations in [56] which considered ion space charge showed that ion density in the regions of a microprotrusion is about one order of magnitude higher compared to the density in the regions of flat surface. The increase of ion density is very crucial for the start-up of breakdown processes: the electric field is enchanced in the region of microprotrusions and an increased heat flux is delivered to the tips. Based on considering of heating of the surface tips, an approach for description of processes on the electrode surface in the presence of high electric field was applied in [57]. It was shown that evaporation of the microprotrusions and consequent breakdown is possible even only by heating of the tips by ions, not accounting for field emission currents.

On the other hand, the ion bombardment of the surface tips may lead to an enchancement of field emission by excitation of metal electrons which finally results in a higher probability of the electron tunneling through the potential barier on the metal-vacuum boundary.

Thus we can draw the conclusion that the presence of the ion flux (especially a dense flux, e.g. of plasma ions) to the surface of the electrodes increases the probability of a breakdown in vicinity of the surface microprotrusions.

2.6.3 Thermal desorption and skin-effect

After exposure to the atmosphere the vacuum chamber is usually heated up to a temperature of $T = 150-250$ °C for several hundred hours to outgas the surface. A temperature of $T = 250 - 300$°C is required to initiate thermal desorption of water vapors and other weakly bound species. Even if ICRF antennas will be baked (that is not done on ASDEX Upgrade antennas), a high concentration of adsorbed species with binding energy $E_b > 2.5$ eV [58] will still exist on the walls and electrodes. The tight bonds that can not be easily broken by temperature increase can be affected by impact of particles, e.g. in glow discharge.

The other aspect to discuss is gas thermal desorption during operation of the antenna. The antenna straps are mostly current-carrying and have high RF currents (up to ≈ 1 kA for few seconds) which flow on the surface because of the *skin-effect*. The skin-depth is defined as a depth of damping of alternating current flowing on a conductor (or electrical field between conducting surfaces) by a factor of e and is determined by the relation:

$$\delta_{skin} = \sqrt{\frac{2}{\omega_0 \mu_0 \sigma}} \tag{2.26}$$

where $\mu_0 = 4\pi \cdot 10^{-7}$H/m – vacuum magnetic permeability, σ – electrical conductivity of material. For OFC copper ($\sigma = 5.85 \cdot 10^7$ (Ohm$\cdot$ m)$^{-1}$) the skin depth is 9.3 μm. For stainless steel type 430 ($\sigma = 1.67 \cdot 10^6$ (Ohm$\cdot$ m)$^{-1}$) the skin depth is 55 μm. Based

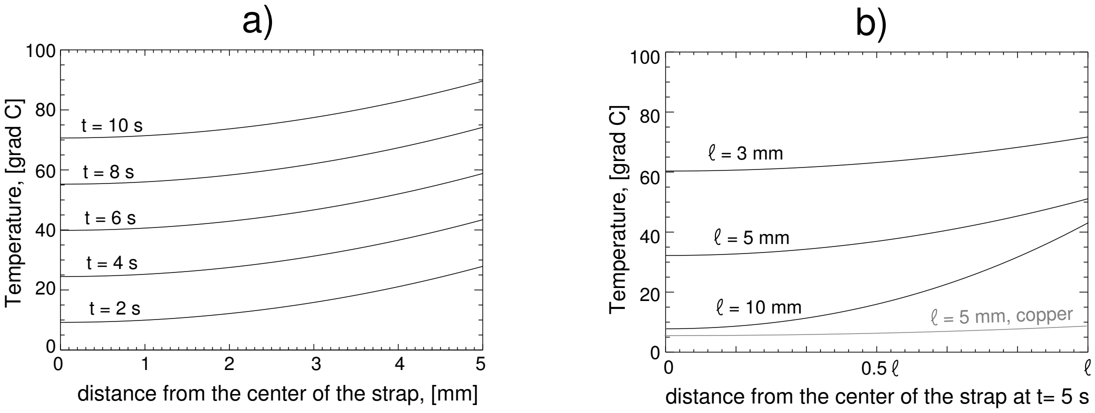

Figure 2.9: *Temperature profiles for the pulse of 1 kA RF current: a) different pulse lengths for stainless steel electrode; b) different strap thickness for 5 s RF pulse, black curves - stainless steel electrode, gray curve - stainless steel electrode with current carrying copper layer on the surface.*

on the solution of a heat diffusion equation from Appendix B, one can get the surface temperatures of an antenna strap for a pulse corresponding to the peak antenna current of 1 kA. This corresponds approximately to the antenna operation at its voltage limits.

The temperature rise is shown in Fig. 2.9 for a strap width of 20 cm. Fig. 2.9a and black lines in Fig. 2.9b correspond to an antenna strap completely made of stainless steel. The gray curve correspond to a strap with a current carrying copper layer (coating of Cu) on the stainless steel strap.

Poor heat conduction of stainless steel needs to be considered and leads to a high initial temperature of the strap: usually 40-80 ^{o}C. The initial temperature should be added to the temperature in the figure. Fig. 2.9a shows temperature for the pulses of 1 kA current with different lengths when half of the strap thickness equals to 5 mm (strap thickness for AUG ICRF antenna is about 10 mm). It is seen that the temperature profile keeps the form after 1 s pulse and increases in the absolute value.

Fig. 2.9b presents the dependence of the temperature on the strap thickness. Temperature on the surface of the strap is found to be very sensitive to the strap thickness, especially at $l < 5$ mm.

When a RF-current-carrying material is changed from stainless steel to copper (e.g. by deposition of a copper coating of several skin depths on the stainless steel electrode), the heat flux onto the surface decreases from 136 kW/m^2 to 23 kW/m^2. The change of the surface temperature decreases proportionally (see solution (B.6)).

The calculated surface temperature of the antenna may already reach the maximal values achieved when torus is baked before operation. Furthermore the rise happens during an operational pulse of the ICRF antenna and under the conditions of plasma presence during ICRF operation. The charged particles of the plasma contribute significantly to the gas desorption.

2.6.4 Particle stimulated desorption

Desorption may be initiated by the incidence of charged particles: electron stimulated desorption (ESD) and ion stimulated desorption (ISD).

As reported by Karetnikov in [59] the experimental results for ESD and ISD are rather inconsistent. Experiments reviewed in [59] show that for electron energies from 1 keV to 75 keV from different materials (stainless steel, molybdenum, copper, titanium) gas yield by ESD varies from 1 to 10 desorbed species per incident electron. Desorbed substances, such as H_2, CO, CO_2, CH_4, O_2, H_2O were observed in neutral as well as in ionized state. Thus one electron can lead to the emission of more than one ion or neutral from the electrode.

Experiments of ISD were reviewed also by McCracken and Stott in [58]. Yield of desorbed neutrals up to 10 molecules per ion were reported for bombarding electrodes by hydrogen ions (which are of interest for our discussion). The experiments did not show a strong dependence of gas desorption on the electrode material for various incident ions.

According to experiments listed in [58] and [59] both for ESD and ISD, conditioning brings a strong reduction of the desorption yield by orders of magnitude. The most successful degassing and conditioning procedures were baking and glow discharge cleaning.

2.6.5 Secondary emission processes

The charged particles are not always adsorbed by the walls. One can speak about dominant absorption of charged particles by the walls if secondary emissions coefficients are below unity. The main secondary emission processes include: electron-electron emission, ion-electron emission, ion-ion and neutral-ion emission. At high energies (at least few hundred eV) ions and neutrals may also sputter the surface of the electrodes and lead to the appearance of the surface material ions and vapors.

The surface of the electrodes usually consists not only of the bulk material, but of some oxides, nitrides etc. Bulk materials and the chemical bonds on the surface have secondary emission coefficients which do not stay below one for the whole range of energies of charged particles.

Electron-electron emission yield often has a maximum of about 1 to 2 at the energies of the order of few hundred eV [60, 61] and a strong dependence on the angle of electron incidence [61, 62]. For example, for polished stainless steel the secondary electron coefficient varies from 1.5 to 1 for the energy range from 200 eV to 1 keV [62]. For the angles of incidence of 55^o-60^o the yield is increased by approximately 20-30% for stainless steel and some other materials, e.g. tungsten.

When the incident electron energy is increased, the yield of the electron-electron secondary emission decreases simultaneously with increasing the fraction of the electrons which are redifused back to the surface after some cascades of elastic or/and inelastic collisions in the metal [60].

Secondary emission yield per ion has significantly higher values than that per electron. Ion-electron emission yield is typically from 0.5 to 5 for single charged ions at energies higher than 1 keV [61]. The yield grows with the incident ion energy and the maximum takes place at the energies from 50 to 100 keV. The maximum yield depends very much on the type of incident ions and the surface material but is usually below 10.

2.6.6 Multipactor in vacuum

The high yield of the secondary electron-electron emission may give rise to a specific effect - a *multipactor* - an effect of the resonance movement of electrons in the vacuum gap in the applied RF electric field accompanied by emission of the electrons from the electrode surface. In other words during half of RF period electrons have a displacement value close to the gap distance. On a surface with a secondary emission coefficient larger than 1, the electrons increase in number after colliding with the electrode surface and can start moving back to the opposite electrode exactly at the moment of electric field reversal.

The multipactor exists in rather narrow range of voltages, the resonance values of which are set by frequency of RF voltage and geometry, i.e. gap distance. In Fig. 2.10 (see below) the electron multipactor in vacuum is shown with the experimental data from [22, 63] for the 5.5 cm gap.

We consider multipacting as one of the parasitic RF effects appearing which does not lead directly to the breakdown. However the effect is one of the components of the chain of phenomena which may influence the probability of the high voltage breakdown through a change of the parameters like neutral gas pressure and initial plasma density. It can be even more critical, because the multipactor represents a mechanism of confinement of electrons, though it exists at rather low voltages.

There are important features of multipactor in magnetic field which are discussed in section 3.4.3.

2.6.7 Mean free-pass and cross-sections of ionization processes

Pressure of neutral gas defines the frequency of electron-neutral and ion-neutral collisions that may lead to ionization or to a charge exchange process. An ionization avalanche [21] is responsible for the gas breakdown and formation of the self-sustained discharge. The processes depend strongly on the energy of the particles. The energy dependence is important for the breakdown of gas at high RF voltages.

At low electron energies (typically ε_e <10 eV) the elastic collisions play a dominant role in collisional processes. The mean free pass of electron at 1 Pa pressure varies from few cm to few tens of cm depending on the gas (see Appendix C).

When energy of electrons is increased, they collide less frequently by elastic scattering while the probability of inelastic processes grows. These processes are: excitation of electrons in atoms, transition to vibrational or rotational states in molecules, dissociation of molecules, or eventually ionization of molecules or atoms. At high energy also cross sections of ion-neutral collisions increase to considerable values. We also need to keep in mind that excitation of neutral particles may lead to the so-called multi-wise ionization (Penning effect) [21], and the effect is more pronounced for such gases as argon and nitrogen than for gases of hydrogen isotopes and helium (more electron states available for the effect which has a resonance nature). It can contribute also when, for example, neutral gas consists not only of hydrogen isotopes, but of impurity gases with a higher mass. In other words impurity atoms (C, Ar, ...) and molecules (N_2, $C_\alpha H_\beta$, $C_\alpha D_\beta$...) have more degrees of freedom resulting in a high probability of the step-wise ionization due to the interaction of excited atoms or molecules in metastable states with other heavy species.

A comprehensive description of elementary collisional processes and ways of measurements of probabilities of the processes can be found in [64, 65, 66]. The data on electron-neutral collisions at low energies, ionizing electron-neutral collisions and ionizing proton-neutral collisions are presented in Appendix C.

2.7 Self-sustained RF glow discharge

The strap of the ICRF antenna presents an electrode with a transition from high RF current to high RF voltage. The transition can be interpreted as a transition from an inductive coupling (power can be locally coupled to plasma by interaction of RF magnetic and induced electric fields with charged particles) to a capacitive coupling (local coupling of the power to plasma by high RF electric fields).

At first we will clarify the role of the inductive coupling for the ICRF antenna. Then such features of the capacitevely coupled discharges as a multipactor plasma, a pressure hysteresis for the ignition and the sustainment of the discharge and an application of the discharge for conditionning are discussed.

2.7.1 Role of inductively coupled discharge

In the inductively coupled discharges, the induced electrical fields transfer the power to electrons. High voltage sheaths do not form near the electrodes in these discharges (see e.g. [34]) and generally the power efficiency for the plasma generation is higher than in the capacitevely coupled discharges. The inductively coupled discharges can also exist at lower pressures.

In the external DC magnetic field the charged particles are confined (see section 3.4). Electrons can not be efficiently accelerated by the induced electric field if the field has a small component parallel to the external magnetic field. The use of poloidal straps for the ICRF antenna leads mainly to an induction of poloidal electric fields that are almost perpendicular to the external magnetic field.

The parallel RF electric fields are associated mainly with the RF voltage on the strap. Therefore we limit ourselves by the description of the high voltage electrodes and the capacitively coupled plasmas.

2.7.2 Capacitively coupled discharge

As a result of ionization and secondary emission (γ-) processes, a self-sustained glow discharge can be ignited. This is a discharge initiated without the "help" of an external source of ionization. According to the Townsend theory [21] the RF breakdown is initiated

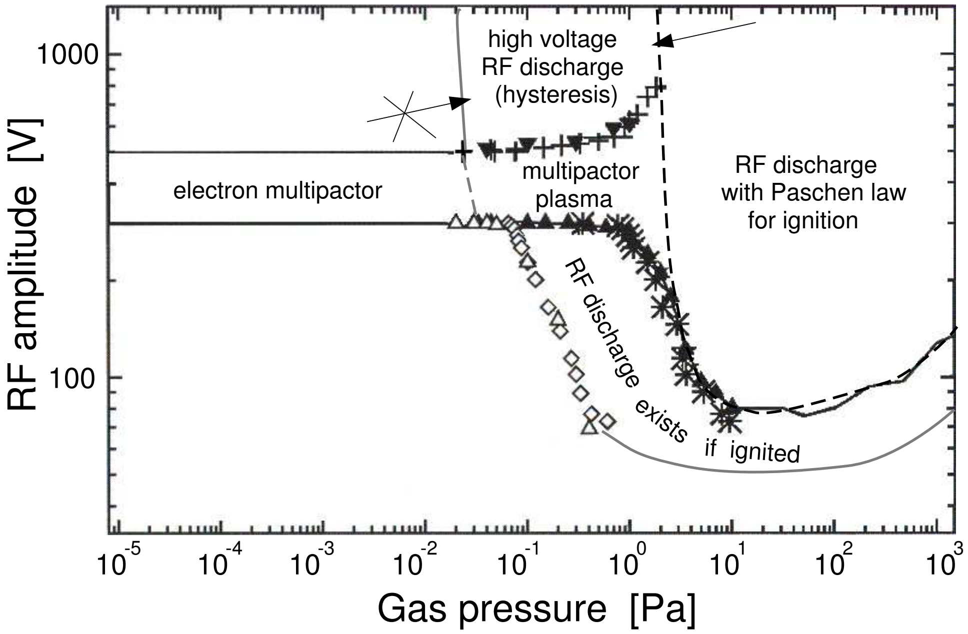

Figure 2.10: *Pressure dependence of voltages of existing forms of RF gas discharge in the region of multipactor [22, 63].*

by an ionization avalanche. The discharge ignition is often described by the well-known Paschen-curve [21]. This curve gives the dependence of ignition voltage vs. product of pressure and the gap distance or versus pressure at the given gap distance (for an example look in Fig. 2.10, black dashed line). Along the Paschen curve the discharges have some peculiarities. A knowledge about the forms and features of the RF glow discharges which may exist in the electrode gap will help us to come closer to the question of the discharge initiation that is discussed later in this chapter and in chapter 3.

A self-sustained capacitive RF glow discharge exists in two forms: α and γ. In the α discharge in the planar system the charged particles are mainly produced by electron impact ionization in the region of the quasineutral plasma. Time averaged potential drops on the sheaths provide a confining potential well configuration for electrons which are accelerated in the weak electric field inside the quasineutral region (compared to the electric fields in the sheaths). However the potential drop inside the plasma exceeds the ionization potential of gas. Electrons (and therefore quasineutral plasma since ions move slowly) are oscillating near the electrodes uncovering and covering in sequence ion space charge. The averaged plasma (ion) densities are mostly "bell-shaped" [38, 68] - with a maximum in the center of the gap. The electrode sheaths play the role of capacitances and contribute to the displacement RF current. Conductive RF current, i.e. current transferred by charged particles is negligible in the sheath of α discharge. The α discharge is dominated by volume ionization that requires rather high ionization probability.

A transition to the γ-regime [68] happens usually at high voltage drops on the sheaths and is often associated with a breakdown of the sheath, hence at high voltage the α-regime may be present only for a short period before the transition to the γ-discharge. In the γ discharge the mechanism of electron birth by secondary emission plays a significant role. At the pressures $p \sim$10-100 Pa (we consider only pressure from the range $p \approx 0.1 - 100$ Pa) the γ discharge is similar to the DC glow with a cathode potential drop. This means that the cathode sheath is self-adjusted in order to have optimal conditions for the generation of charged particles in it by ionization and ion-electron secondary emission. The conditions correspond to the operation in the minimum of Paschen curve for the sheath. The averaged plasma density profile normally has two maxima in vicinity of each of the electrodes.

A RF discharge at the left branch of the Paschen curve and at substantially high voltage exists in the γ-form and is characterized by other similarities with DC glow discharges. Electrons pass the electrode gap in a time shorter than characteristic time of the change of external electric field, i.e. the voltage is quasi-constant. However neither in DC nor in RF case a creation of the effective cathode sheath is possible in the left branch of the Paschen curve. The mean free pass is comparable with the interelectrode distance and the sheath thickness required to provide optimal conditions for ionization is larger than the distance. To ignite such a discharge both secondary emission and volume ionization are important and the Paschen curve at high voltages has a threshold dependence on pressure. The threshold pressure depends very much on the gas [69] for the high voltages.

Most of the experimental data exists for voltages below 1 keV. From the experiments in [70, 71] it is clear that, at the left branch of the Paschen curve, effects connected with secondary emission processes can take place. At voltages of few hundred volts there often exists a region where the ignition voltage has a weak dependence on the pressure (ignition voltage is almost constant for a range of pressures). The dependence does not follow the classical Paschen curve behavior at the left branch. By insulating the electrodes with glass plates [70] it was possible to determine that the reason for the behavior is really the secondary emission. The γ processes participate in the ignition and sustainment of the discharge by multiplication of the electrons in the gap. According to section 2.6.6, for the RF voltage the movement of the electrons may be in a resonance with the external electric field. The effect may be coupled to collisions of electrons with neutrals.

2.7.3 Multipactor plasma discharge (multipactor affected by gas)

Electron multipactor transforms to the multipactor plasma when the pressure is increased (for experiments in [63] it is $3 \cdot 10^{-2}$ Pa Fig. 2.10). The multipactor plasma is a form of RF glow discharge when electrons undergo collisions with neutral particles and change their velocity in projection transversal to the electrode gap. This way electron displacement stays close to the gap distance even if the voltage does not fit exactly to the resonance condition. This leads to a widening of the voltage range required for the resonance condition to be fulfilled when one operates at higher pressures ($\approx$1-3 Pa in the figure) and a weaker pressure dependence on the left branch of the Paschen curve.

The work [22] gives an overall picture of the secondary emission effects contributing to the ignition of the RF glow discharge. This is confirmed by the experimental observations [70, 71].

2.7.4 Pressure hysteresis for RF discharge existence

In the above mentioned experiments [63] (Fig. 2.10) the hysteresis of discharge ignition and extinguishment is observed (see black arrows in the figure). When the discharge is already ignited, its extinguishing happens at a pressure about one order of magnitude lower than the ignition pressure.

The hysteresis explains the possibility to ignite the so-called *semi-self-sustained* discharge that appears as a consequence of the application of a voltage to the electrode gap during existence of an external plasma (ionizing) source.

The hysteresis is explained by the increased charged particle fluxes which still can sustain a high number of ionization events in the volume as well as high secondary emission currents when one decreases the pressure after the discharge ignition. Obviously for the low voltage case, electron impact ionization and electron-electron secondary emission are mainly responsible for the production of charged particles. The high voltage case is somewhat different because, for example, processes initiated by fast ions may play a considerable role.

Using the knowledge for the high voltage case from section 2.6, data on secondary emission, data on collisions summarized in Appendix C, one can make a few statements concerning the initiation of the ionization avalanche leading to the high voltage self-sustained RF discharge (high-pressure side of the hysteresis on the pressure axis) and the existence of the plasma (low-pressure side).

Ignition of RF discharge (high pressure side of the hysteresis)

Some features (mainly connected with probabilities of electron- and ion- impact ionization) should be noted for the cases when light or heavy neutral gas is used as a working medium.

Heavy neutrals. After ionization by electron impact, heavy ions do not acquire high energy from RF field during RF period. The ions do not reach energies that are sufficient for an increase of the cross-section of ion-neutral collisions. Also the energies are not sufficient to get a high ion-electron emission yield. Electron impact ionization and electron-electron secondary emission can be considered as the main sources of charged particles.

Light neutrals. At high RF voltage the main electron source is field emission. The field emission current starts from applied voltages of at least a few kV and depends exponentially on the voltage. Therefore the emitted electrons have a very narrow energy range since they are mainly emitted when the voltage reaches its maximum. The typical energies of electrons contributing to dark field emission (self-sustained) current are in the range from a few keV to a maximal value corresponding to the RF voltage amplitude. This is far from the optimal energy for the electron impact ionization. However the ionization is the only source of ions. Ion-neutral ionization is a "second-order" effect, because ion density is substantially lower compared to the electron density. Therefore, as the probability of ionization is proportional to the density, the electron impact ionization of neutrals (despite unfavorable conditions) is the dominant ionization process. Ion-electron secondary emission (though the ion current density is small) is increased to values above unity at high energies and partly compensates for the low ion density, and therefore plays a role as well as electron-electron secondary emission (but in the energy range of low emission yield).

Sustaining or ignition of the semi-self-sustained RF discharge (low pressure side of the hysteresis)

If a source of external plasma exists, the value of the injected ion density is close to the electron density along the most part of the gap. Light ions can be successfully accelerated in high RF fields to relatively high energies where the cross-sections of ion-neutral collisions as well as the yield of secondary ion-electron emission are high. The energy spectrum of electrons and ions is not the same as in the case of the self-sustained current, i.e. far from the monoenergetic spectrum. The external injector works during the whole RF cycle and particles of different energies are present in the gap. This means that the conditions for an operation at optimal electron energies for the impact ionization and electron-electron secondary emission exist. Thus the conditions are more favorable for ignition of RF gas discharge or the discharge is more easily sustained if it is already ignited.

Role of secondary emission from the anode

Secondary electrons emitted after electron incidence to the anode do not participate in the ionization processes if the instantaneous voltage on the electrodes is high. According to (2.18) secondary electrons mostly return to the anode surface. The electric field can be assumed constant for the electron timescale (2.16) and secondary electrons are reflected back to the anode surface with the same speed they were emitted from the surface. The low energy electrons are lost on the electrodes.

2.7.5 RF gas discharge conditioning

When the discharge exists in the gap the electrodes are bombarded by intensive electron and ion fluxes. This leads to a particle stimulated desorption from the electrodes, surface sputtering and some changes of microgeometry on the electrode surface. The chemical properties of the surface are changed since structure of the surface is modified and impurities are removed. All this coupled together leads to a decrease in emissive and sorption properties of the surface. For this reason the RF gas discharge can be used very efficiently for conditioning of electrodes.

2.8 Summary

The power transmission from RF generator to plasma by ICRF transmission lines and antenna can be limited by the parasitic RF breakdown in the RF system and, in particular, on the antenna. There exists a number of effects which may assist or lead to the high voltage ICRF breakdown that should be taken into account simultaneously. RF vacuum arc, RF glow discharge - self-sustained and semi-self-sustained are the candidates that may lead to arcing on the antenna.

High voltage operation makes restrictions on the surface state of the electrodes. Initiation of breakdown happens typically at the emission centers where the work function is low (or where a non-metallic impurity inclusion exists which makes the electron tunneling easier through interfaces) and/or microprotrusions are present which increase field emission currents from the surface.

We also have concluded that such ions as H^+, H_2^+, He^+ can not be considered completely motionless during the RF period of the high electrical fields.

When external plasma appears in the electrode gap, a few additional mechanisms can be triggered simultaneously. We have reviewed the most important ones:

- increase of charged particle fluxes to the surface, local focusing of the fluxes to microprotrusions;
- particle stimulated desorption;
- enchanced production of charged particles in the volume and by secondary emission;
- ignition of semi-self-sustained RF gas discharge.

The processes listed make one think about an improvement of vacuum conditions in the region of the ICRF antenna that carries high RF currents and is heated.

One of the main processes, the amplification of electrical field on the surface by space charge effects, is important but not listed above. It is discussed separately in the next chapter.

Chapter 3

Plasma in the electrode gap

When plasma is present in the electrode gap, the electrical fields on the electrodes may become significantly higher than the vacuum fields. Ignition of arcs on the surface of the electrodes is directly dependent on the surface electric field. This makes it important to clarify the characteristic behavior of the fields during a RF period and the influence of the RF field on the densities of ions/electrons in the sheath and on the density of the quasineutral plasma.

In section 2.6 some attempts were made to understand the influence of the presence of charged particles on the formation of an arc when the influence of space charge is negligible (i.e. condition (2.21) is fulfilled). Now we initially assume that space charge can be present in the electrode gap and the condition (2.21) is not fulfilled. However we consider the neutral pressure to be low enough for all types of particle-particle collisions to be negligible in the near-electrode regions (sheaths) of the gap where spatial charge is present. The potential distribution and the flows of charged particles to the electrodes depend strongly on the density of a plasma which is sustained by a plasma source. The latter is considered external, though the following description is also suited for the plasma sustained by volume ionization in the region of quasineutral plasma of the electrode gap.

At first we discuss sheath theory in the case of no magnetic field. That is practically the same as in the case when magnetic field lines are not nearly parallel to the electrode surfaces since plasma diffusion parallel to the electrodes is not considered in the 1-D models being used.

3.1 Approach to a DC sheath

No voltage is applied to the electrodes

If no voltage is applied to the electrodes, the plasma density in a gap is determined by the balance between the plasma flow from the source and ambipolar diffusion of plasma that leads to losses of the charged particles on the electrodes. The plasma inside the gap can sometimes be considered to be in a thermodynamical equilibrium for the ion and electron components.

As electrons have a much smaller mass than the mass of ions, for the same energy electrons are much faster. The electron mean energy often defines the plasma properties. Maxwellization of the electron energy distribution is associated with electron-electron collisions. We assume that the external plasma source contains initially thermalized electrons and ions. Therefore the electron-electron collision time τ_{ee} can be evaluated by applying the concept of electron temperature T_e (energy distribution function is initially close to the maxwellian):

$$\tau_{ee} \approx 3.45 \cdot 10^{11} \frac{(T_e,\ [\mathrm{eV}])^{3/2}}{\ln\Lambda \cdot n_e,\ [\mathrm{m}^{-3}]},\ [\mathrm{s}];\ \ \ln\Lambda = 24 - 0.5\ \ln n_e -\ \ln T_e, \tag{3.1}$$

where $T_e \gtrsim$10 eV, n_e – electron density, ln Λ - Coloumb logarithm. For T_e = 15 eV, n_e=10^{16} m^{-3} one estimates $\tau_{ee} \approx 62$ μs that is much longer than the RF period (e.g. 20 ns for 50 MHz). Thus non-maxwellian electrons can be thermalized only if a configuration of electric field exists in the gap which confines electrons for several RF periods.

If electron collisions with the heavy particles are elastic, the energy transfer from electrons to the heavy particles is very small, though a one-dimensional component of the velocity is broadened (but does not thermalize).

When $T_e \gtrsim T_i$ (T_i – ion temperature), electrons are lost on the walls more frequently. The loss of electrons charges the plasma to some positive potential. The plasma tends to be quasineutral and a voltage drop is formed on a thin sheath of positive (ion) spatial charge between the plasma and the electrode forming a "bell-shaped" configuration of potentials that partially confines electrons inside the gap. The sheath has a thickness of:

$$\lambda_{De} = \sqrt{\frac{\epsilon_0 k T_e}{n_e e^2}} = 7.43 \cdot 10^3 \sqrt{\frac{T_e,\ [\mathrm{eV}]}{n_e,,\ [\mathrm{m}^{-3}]}}\ ,\ [\mathrm{m}] \tag{3.2}$$

Here λ_{De} - is the so-called electron Debye length. For typical electron temperatures of T_e = 15 eV and plasma densities $n_e > 10^{14}$ m^{-3}, the Debye length λ_{De} <0.29 cm and is thus significantly smaller than the gap distance of few cm. When an electrode is electrically insulated from any surface with a defined potential, the electrode is floating. The potential drop between the electrode and plasma (assuming singly charged ions with adiabatic index of 3) is [73]:

$$V_{sh} \approx -\frac{kT_e}{2e}\ \ln\left(2\pi\frac{m_e}{m_i}\Big(3\frac{T_i}{T_e}+1\Big)\right) \tag{3.3}$$

For cold ($T_i \ll T_e$) deuterium ions one gets $V_{sh} \approx 3.2\ kT_e/e$. For a system with insulated electrode, no steady-state electric current flows through the gap. This means that the potential drop (3.3) appears in order to reflect electrons from the electrodes and make the electron current to the electrodes equal to the ion current.

If the circuit is closed, electron currents may flow to each of the electrodes (see Fig. 3.1a). The voltage drop on the sheaths is reduced compared with expression (3.3), but is still of the order of T_e/e. The net electron current is zero if both electrodes of the gap are completely identical (Fig. 3.1a). If one of the electrode has a larger area, as in Fig. 3.1b, it collects more electrons and the plasma induces a small net current between two electrodes. A positive net current flows externally from the small electrode to the large one.

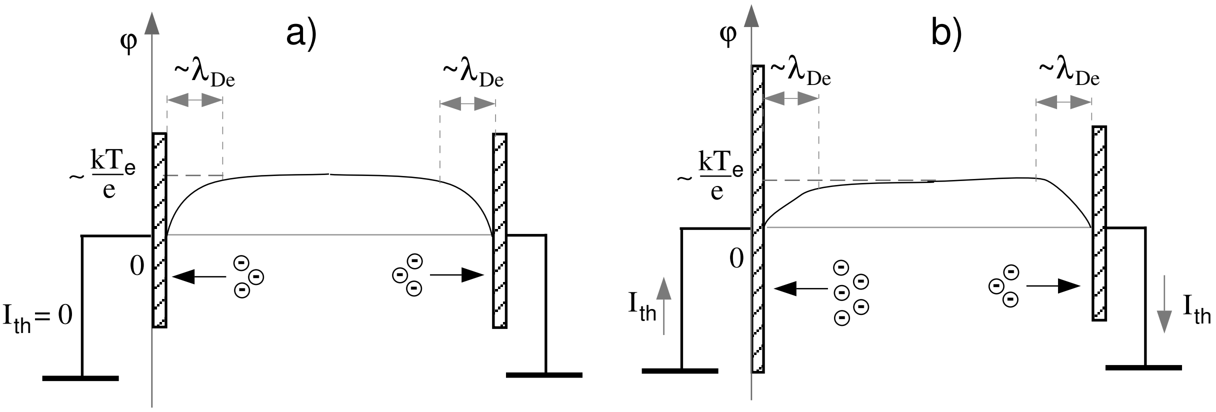

Figure 3.1: *a) Completely identical electrodes, no net electron current; b) electrode areas are different, net electron current exists.*

Common approach to a DC sheath

When a voltage is applied to the gap, the sheath thickness and the appropriate potential drops are changed. Though Debye length is small, the thickness of the screening non-quasineutral sheath is larger when a high voltage is applied to the electrodes. To get the parameters of the RF sheath like the thickness, the voltage drop and eventually the surface electric field, we describe briefly the common approach to the characterization of a DC sheath which we are using appropriately for some of the RF sheath issues.

The electron density in the ion sheath is usually described by a Boltzmann equilibrium:

$$n_e = n_0 \exp\left(\frac{e(\Phi - \Phi_p)}{kT_e}\right) \tag{3.4}$$

where Φ_p - potential of quasineutral plasma. The Boltzmann law can be used when electrons are assumed adiabatic.

The description of the ion density n_i is usually not straightforward if the first approximation of n_i =const (the assumption of *ion matrix sheath*, see, e.g. [34]) is not used. To define the ion density the continuity equation:

$$\frac{\partial n}{\partial t} + div(n \cdot v) = S \tag{3.5}$$

where S - particle sources, is often used for the stationary case $\partial n/\partial t = 0$ together with an expression for energy conservation.

Electron and ion densities are substituted into the Poisson equation:

$$\Delta\Phi = -\frac{e}{\epsilon_0}(n_i - n_e) \tag{3.6}$$

In particular, one-dimensional models are used. It can be shown (e.g. [34]) that for the formation of an ion spatial charge it is necessary (in the collisionless case) that ions have initially high velocities at the boundary between the quasineutral plasma and the sheath:

$$v_i \geqslant v_B = \sqrt{\frac{kT_e}{m_i}} \tag{3.7}$$

where v_B is the Bohm velocity. Expression (3.7) is called the Bohm criterion[1]. Acceleration of ions to the required velocity occurs in the so-called *presheath*. The presheath is quasineutral but a finite electric field exists inside it which "drives" ions to the velocity v_B. The dimensional scale of the presheath is much larger than λ_{De} and is of the order of d [74].

Thus the criterion (3.7) should be fulfilled if a sheath of ion spatial charge is formed. However the formation of the sheaths should be discussed separately when a RF voltage is applied to the electrodes, though approximately the same approach can be used further.

3.2 A RF sheath: frequency ranges

Properties of a RF system depend strongly on the frequency range of operation. The plasma frequencies, in particular:

$$\omega_{pe} = \sqrt{\frac{\epsilon_0 e n_e}{m_e}}; \qquad \omega_{pi} = \sqrt{\frac{\epsilon_0 e n_e}{m_i}} \tag{3.8}$$

should viewed as characteristic timescales of electrons and ions respectively.

There exists another characteristic frequency, namely the frequency of collisions of electrons with heavy particles, in particular with neutrals $\nu_{en} = n_n \; v_e \; \sigma_{en}$, n_n – neutral density. We assume ν_{en} is the highest from the collision frequencies (see also Appendix C). In the sheath or in the cases when electron leaves the gap in a time shorter than $1/\nu_{en}$, the collisions are negligible if the neutral pressure is low. Therefore there is no need to account for collisions in the region of space charge near to the surface of the electrodes, i.e. in this chapter.

3.2.1 Comparing ω_0 with ω_{pe}

Let us start with the assumption n_i=const. The assumption is rough but convenient for the initial stage when basic sheath properties are studied.

From section 2.6 we know that electrons oscillate with the displacement $d_e = eE_p/m_e\omega_0^2$ in the RF electric field E_p. We assume E_p is the RF field in the plasma. The electric field in regions of spatial charge is defined by the ion density n_i: $E_{sh} \approx en_i s/\epsilon_0$, where s is the thickness of the sheath defined by approximately the electron displacement d_e.

---

[1] Expression (3.7) is written for the assumption $T_e \gg T_i$ (see, e.g. [73]). We assume here and below that the condition $T_e \gg T_i$ is fulfilled, though we keep in mind that a higher ion temperature T_i can result in a higher ion velocity (and current) at the boundary of the quasineutral plasma and therefore in a higher ion density in the sheath.

Setting $s = d_e$ one gets:

$$\frac{E_{sh}}{E_p} \approx \frac{\omega_{pe}^2}{\omega_0^2} \tag{3.9}$$

This ratio defines the amplitude of electrical field in plasma E_p compared to the sheath electric field E_{sh}. Low values of E_p mean that RF electrical field is screened near RF electrodes, high E_p values correspond to the penetration of electrical field into the plasma. The condition of total screening of RF field $E_{sh} \gg E_p$ or $\omega_{pe} \gg \omega_0$ is actually the condition of the total reflection of electromagnetic field from the plasma.

$\underline{\omega_0 < \omega_{pe}}$

The plasma is capable to screen the electric field. If $E_{sh} > E_p$, plasma electrons respond to external RF electric field of arbitrary magnitude, and therefore the external electrical field does not penetrate into plasma deeper than the screening sheath thickness. Also electron density and fluxes are quasi-stationary. Appropriately this means densities above $5 \cdot 10^{12} - 10^{14}$ m^{-3} for f_0 =20-120 MHz. As we will see in chapter 5 the condition for the density is fulfilled for the location of ICRF antennas on ASDEX Upgrade and for the experiments conducted in the frameworks of this thesis.

Densities above $8 \cdot 10^{12}$ m^{-3} correspond to the case $\lambda_{De} < d$, where $d \approx 1$ cm – interelectrode distance, T_e is taken 15 eV. However the sheath thickness s may be either smaller than d or larger than d depending on instantaneous voltage applied to the electrodes. The discussion on the comparison of s with d follows in section 3.3.

$\underline{\omega_0 > \omega_{pe}}$

The screening capabilities of the plasma are reduced. If $E_{sh} < E_p$, the electrical field starts penetrating into the plasma since electrons are too slow compared with the time of change of the electric field. For the frequency range of interest 20-120 MHz the condition means that electron density should be lower than $5 \cdot 10^{12} - 10^{14}$ m^{-3} respectively.

Densities below $8 \cdot 10^{12}$ m^{-3} correspond appropriately to $\lambda_{De} > d$ and $s > d$ for the usual parameters. The charged particles are moving in the gap according to the vacuum electrical field distribution and spatial charge effects are neglected. The latter statement is provided by $s > d$ and is applicable for the higher plasma densities unless voltage on the electrodes is high enough (see also condition (2.21)).

3.2.2 Comparing ω_0 with ω_{pi}

Comparison of ω_0 with ω_{pi} requires initially the condition $\omega_0 \ll \omega_{pe}$ to be valid. This condition and $\lambda_{De} < d$ are assumed everywhere here on.

It was shown in [75] that the Bohm criterion (condition 3.7) is valid for RF sheath, non-modified in the case $\omega_0 \ll \omega_{pe}$ for the arbitrary ratio ω_0/ω_{pi}: the sheath of positive spatial charge is present in this frequency range.

Displacement of an ion in the sheath is $d_i = eE_{sh}/m_i\omega_0^2$, where $E_{sh} \approx en_i s/\epsilon_0$. For the ratio of the displacement d_i and sheath thickness s one gets:

$$\frac{d_i}{s} \approx \frac{\omega_{pi}^2}{\omega_0^2} \tag{3.10}$$

Therefore the ratio ω_0/ω_{pi} defines the displacement of an ion compared with the sheath thickness.

The condition $\omega_{pi} = \omega_0$ for $f_0 = 20 - 120$ MHz means in terms of ion density in the sheath:

$$n_i,\ [\mathrm{m}^{-3}] = (9 \cdot 10^{15} - 3.3 \cdot 10^{17}) \cdot \mu_i \tag{3.11}$$

where μ_i - ion to proton mass ratio. Higher densities correspond to the condition $\omega_0 < \omega_{pi}$, lower to $\omega_0 > \omega_{pi}$.

$\underline{\omega_0 < \omega_{pi}}$

Ions acquire energy on the RF timescale for arbitrary RF electric fields. Positive space charge prevails in the near-electrode region. In this case the sheath evolves as a quasi-stationary (DC) sheath and Langmuir probe theory is applicable. This condition means also smallness of the capacitive RF current through the sheath compared to the current carried by charged particles.

$\underline{\omega_0 > \omega_{pi}}$

In this range ions can be assumed almost motionless on the RF scale since a displacement of a single ion during RF cycle is lower than the sheath thickness and therefore much lower than the gap interelectrode distance. In this case ions respond mainly to time-averaged electric fields. If $\omega_0 \gg \omega_{pi}$, many theoretical models use only the time-averaged electric fields to describe the ion density.

The condition $\omega_0 \gg \omega_{pi}$ is fulfilled for RF glow discharges for heavy ($\mu_i > 10$) gases. For hydrogen and its isotopes the condition may not be so strict as for the heavy gases, e.g. *Ar* used in the etching/coating reactors based on the capacitive RF glow discharges [68]. Moreover in the limiter shadow of ASDEX Upgrade, where ICRF antenna is situated, the range of the densities is broad (see section 5.3.1) and the condition may be fulfilled only for certain plasmas or for a limited time interval.

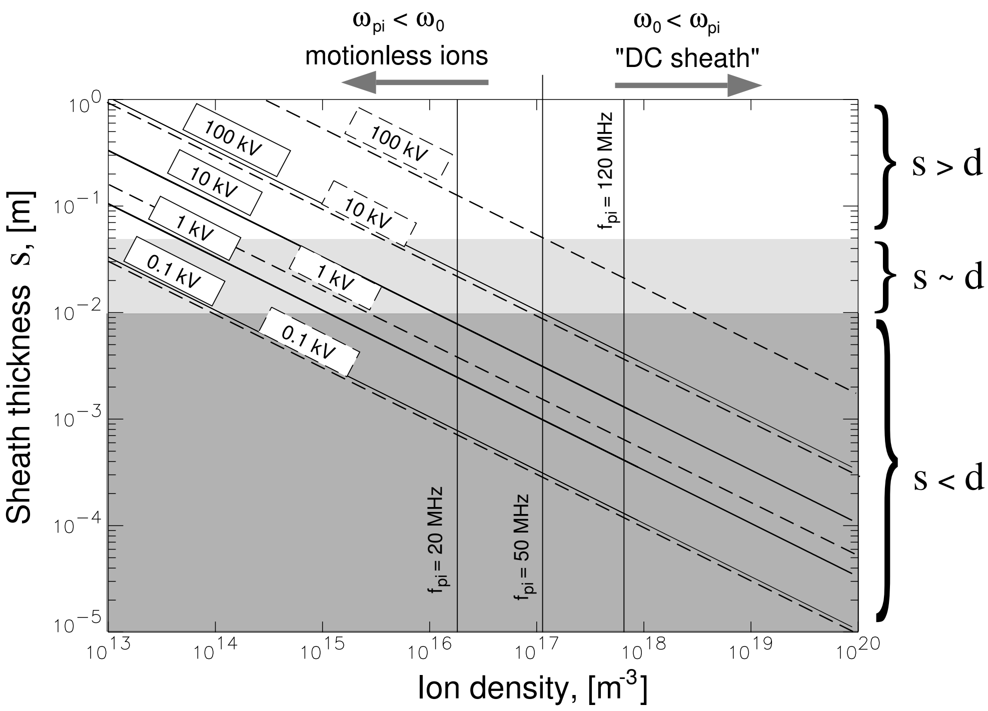

Figure 3.2: *Sheath thickness versus ion density. Solid vertical lines - boundaries* $\omega_0 = \omega_{pi}$*. Solid lines - sheath thickness for different voltage over the sheath for* n_i*=const and (3.12). Dashed lines - sheath thickness according to (3.18),* T_e*=15 eV, when the ion density is reduced.*

3.3 Plasma screening properties

The electrode gap has a spatial parameter - gap distance d which is as important for electrical field screening as the ratios between the generator and the plasma frequencies noted above. The thickness of the screening non-quasineutral sheath depends on the voltage applied to the electrodes, though the electron Debye length is small. The sheath thickness is also defined by the ion density which has a relation to the density of quasineutral plasma. Therefore, depending on the plasma density, the high voltage sheath may cover either a small part of the gap or it can be thick enough to cover the whole gap.

Thus the sheath thickness should be compared to the gap distance. The sheath thickness can be easily derived from the Poisson equation (3.6) for the case of n_i=const (see e.g. [34]):

$$s = \sqrt{\frac{2\epsilon_0(V_p - V)}{en_i}} = \lambda_{De}\sqrt{\frac{2e(V_p - V)}{kT_e}}, \tag{3.12}$$

where V_p is the potential of the quasineutral plasma and $(V_p - V)$ is the voltage across the sheath. Two density regimes can be identified:

- the high density case, when the maximal sheath thickness is much smaller than the gap distance $s < d$, *the thin sheath*;
- the low plasma case, when the sheath is larger than $s > d$ for the most part of RF cycle, *the thick sheath.*

The estimation of the ion density for each of these two cases can be understood from Fig. 3.2 where the sheath thickness (3.12) is presented versus n_i for n_i=const by solid lines. One can see that the case $s > d$ is only possible when $\omega_0 \gg \omega_{pi}$. The case $s < d$ takes place both for $\omega_0 > \omega_{pi}$ and for $\omega_0 < \omega_{pi}$.

For the case $s < d$ the vacuum electrical field is strongly changed by the field spatial charge. This leads to an increase of the electrical field on the electrode surface. One can estimate this increase by using simple sheath models.

3.3.1 Electrical field for the thin sheath ($s < d$)

The maximal electric field E_{el} on the electrode surface in the case n_i=const estimated from the Poisson equation is:

$$E_{el} = \sqrt{\frac{2en_i}{\epsilon_0}} \cdot \sqrt{V_p - V} = \frac{2(V_p - V)}{s} \tag{3.13}$$

where sheath thickness s is expressed by (3.12).

The electric field (3.13) is high compared to the electric field when no plasma is present in the electrode gap. In vacuum the voltage drop corresponding to RF amplitude V_0 linearly covers the gap. As we will see below, in the presence plasma voltage about V_0 can be dropped on the sheaths near electrodes. If $(V_p - V) \sim V_0$, one sees from (3.13) that the electric field in the plasma case is twice higher than in the case when the voltage is dropped over a vacuum gap with the size s.

Another important feature is that the electric field on the surface of electrodes is dependent on the square root of the voltage V. This means E_{el} grows more slowly than linearly with V.

The assumption n_i=const is too simplified, because the ion density in the sheath has a certain distribution and it decreases to the direction of the electrode due to closeness of ω_0 to ω_{pi} and the acceleration of ions. To describe the ion density the continuity equation can be used as for DC sheath (3.1). For stationarity of the ion movement we get $n_p \cdot v_B = n_i \cdot v_i$. Using the energy conservation one can derive the ion density in the sheath and substitute it into the Poisson equation neglecting the electron density in the sheath for the high-voltage approximation:

$$\frac{d^2\Phi}{dx^2} = \frac{e}{\epsilon_0} n_p \left(1 - \frac{2e(\Phi - V_p)}{m_i v_B^2}\right)^{-1/2} \tag{3.14}$$

where Φ is a potential in the sheath, V_p is a potential of the quasineutral plasma. After integrating once and applying $d\Phi/dx = 0$ at $\Phi = V_p$ one gets:

$$\frac{1}{2}\left(\frac{d\Phi}{dx}\right)^2 = \frac{en_p}{\epsilon_0} \cdot \frac{kT_e}{e} \cdot \left(\sqrt{1 + \frac{2e(V_p - \Phi)}{kT_e}} - 1\right) \tag{3.15}$$

The absolute value of the electrical field on the electrode surface with the potential V on it is determined for the high-voltage case by:

$$\left.\frac{d\Phi}{dx}\right|_{\Phi=V} = |E_{el}| = \sqrt{\frac{2en_p}{\epsilon_0}} \cdot \sqrt{\frac{kT_e}{e}} \cdot \left(\frac{2e(V_p - V)}{kT_e}\right)^{1/4} \tag{3.16}$$

The last expression [2] shows that, as a result of the reduced ion density across the sheath, the dependence of the electric field on the electrode surface grows as a root of the fourth order with the voltage, i.e. very slowly compared to the vacuum case. The sheath thickness in this case is equal to:

$$s = \frac{\sqrt{2}}{3} \cdot \lambda_{De}\left(\frac{2e(V_p - V)}{kT_e}\right)^{3/4} \tag{3.18}$$

that is larger than for the model with the constant ion density. The sheath thickness according to (3.18) is presented in Fig. 3.2 by the dashed lines for different voltages $(V_p - V)$.

Similarly (for example, in [34]) it is possible to derive a more general expression - the so-called Child-Langmuir law for the spatial charge limited instantaneous current j_i from the plasma. The current j_i is not necessarily equal to $j_0 = en_i \cdot V_i = en_s v_B$ (where n_s is the ion density on the boundary of the sheath and the quasineutral plasma) like it was for the previous case. The relation connects the ion current which is emitted by the plasma with the voltage $(V_p - V)$ on the sheath:

$$j_i = K_1 \cdot \epsilon_0 \cdot \sqrt{\frac{2e}{m_i}} \cdot \frac{(V_p - V)^{3/2}}{s^2} \tag{3.19}$$

where $K_1 = 4/9$ for the Child-Langmuir law.

In [76] Lieberman showed analytically that expression (3.19) in the RF case should be modified if it is applied for the time-averaged voltage between the plasma and the electrode. This is explained by the fact that periodical appearance of electrons in the sheath constitute a finite time-averaged electron density which ultimately results in another constant multiplier $\underline{K_1^*} = 200/243$ in (3.19). Respectively the sheath thickness s is a factor $(K_1^*/K_1)^{1/2} = \sqrt{50/27}$ larger compared to (3.18).

From the equations above we can draw some intermediate conclusions for the problems of high voltage on the ICRF antenna. The electrical field on the electrode surface for the

---

[2] Expression (3.16) was achieved when the ion-electron secondary emission is assumed to be negligible. If one accounts for the electron emission by ion bombardment and corresponding electron current $j_e = \gamma_{ie} j_i$ where γ_{ie} is coefficient of the ion-electron emission (the same as emission yield, see section 2.6.5), expression (3.16) for the surface electric field is modified by a multiplier:

$$\sqrt{1 - \gamma_{ie}\sqrt{m_e/m_i}} \tag{3.17}$$

In the "worst case" when γ_{ie} is about 10 and one considers hydrogen ions, the resulting change in the electric field will be below 13%. We can neglect the effect as the uncertainty connected with measurements of the plasma density n_p in the scrape-off-layer is higher (see section 5.3).

case of high plasma density (the plasma completely screens the external electric field) depends rather weakly on the applied voltage ($\sim V^{1/4}$). The space charge limited current for the high voltage sheath is also weakly dependent on the voltage (it is close to the Bohm current j_0). However the energy of the ions which carry the current increases accordingly to the voltage between the plasma and the electrodes. The strong dependence of the current and the electric field on the plasma density plays an important role in the conditions of the scrape-off layer plasma where the plasma density can be often changed by orders of magnitudes.

It is important to consider asymmetry of the electrodes of the gap. The electrodes can construct either a *symmetrical system* (electrodes are identical and have the same area) or an *asymmetrical system* (one of the electrodes is larger). For the last case one has a "large" electrode and a "small" electrodes characterized by the large and small areas correspondingly.

Furthermore we will rely on the following assumptions in the further discussion:

1. *the thin sheath, $s < d$*
   (a) quasineutrality of the plasma in all regions of the gap but sheaths;
   (b) the sheath is collisionless;
   (c) the sheath is a high voltage sheath and is "electron free": $eV_0 \gg kT_e$ leads to $\exp(e(\Phi - \Phi_p)/kT_e) \ll 1$ and the sheath boundary is sharp;
   (d) presence of the sheaths with the voltage drop on them $\sim kT_e/e$ means "electrical contact" between plasma and the electrode;
   (e) a change of the ion density in the sheath takes place in a time much longer than a change in electron density: electric field in the sheath changes instantly (without a delay) according to the changes of the external field;
2. *the thick sheath, $s > d$*
   (a) quasineutrality of the plasma in terms of the time-averaged densities $\bar{n}_e = \bar{n}_i$ in the whole gap;
   (b) the gap is collisionless;
   (c) voltage distribution over the electrode gap is close to the distribution in vacuum.

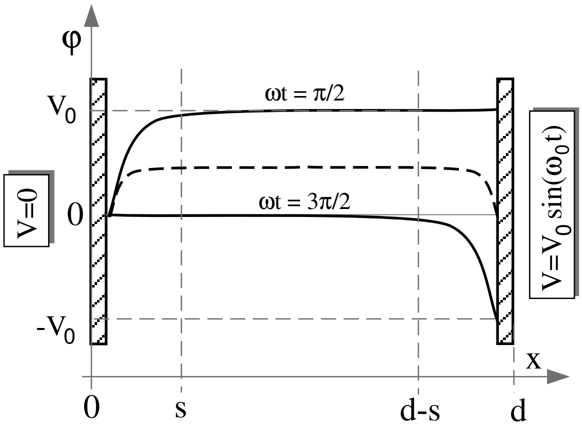

Figure 3.3: *Spatial variation of potential at maximal positive and negative voltage (solid lines) and time-averaged potential (dashed line) for symmetrical electrodes in a high density case.*

3.3.2 Basic dynamics of the thin high-voltage RF sheath ($s < d$)

Let us consider the basic dynamics of the potential distribution of the gap that consists of the sheath region and a region of quasineutral plasma charged to some potential V_p. The plasma potential has a relation to the amplitude of RF voltage on the electrodes. We discuss features of the symmetrical systems and systems with the electrodes of different area and the different conditions for the external DC circuit.

Symmetrical system of electrodes

The case of a thin sheath is illustrated in Fig. 3.3 for the symmetrical system. The left electrode is grounded, the right is RF driven: $V = V_0 \sin \omega_0$. The plasma inside the gap periodically moves towards one or the other electrode. In the case of two identical electrodes the quasineutral plasma (i.e. electrons) periodically contacts each of the electrodes.

At $\omega t = \pi/2$ the plasma reaches the right electrode in Fig. 3.3. The plasma is charged to V_0. The voltage is dropped at the ion sheath at the right electrode. No electron sheath can be formed since electron react to the external field instantaneously. At $\omega t = 3\pi/2$ the left electrode has a contact with plasma. This leads to the plasma potential close to 0 ($eV_0 \gg kT_e$). Thus the time-averaged potential is close to $V_0/2$.

Equality of the net DC current to zero

If the electrodes are identical, the net time-averaged (DC) current is zero and the current collected by one of the electrodes during a half of RF period, equals to the current collected by the other.

The condition of zero net DC current is also true when a blocking capacitor with high capacitance (the resistance of the capacitor is much lower than plasma resistance) is used in the circuit of RF electrode either in symmetrical or asymmetrical systems. In other words the case with the blocking capacitor means that the RF electrode is DC-floating. For the symmetrical system there exists no difference between the case of grounded or DC-floating RF electrode. For the asymmetrical case (see connections in Fig. 3.4a) the RF electrode can acquire a potential V_{dc}.

From the condition of zero net current we can derive the time averaged plasma potential $\bar{V}_p$ [68] assuming the potential of the plasma is:

$$V_p = \bar{V}_p + \Delta V_p \sin \omega_0 t \tag{3.20}$$

where ΔV_p is obviously a RF component of the plasma potential. The ion current density on the sheath boundary is the Bohm current $j_i = e n_p v_B / K_2$, where K_2 is a constant ($K_2 = n_p/n_s \approx \sqrt{\bar{e}})^3$, relating to a reduction of the ion density in the presheath [80]. In a collisionless sheath near a grounded electrode the Bohm current j_i is constant. The electron current near the ground electrode is determined with the Langmuir formula:

$$j_e = \frac{1}{4} \cdot e n_p \cdot \sqrt{\frac{2e\bar{V}_p}{m_e}} \cdot \exp\Big(-\frac{eV_p}{kT_e}\Big) \tag{3.21}$$

Equality of the time-averaged ion ($\int_0^{2\pi} j_i d(\omega_0 t)$) and electron ($\int_0^{2\pi} j_e d(\omega_0 t)$) currents leads to an expression for the plasma potential:

$$\bar{V}_p = |V_f| + \frac{kT_e}{e} \ln\left(I_0\Big(\frac{e\Delta V_p}{kT_e}\Big)\right) \tag{3.22}$$

where $|V_f| = -kT_e/2e \ln(\bar{e} m_i / 2\pi m_e)$ is the potential of the insulated probe (floating potential) and $I_0((e\Delta V_p)/kT_e)$ is the modified Bessel function of the first order.

For the high voltages ($(e\Delta V_p)/kT_e) \gg 1$) expression (3.22) is transformed to:

$$\bar{V}_p = \Delta V_p + |V_f| - \frac{kT_e}{2e} \ln\left(\frac{2\pi e \Delta V_p}{kT_e}\right) \tag{3.23}$$

If the same procedure is applied to the RF driven electrode with a voltage

$$V = V_{dc} + V_0 \sin \omega_0 t, \tag{3.24}$$

then by exchanging in (3.21) $V_p \rightarrow V_p - V$ and $\bar{V}_p \rightarrow |\bar{V}_p - V_{dc}|$, using (3.23), one can achieve the relation:

$$\bar{V}_p = \frac{V_0 + V_{dc}}{2} + |V_f| - \frac{kT_e}{4e}\left(\ln\Big(\frac{2\pi e \Delta V_p}{kT_e}\Big) + \ln\Big(\frac{2\pi e (V_0 - \Delta V_p)}{kT_e}\Big)\right) \tag{3.25}$$

Expression (3.25) (see also Fig. 3.3) confirms that for the symmetrical system the time-averaged plasma potential is close to $V_0/2$. It was noted in the beginning of this chapter

---

[3] We use $\bar{e}$ for the Euler number 2.7182... in order to differentiate it with the elementary charge e.

that for two equivalent electrodes with closed external circuit the plasma potential is positive due to the fact that a certain electron charge leaves the gap forever. Here we see that when a RF voltage is applied to the electrode, the plasma potential is charged more positively since the charge initially going to the electrodes increases. Application of the RF field leads to a higher plasma potential than (3.3). In this context we can speak about the so-called *sheath rectification* effect [77]: a time-averaged sheath voltage near every electrode is much higher than the voltage in (3.3). The high plasma potential leads to high ion DC currents towards the both electrodes. The sheath rectification is accompanied by a self-biasing potential V_{dc} in the asymmetrical system with the opened external DC circuit.

System with the RF driven electrode small and the external circuit opened

In Fig. 3.4a the small electrode is RF driven. Also for this system which includes a blocking capacitor, the ion current is compensated by the electron current for each electrode. This requires that the electron density should be in contact with the electrodes for some time during RF period.

At $\omega_0 t = \pi/2$ the plasma is charged to $V_{dc} + V_0$ when it reaches the small electrode. At $\omega_0 t = 3\pi/2$ the plasma reaches the large electrode and its potential becomes close to 0. Thus the time-averaged plasma potential should be indeed close to $(V_{dc} + V_0)/2$ (see expression (3.25)).

Self-bias of the RF electrode V_{dc} is negative if the RF driven electrode is smaller than the ground electrode. This can be shown from a simple electrical model which represents the sheath near left electrode as a capacitor C_1 of fixed value connected in parallel with a resistance R_1 of fixed value. The capacitor describes the RF displacement current flowing through the sheath while the resistance is a model for the response of the ion conductive current in the sheath to the RF voltage. For the right electrode we use C_2 and R_2 respectively. The capacitors are connected in series with the blocking capacitor C so that it does not limit RF current: $C \gg C_1$ and $C \gg C_2$. From the equality of RF current flowing through the left and the right electrodes:

$$\left(\omega_0 C_1 + \frac{1}{R_1}\right) V_1 = \left(\omega_0 C_2 + \frac{1}{R_2}\right) V_2 \tag{3.26}$$

where the RF components of the voltage drops near the electrode are respectively: $V_1 = \Delta V_p$ and $V_2 = V_0 - \Delta V_p$, one gets:

$$\Delta V_p = \frac{C_2 + 1/(\omega_0 R_2)}{C_1 + C_2 + (R_1 + R_2)/(\omega_0 R_1 R_2)} \cdot V_0 \tag{3.27}$$

Equation (3.27)[4] for the RF voltage drop V_2 at the grounded electrode can be also used for the voltage drop V_1 at the RF driven electrode by exchanging C_2 to C_1 and R_2 to R_1. The equation describes the voltage drops on the hybrid capacitive-resistive

---

[4] Equation (3.27) can be applied to any system as it is derived from equation (3.26) for the RF currents which is a general relation and is independent of the DC boundary condition and the electrode area.

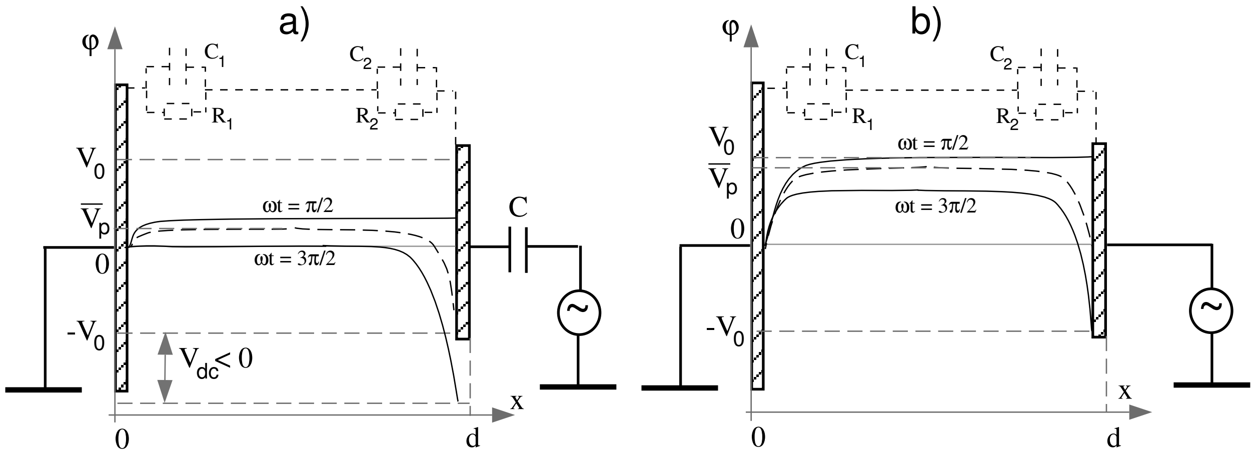

Figure 3.4: *Spatial variation of potential at maximal positive and negative voltage (solid lines) and time-averaged potential (dashed line) for the system with the small RF electrode: a) without blocking capacitor; b) with blocking capacitor.*

voltage divider that is the linear model for the sheath. It is important to note that in the limit $\omega_0 \ll \omega_{pi}$ the impedances of capacitances are very high so that capacitive current is much lower than resistive: $\omega_0 C_{1,2} \ll 1/R_{1,2}$ and the voltage divider becomes completely resistive. For $\omega_0 \gg \omega_{pi}$ respectively $\omega_0 C_{1,2} \gg 1/R_{1,2}$ and the voltage divider is completely capacitive.

For the system from Fig. 3.4a the minimal plasma potential is 0, the maximal is $2\bar{V}_p$, therefore $\bar{V}_p = \Delta V_p$. This system has also $\bar{V}_p \approx (V_{dc}+V_0)/2$. Hence one gets an expression for the self-bias V_{dc} of the right electrode:

$$V_{dc} = \frac{C_2 - C_1 + (R_1 - R_2)/(\omega_0 R_1 R_2)}{C_1 + C_2 + (R_1 + R_2)/(\omega_0 R_1 R_2)} \cdot V_0 \tag{3.28}$$

It is reasonable to consider that $C_1 > C_2$ since capacitance of a parallel plate capacitor is proportional to the surface area A and the left electrode area A_1 is larger than the area of the right one A_2. Also for the resistances: R_1 and R_2 are inversely proportional to the surface of a conductor. The role of the conductor here is played by the plasma and one has $R_1 < R_2$. Thus from equation (3.28) one concludes that V_{dc} is negative. One also sees that both types of the dividers: capacitive and resistive describe the rectification effect (existence of negative V_{dc}), hence for $\omega_0 \sim \omega_{pi}$ the rectification also occurs.

One can write for V_1 and V_2 and the system considered in Fig. 3.4a:

$$\begin{aligned} V_1 &= \Delta V_p = \bar{V}_p = \frac{V_0 + V_{dc}}{2} \\ V_2 &= V_0 - \Delta V_p = V_0 - \bar{V}_p = \frac{V_0 - V_{dc}}{2} \end{aligned}$$

As $V_{dc} < 0$ and $|V_{dc}| < V_0$ (see equation (3.28)), one gets the requirement that the RF component of voltage on the sheath near the large electrode $V_1 < V_0/2$ whereas near the small electrode $V_2 > V_0/2$. The time averaged plasma potential of the system $\bar{V}_p < V_0/2$.

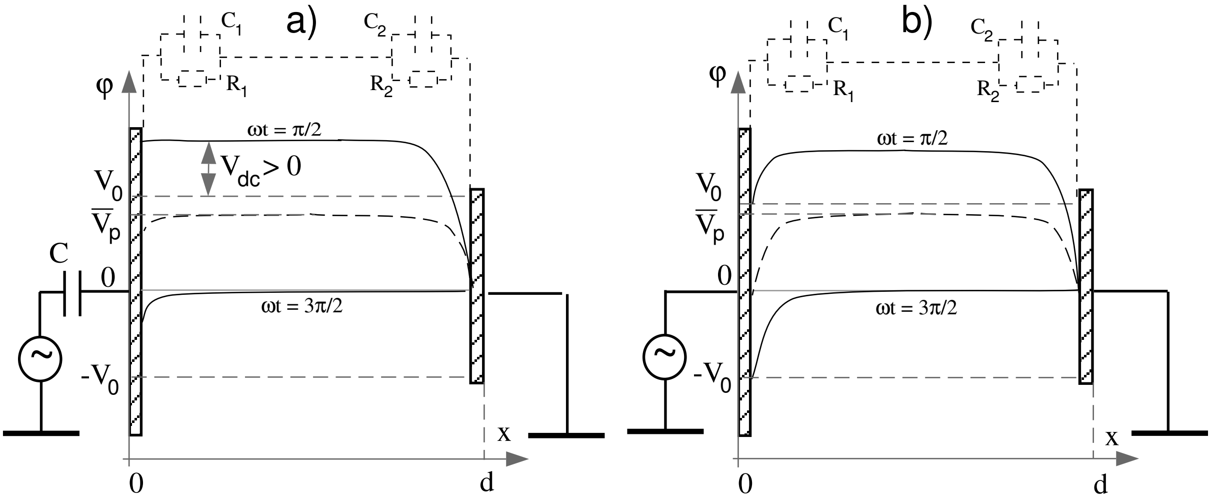

Figure 3.5: *Spatial variation of potential at maximal positive and negative voltage (solid lines) and time-averaged potential (dashed line) for the system with the large RF electrode: a) without blocking capacitor; b) with blocking capacitor.*

System with the RF driven electrode small and the external circuit closed

The ICRF antennas are usually DC grounded. The asymmetrical case for the small RF electrode is shown in Fig. 3.4b. An asymmetry in the electrode areas leads to the *battery effect* in the presence of plasma. Though the electrodes have the same DC potential, a DC current may be induced in the circuit. The mechanism of self-biasing does not work for the electrode but it applies to the plasma potential.

The plasma (electron density) should reach at least one of the electrodes, otherwise a continuous loss of the ions from the plasma would make the system non-stationary. Since electrodes can not acquire DC potential and the ion and electron currents do not compensate each other (DC current is present), the plasma can not reach both electrodes. The alternating component of sheath voltage is lower at the large electrode and the plasma does not touch the large electrode. An ion spatial charge is always present near the large electrode. This means that the plasma potential V_p is always higher than 0. If one accounts for the electron temperature this means that the minimal value of the plasma potential is higher than (3.3). The time averaged plasma potential $\bar{V}_p > V_0/2$. The effect can be considered as sheath rectification accompanied by self-biasing of plasma.

Systems with the RF driven electrode large

The asymmetrical systems shown in Fig. 3.5 can be treated in the same way. For these systems the RF electrode is the large electrode and the small electrode is grounded. For the case with the blocking capacitor (Fig. 3.5a) we achieve $V_{dc} > 0$. For the case of the closed external circuit (Fig. 3.5b) the plasma touches only the grounded electrode. For both cases the plasma potential V_p is 100% modulated and $\bar{V}_p > V_0/2$.

System description	voltage drop at RF electrode $V_D = (V_p - V)$	voltage drop at ground electrode V_p	modulation of plasma potential ΔV_p, $\Delta V_p/\bar{V}_p$
Blocking capacitor and small RF driven electrode (Fig. 3.4a)	$V_0 < V_D^{max} < 2V_0$ $V_0/2 < \bar{V}_D < V_0$	$V_0 > V_p^{max} > 0$ $V_0/2 > \bar{V}_p > 0$	$V_0/2 > \Delta V_p > 0$ $\frac{\Delta V_p}{\bar{V}_p} \approx 100\%$
Blocking capacitor and large RF driven electrode (Fig. 3.5a)	$V_0 > V_D^{max} > 0$ $V_0/2 > \bar{V}_D > 0$	$V_0 < V_p^{max} < 2V_0$ $V_0/2 < \bar{V}_p < V_0$	$V_0/2 < \Delta V_p < V_0$ $\frac{\Delta V_p}{\bar{V}_p} \approx 100\%$
No blocking capacitor and small RF driven electrode (Fig. 3.4b)	$V_0 < V_D^{max} < 2V_0$ $V_0/2 < \bar{V}_D < V_0$	$V_p^{max} \approx V_0$ $V_0/2 < \bar{V}_p < V_0$	$V_0/2 > \Delta V_p > 0$ $100\% > \frac{\Delta V_p}{\bar{V}_p} > 0\%$
No blocking capacitor and large RF driven electrode (Fig. 3.5b)	$V_D^{max} \approx V_0$ $V_0/2 < \bar{V}_D < V_0$	$V_0 < V_p^{max} < 2V_0$ $V_0/2 < \bar{V}_p < V_0$	$V_0/2 < \Delta V_p < V_0$ $\frac{\Delta V_p}{\bar{V}_p} \approx 100\%$

Table 3.1: *Maximal instantaneous and averaged voltages on the sheaths and plasma potentials for different DC boundary conditions and asymmetry. Left limit corresponds to the small asymmetry $A_1/A_2 \approx 1$, right limit corresponds to the large asymmetry $A_1/A_2 \gg 1$.*

Summary table

We can see that the high density plasma screens the externally applied electric field by forming a sheath near the electrodes as well as adds the plasma potential V_p to the voltage drops across the sheaths. The sheath voltages, and in particular their rectified components, depend strongly on the asymmetry of the system. The table 3.3.2 summarizes the rectified component and maximal values of the voltage drop across the sheath near the RF and ground electrodes. The left limit of the values in the table reflects the symmetrical case (Fig. 3.3) while the right one is the limit of the highest asymmetry or $A_1/A_2 \gg 1$.

The maximal values $V_D^{max} = (V_p - V)^{max}$ and V_p^{max} define the maximal values of electrical field on the surfaces of RF driven and grounded electrodes respectively. The maximal field ultimately influences the probability of arc ignition.

The rectified components $\bar{V}_D$ and $\bar{V}_p$ define the stationary ion fluxes on the surface of the electrodes. These fluxes can be essential for the sputtering on the antenna surface. For the case with a magnetic field, the rectified plasma potentials are also important for the electrical field distribution in the area of the antenna (see below section 3.4.2).

The modulation of the plasma potential are also described in the table 3.3.2.

The case with the blocking capacitor and small RF electrode for highly asymmetrical system is characterized by an almost double value of the maximal voltage drop on the RF electrode compared to the symmetric case and by a high DC self-bias of the RF electrode. The latter allows for surface processing of the RF electrode surface by bombardment of ions having energies close to eV_0. The small DC potential of the plasma (non-zero when accounting for electron temperature) results in low ion fluxes towards the grounded surfaces, that have large area and could be sources of undesirable impurities. These properties are used when building the systems for coating deposition and etching on the base of RF glow discharge or RF biasing of the electrode (substrate) in externally sustained plasma. The systems are widely used in science and industry. There exists practically no difference between the DC floating and dielectric substrate for heavy gases ($\omega_0 >> \omega_{pi}$). This enlarges the variety of the materials which can be used for substrate or coatings. In these systems the power is mainly consumed to sustain a discharge and to accelerate ions towards the RF electrode. Only a small fraction of the power goes for the acceleration of ions towards the grounded electrodes. The other 3 cases in the table are characterized by the formation of high DC ion fluxes towards the grounded electrodes.

The most interesting cases for ASDEX Upgrade antennas are the cases with the DC grounded electrodes. In the case of the small RF driven electrode, the RF voltage drop between the RF driven electrode and the plasma has the maximal value between V_0 and $2V_0$. The same situation is observed between the ground electrode and the plasma when the ground electrode is smaller than the RF driven one. The sign of the maximal RF voltage drop is the same for both cases and corresponds to the electric field direction from plasma to the electrodes, i.e. electron field emission and ion bombardment take place at that voltage. Due to the almost doubled potential drop for a strongly asymmetric system compared to a symmetrical system, fluxes of ions with energies twice higher than eV_0 may be collected by the electrodes when $\omega_0 \lesssim \omega_{pi}$. Consequently the system of electrodes should be as close to the symmetrical as possible to reduce the ion energies.

As we will see in 3.4, a magnetic field influences the effective geometry of the electrodes and requires a different approach for the electrode surfaces oriented differently with respect to the magnetic field.

One should also note that the modification [76] of the Child-Langmuir law for the time averaged ion current stated in section 3.3.1 is not applicable for all the systems. The modification used the model which assumes that a boundary of electron density reaches the electrode during RF period. The latter condition is not correct, in particular, for the case of the asymmetric systems without a blocking capacitor (see also Fig. 3.4b, 3.5b) where the electrons do not reach the large electrodes and the oscillations of the boundary of the electron density in the sheaths near the large electrodes are smaller, when the asymmetry is higher. Therefore the Child-Langmuir law modified in [76] should be used with care for the RF case.

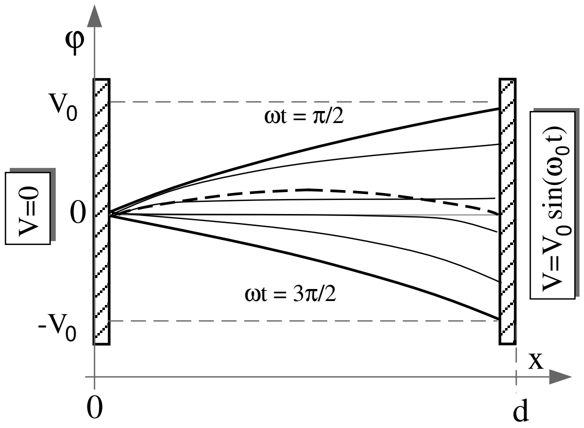

Figure 3.6: *Spatial variation of potential at positive and negative voltage (solid lines) and time-averaged potential (dashed line) for symmetrical electrodes in low plasma density case.*

3.3.3 Basic dynamics of the thick high-voltage RF sheath ($s > d$)

At high voltages and relatively low plasma densities, which are connected in terms of the sheath thickness s in Fig. 3.2, the sheath expands during RF cycle over the whole electrode gap (Fig. 3.6). This case is not a "classical" case and is not considered usually in the theory of RF sheath. As we have defined the case of the thick sheath, the sheath thickness is larger than the electrode gap for most part of RF cycle. This means that a high electric field is present at any point of the gap. Electrons leave the gap during a time shorter than half of a RF-period and are absorbed by the walls (electrodes). Ion density dominates over the whole electrode gap and produces a time-averaged electric field which extracts ions towards the electrodes as well. Thus ions tend to leave the gap in the electric fields of their own spatial charge. This together with the ion acceleration in the field results in a significant reduction of the ion density in the gap. The effect is larger for a larger electric field and finally the ion density is adjusted to fulfill the condition of quasineutrality, i.e. to be equal to the time-averaged electron density:

$$n_i = \bar{n}_e = \frac{1}{2\pi} \int_0^{2\pi} n_e \cdot d(\omega_0 t) \tag{3.29}$$

Let us consider a symmetric electrode system with a plasma sustained by injecting the charged particles into the gap. The injection is described by the charged particle generation rate $\xi(x) = \xi_i(x) = \xi_e(x)$, that is a number of particles generated in elementary volume at x per second. The instantaneous electron density across the gap (along x) can be presented as:

$$n_e = \int_0^x \frac{\xi dx'}{v_e(x')} \tag{3.30}$$

where $v_e(x')$ – instantaneous velocity of electrons at x'.

Plasma injection may be assumed homogeneous, i.e. $\xi = \xi_0$. The electron velocity v_e is derived from the energy conservation:

$$\frac{m_e v_{e0}^2}{2} + e\Phi(x) = \frac{m_e v_e^2}{2} + e\Phi(x^{'}), \tag{3.31}$$

where v_{e0} – an initial velocity of an electron, $\Phi(x)$ and $\Phi(x^{'})$ – potentials at positions x and $x^{'}$ respectively. However the initial velocity v_{e0} can be assumed to be the thermal velocity which is distributed symmetrically among the particles, hence it is zero for an "averaged" electron. Thus one gets:

$$v_e(x^{'}) = \sqrt{\frac{2e}{m_e}\Big(\Phi(x) - \Phi(x^{'})\Big)} \tag{3.32}$$

and:

$$n_e = \xi_0 \cdot \int_0^x \frac{dx^{'}}{\sqrt{\frac{2e}{m_e}(\Phi(x) - \Phi(x^{'}))}} \tag{3.33}$$

The distribution of the potential across the gap is close to the distribution without spatial charge when (2.21) is fulfilled. We assume that the potential is distributed in the gap as in the vacuum case:

$$\Phi(x) = V_0 \ \sin(\omega_0 t) \ \frac{x}{d} \tag{3.34}$$

Let us consider the electron density during the first half-period of the RF cycle: $n_e^{0\to\pi}(x)$. Because of the system symmetry, the density in the second half can be derived as:

$$n_e^{\pi\to 2\pi}(x) = n_e^{0\to\pi}(d - x) \tag{3.35}$$

By substituting (3.34) in (3.33) one gets:

$$n_e^{0\to\pi}(x) = \sqrt{2} \ \frac{\xi_0 \sqrt{d}}{\sqrt{(eV_0)/m_e}} \cdot \sqrt{\frac{x}{\sin(\omega_0 t)}} \tag{3.36}$$

To derive the time-averaged density one uses (3.36) for the first half-period and (3.35) for the second half-period:

$$\bar{n}_e = \frac{1}{\pi} \int_0^\pi n_e^{0\to\pi}(x) \ d(\omega_0 t) + \frac{1}{\pi} \int_0^\pi n_e^{0\to\pi}(d - x) \ d(\omega_0 t) \tag{3.37}$$

The integrated expression is:

$$\bar{n}_e = C_0 \ \frac{\xi_0 \sqrt{d}}{\sqrt{(eV_0)/m_e}} \cdot \Big(\sqrt{x} + \sqrt{d - x}\Big) \tag{3.38}$$

where C_0 is a constant:

$$C_0 = \frac{\sqrt{2}}{\pi} \int_0^\pi \frac{d(\omega_0 t)}{\sqrt{\sin(\omega_0 t)}} = \frac{\Gamma^2(\frac{1}{4})}{\pi\sqrt{\pi}} \tag{3.39}$$

From expression (3.38) one can see that the averaged electron density has a distribution with a maximum in the middle of the gap $x = d/2$:

$$\bar{n}_e^{max} = \sqrt{2}\, C_0 \, \frac{\xi_0 \, d}{\sqrt{(eV_0)/m_e}} \tag{3.40}$$

and it is inversely proportional to the square root of the amplitude value of the voltage V_0. The averaged electron density equals the ion density according to (3.29). Therefore one can speak of a reduction of plasma density by application of a high voltage in the case when the density is small enough, so the spatial charge effects do not change the distribution of the electrical field during most part of the RF cycle.

The described reduction of the plasma density may very well affect the neutral pressure balance in the region of the ICRF antenna. The neutral gas can be ionized by electron impact and be transferred to the electrodes thus reducing the neutral pressure near the antenna.

Rectified current

In the symmetric case the RF current is sinusoidal. If the areas of the electrodes are different, the currents are asymmetric. With the approximation (2.21) one can neglect the non-linear sheath motion [72, 76]. The current is transmitted mostly by electrons, as the current density at the two electrodes can be considered to be the same: the density is the same and defined by the plasma injection parameter ξ_0 and the electrode voltage. The current is higher for the half-period when the large electrode collects electrons. In a time-averaged picture a direct current flows externally from the large electrode to the small one if the external DC-circuit is closed. In the first approximation, assuming that all electrons injected with the external plasma immediately reach the electrodes, the current can be estimated as:

$$I_{DC} = \xi_0 \, d \, (A_1 - A_2) \tag{3.41}$$

where A_1 and A_2 – the surface area of the large and small electrodes respectively. This expression presents an actual saturation DC current which can be reached at high voltages for the case of the thick sheath.

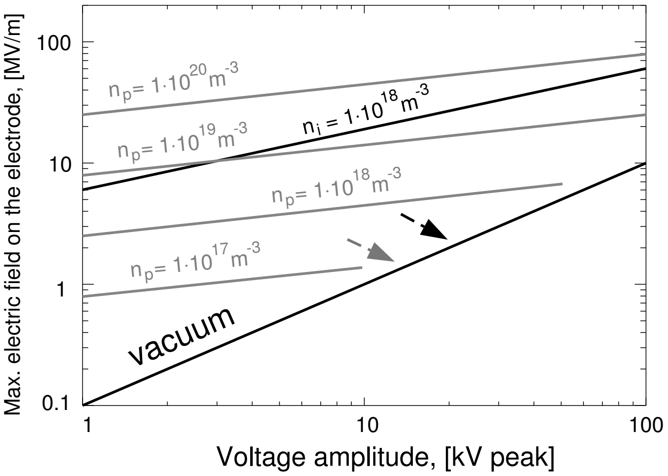

Figure 3.7: *Electrical field on the electrode surface versus voltage between electrode and plasma: solid black line - reference field in vacuum for the 1 cm gap, dashed black line - surface electrical field for n_i=const (3.13), gray lines - surface electrical field (3.16), T_e=15 eV, from the model which accounts for a reduction of n_i. The arrows show that for the thick sheath the electrical field approaches the vacuum field as the density in the gap is reduced.*

3.3.4 Surface electrical field and a transition to $s \sim d$

Fig. 3.7 presents the maximal value of the electric field on the electrode surface depending on the RF voltage between the plasma and the electrode. One can see that the electrical field in the presence of the dense plasma ($n_p \gtrsim 10^{17}$ m^{-3}) inside electrode gap is much higher than that in vacuum.

The model of n_i=const (dashed black line) is good for the presentation of the sheath dynamics, but overestimates the electrical field (equation 3.13). The model accounting the density reduction in the sheath (equation 3.16, gray lines) shows that an increase of the plasma density is more critical for the surface electric field ($E_{el} \sim \sqrt{n_p}$) than an increase in voltage ($E_{el} \sim v^{1/4}$). We will see in the experimental section 5.3.1 that plasma density in front of the ICRF antennas can be changed by orders of magnitude in the range still corresponding to $s < d$.

At $s > d$ the potential distribution is close to the vacuum case (solid black line). The intermediate regime, e.g. for the densities $n_p \approx 10^{16} - 10^{17}$ m^{-3} and voltages of 10-100 kV from the Fig. 3.2, is also characterized by a density reduction at very high voltages as for the case of low densities.

The effect of the density reduction in this range means that the density is too low to form the near-electrode sheath during the whole RF cycle while it is high enough for the spatial charge to change the field distribution from the vacuum one. The reduction of the plasma density leads to the faster asymptotic approach of the maximal electric field on the electrode to the vacuum field. This is presented in Fig. 3.7 by the arrows at the high voltages.

3.3.5 Role of ponderomotive force for density reduction

If electron moves in a non-homogeneous oscillating electric field, this motion is generally non-linear. The time-averaged electron displacement is not zero and electrons drift from a region of the strong electric field to a region of the small electric field as a non-linear force acts on them [78]:

$$F_{NL} = -\frac{\omega_{pe}^2}{\omega_0^2}\nabla\frac{\langle\epsilon_0 E^2\rangle}{2} \tag{3.42}$$

The force F_{NL} is called *ponderomotive force*. It leads to the drift of the plasma (ions follow electrons) from the regions of the strong electric fields[5].

The ponderomotive force is sometimes used to explain a reduction of the plasma density in the ICRF antenna box experimentally observed when the RF power is applied to the antenna [79].

It is important to note that the non-linear force (3.42) acts only if electrons move in RF electric fields for a time longer than RF period. If electrons are collected by the electrodes in a shorter time than RF period (as in the case of the thick high voltage sheath in section 3.3.3), electrons do not oscillate and the concept of the ponderomotive force is not applicable. The explanation of the density reduction for the thick sheath used in section 3.3.3 does not use the concept of the ponderomotive force.

In the case of the thin RF sheath (section 3.3.2), the sheath effects lead to localization of electric fields in the near-electrode regions. In a two-electrode system, the existence of electric fields near specific electrode leads to the appearance of electric fields near the second one. These electric fields can have RF and DC components which depend on the asymmetry of the electrodes. Furthermore the total electric fields near electrodes are directed always from the quasineutral plasma to the electrodes. Therefore electrons do not oscillate locally in these electric fields, though some of them can oscillate in the electrode gap, i.e. be confined by the electric fields of both electrodes. However the concept of the ponderomotive force is not applicable for this case.

For the system with two electrodes[6] it can be convenient to use the concept of the ponderomotive force at relatively small plasma densities when:

1. the capabilities of plasma to localize electric fields are small: $\omega_{pe} < \omega_0$ or $s \gtrsim d$ at $\omega_{pe} > \omega_0$ for a given RF voltage and interelectrode distance [7];

and

2. the interelectrode distance is large compared to the electron displacement due to the linear motion ($d > d_e$).

---

[5] The ponderomotive force applies similarly for electrons in RF fields of an electromagnetic wave. In our case we do not consider RF magnetic field and the Lorentz force associated with this field.

[6] Here we do not consider the cases when waves with strong RF electric fields can exist in the plasma.

[7] Use Fig. 3.2 for values of the density.

3.4 Influence of a magnetic field

The most important aspects of the influence of a magnetic field on the processes in the collisionless gap at a RF voltage are the following:

- a change of the effective collection areas of electrodes with respect to charged particle movement which is related to the confinement of charged particles as discussed in section 3.4.1;
- a large difference between the movement of electrons and ions in the RF electric fields with frequencies close or above the ion cyclotron frequency, the drift approximation can be applied only to electrons, see section 3.4.1;
- a change of plasma potential leads to consequences for the electric field distribution since the plasma is confined: a build-up of a complex 3D distribution of electric field is briefly discussed in section 3.4.2;
- at least two spatial dimensions should be used to treat electron trajectories in magnetic field for multipactor conditions: a discussion in section 3.4.3 is devoted to the features of the electron parallel and perpendicular movement in the external magnetic field and the influence on multipactor conditions.

3.4.1 Confinement of particles in the electrode gap

The particles in a magnetic field move along the magnetic field lines as in the case without the field. The transverse motion is circular for the particles with the constant perpendicular velocity $V_\perp$ and a constant magnetic field $\boldsymbol{B}$. The motion is characterized by a gyroradius – ρ_e for electrons and ρ_i for ions:

$$\rho_e = \frac{v_{e,\perp}}{\omega_{ce}}; \qquad \rho_i = \frac{v_{i,\perp}}{\omega_{ci}} \tag{3.43}$$

where ω_{ce}, ω_{ci} are the electron and ion cyclotron frequencies respectively.

In addition to the gyromotion, the particles (or the so-called guiding centers) drift in the direction perpendicular to magnetic field with velocities:

$$\boldsymbol{v}_{i,e,\perp} = \frac{\boldsymbol{E}\times\boldsymbol{B}}{B^2} + \frac{\boldsymbol{\nabla} p_{i,e}\times\boldsymbol{B}}{q_{i,e}\cdot nB^2} \tag{3.44}$$

where $\boldsymbol{E}$ - external electric field, $q_i = e$, $q_e = -e$. The first term is the so called *E-cross-B* drift which has the same direction for electrons and ions. The second term is a diamagnetic drift with the opposite sign for electron and ions and gives an averaged current connected with gyromotion and the drift of a single particle in the non-homogeneous magnetic field:

$$\boldsymbol{v}_{d\perp} = \frac{m_{i,e}v_\perp^2}{2q_{i,e}B^2}\cdot(\boldsymbol{B}\times\boldsymbol{\nabla} B) \tag{3.45}$$

The first order correction to the velocity in (3.45) can be derived by applying the operator $(\partial/\partial t + \boldsymbol{\nabla} \cdot \boldsymbol{V})$ to (3.45) as a zero-order expression and filling in the first term of it. As a result we obtain the polarization velocity:

$$\boldsymbol{v}_{i,e,pol} = \frac{m_{i,e}}{q_{i,e} B^2} \cdot \frac{\partial \boldsymbol{E}}{\partial t} \tag{3.46}$$

The particles are magnetized, hence the gyroradii are much smaller than the gap distance and electrode dimensions. This results in a change of the effective geometry of the electrodes, i.e. the surfaces should be accounted that are intersected by magnetic field lines. This makes the radius of curvature of the electrodes important. There exists no big difference in terms of particle fluxes compared to the case without magnetic field for the surfaces to which the magnetic field line have rather large angle of incidence α ($\alpha > 5°$).

Equations (3.44) and (3.45) are valid for the approximation $\omega_0 \ll \omega_c$. The magnetic moment:

$$\mu = \frac{\frac{1}{2}\, m_{i,e} v_\perp^2}{B} \tag{3.47}$$

is constant in this frequency range. The energy is distributed between $v_\perp$ and $v_\parallel$ depending on the initial conditions and B.

The heating of ions is possible by the RF electric fields at ion cyclotron range of frequencies. This means $\omega_0 \sim \omega_{ci}$ and $\mu \neq const$ which results in non-validity of the drift approximation for ions, though for electrons one still can use it.

The concept of the ponderomotive force described in section 3.3.5 can be applied for electron motion along the magnetic fields lines. For ions, a perpendicular non-linear motion can be also present.

3.4.2 Charging of the plasma in the magnetic field

The effects of the electrode asymmetry discussed in the previous section are of particular interest in the case of the external magnetic field.

In the Table 3.3.2 the geometry of the system changes the rectified potentials of the plasma and the modulation depth of the potential. In the magnetic field, the plasma is confined, so the plasma conductivity along the field lines is high. Thus the magnetic field lines may be assumed equipotential in the quasineutral regions. If a constant perpendicular electric field arises due to a charging of the plasma, the complex 3-D electrical field structure may be changed significantly. This may lead to additional $E \times B$ drifts and change of the particle convection and balance in the region of the electrodes. The problem of 3D convection is complicated for full analytical description, therefore these are combined with numerical calculations to investigate the interaction between the ICRF antennas and the plasma edge [81, 82, 83].

3.4.3 Multipactor conditions

Multipactor (see the sections 2.6.6, 2.7.3) represents a specific mechanism of electron confinement in the electrode gap. When an external magnetic field $\boldsymbol{B}$ is applied, the electrons are additionally confined. In a magnetic field oriented perpendicular to the electric field of the parallel plates, the single-surface multipactor can be initiated at low ratio ω_{ce}/ω_0 [84]. For ion cyclotron range of frequencies only two-surface multipactor resonance conditions may be fulfilled for the two parallel plate geometry when $\boldsymbol{B}$ is oriented with a large angle of incidence to the electrodes.

$\boldsymbol{E} \times \boldsymbol{B}$ drift multipactor?

The real geometry of the antenna and its surroundings allows for the existence of RF electric fields in various directions with respect to $\boldsymbol{B}$. The $\boldsymbol{E} \times \boldsymbol{B}$ velocity changes the sign according to the polarity of the electric field and in principle can play the role of the velocity parameter in the resonant conditions. This is only possible if the electrons are not lost during RF cycle along the magnetic field lines, i.e. the electric field along $\boldsymbol{B}$ is close to zero, because the ratio between the velocity along the magnetic field line and $\boldsymbol{E} \times \boldsymbol{B}$ is very high:

$$\frac{\boldsymbol{v}_{B\|}}{\boldsymbol{v}_{\boldsymbol{E}\times\boldsymbol{B}}} = \frac{\omega_{ce}}{\omega_0} \approx \frac{m_i}{m_e} \tag{3.48}$$

For the same reason $\boldsymbol{v}_{\boldsymbol{E}\times\boldsymbol{B}}$ requires relatively small gaps and high RF voltages to fit the resonant conditions. Compared to the multipactor along magnetic field lines which require $V_0 \sim 200$ V for $d \sim 1$ cm, fulfilling the resonance condition with $\boldsymbol{v}_{\boldsymbol{E}\times\boldsymbol{B}}$ would require $V = 800$ kV for $d \sim 1$ cm. Such voltages are irrelevant and therefore the resonance distance for the maximal voltages on the ICRF antennas is about 1/30 cm, much smaller than the typical antenna dimensions. Furthermore electron energies associated with the $\boldsymbol{E} \times \boldsymbol{B}$ movement are low with respect to the required (~ 200 eV for stainless steel) to get the secondary emission coefficient above unity. This makes the $\boldsymbol{E} \times \boldsymbol{B}$-multipacting improbable.

Multipactor along magnetic field

Nevertheless the multipactor along the magnetic field lines is probable and may have very distinguishable conditions compared to the multipactor without magnetic field:

1. Electrons move along magnetic field lines and are confined, i.e. the perpendicular diffusion of electrons is limited.

2. Magnetic field lines intersect the wall wich has a complicated 3D geometry. Consequently, it is likely that a system of two electrodes with a interelectrode distance close to the resonant can be formed.

3. Gyromotion of electrons changes the incident angle modifying the secondary emission yield which depends on $v_\perp$, $v_\|$ (the yield is typically increased since gyromotion increases $v_\|$).

The conditions listed make multipator possible at very unexpected regions of the vacuum vessel in the presence of magnetic field [85]. The multipactor effect is especially dangerous when a high gas desorption (electron stimulated desorption and desorption due to surface heating by RF current) leads to high neutral densities which can be ionized. We have discussed in chapter 2 (section 2.7.3) that the so-called "multipactor plasma" can be sustained at low pressures ($p \gtrsim 3 \cdot 10^{-2}$ Pa) [63].

3.4.4 Effect on the effective interelectrode distance

The Paschen law for ignition of RF glow gas discharge operates with the product of the neutral pressure and gap distance. An increase of the gap distance is equivalent to an increase in the pressure. The distance can be presented as $d^* = V^{gas}/S$ where V^{gas} – geometrical volume of the neutral gas, S – effective surface surface of the electrodes. When a magnetic field is applied, the surface may be significantly reduced. The effective surface of the electrodes in the magnetic field S_{mag} is the surface that is intersected by the magnetic field lines, connecting both electrodes, at large angles. Therefore the application of the magnetic field serves as an effective increase of the gas pressure by a factor of S/S_{mag}.

3.5 Summary

The electrostatic effects were considered for the description of the plasma - RF antenna interaction. For a plasma density corresponding to $\omega_{pe} > \omega_0$, the external electrical field can be screened by the ion space charge in the case without magnetic field or in the case with large angles of incidence of magnetic field to the surface of the electrodes.

If the sheath associated with the spatial charge near the electrodes is thinner than the electrode gap, the surface electrical field is amplified. The field depends on the the voltage $(V - V_p)$ between the quasineutral plasma and the electrode as $(V - V_p)^{1/4}$ and on the plasma density n_p as $\sqrt{n_p}$. This makes variations of the plasma density essential for the surface electric field. The ion current from the plasma to the electrode is space-charge limited and energies of the ions which contribute to the current are defined by the DC voltage drop between the plasma and the electrodes in the case $\omega_0 \gg \omega_{pi}$ or by the RF potential drop if $\omega_0 \lesssim \omega_{pi}$. The RF and DC voltages between the plasma and the electrode in a system with different electrode areas can reach $2V_0$, where V_0 is the amplitude of the RF voltage between the electrodes. For a system of electrodes with equivalent areas, the corresponding DC potential is about only $V_0/2$ while the maximal RF potential drop plasma-electrode $(V - V_p) \sim V_0$. This makes the consideration of the antenna electrode asymmetry important in order to reduce the voltage drops near the antenna electrodes and to reduce the energy of ions which bombard the surface of the electrodes. The presence of the external magnetic field should also be taken into account as it influences the effective area which collects charged particles.

If the sheath is thick compared with the interelectrode distance, the applications of a high RF voltage to the electrodes reduces the plasma density in the gap. For the intermediate case, when sheath thickness is of the order of the gap distance, the plasma density is also reduced. In addition the neutral pressure balance is affected, since the neutral gas can be ionized and transferred to the electrodes.

The magnetic field has additional consequences for the RF breakdown: multipactor and RF glow gas discharges by simplifying the ignition of both. Geometrical considerations are important to prevent the discharge ignition: avoiding the distances between two conducting surfaces along the magnetic field lines which fit the resonant conditions for the multipactor (in practice this can be only partly realized by using simple geometry with well-defined interelectrode distances); minimizing the effective electrode distance $d^* = V^{gas}/S$, where V^{gas} – geometrical volume of the neutral gas, S – surface limited by the intersection of the electrodes by magnetic field lines.

Chapter 4

Experimental approach

The ICRF antennas in a fusion device with magnetic confinement are situated in the scrape-off layer region. For ASDEX Upgrade the antennas are placed at the low field side. Many mechanisms of charged particle transport from the core plasma to the outer wall (see also chapter 1) exist in a tokamak. The particle transport affects properties of the SOL plasma. The presence of the intermittent plasma fluxes towards the wall due to the appearance of instabilities at the plasma edge, for example edge-localized modes (ELMs), is an inherent property of the fusion experiments. Similar plasma conditions can not be reproduced in a test facility.

The ICRF antennas operate under these conditions, but can not provide an explicit knowledge on the high voltage breakdown for several reasons:

1. The antenna has a complex 3D-geometry with various alignments of the electrodes with respect to the magnetic field. This makes it difficult to analyze experimental data on the local phenomena and predict the critical aspects of the antenna in terms of the RF breakdown.

2. The whole range of the RF voltages from zero to the maximal one (the latter being defined by the RF power coupled to the antenna) is present on the antenna components which face the SOL plasma.

3. The antenna is a tool for the plasma heating and is usually not diagnosed specifically to get a detailed knowledge on the RF breakdown.

4. The plasma heating by the ICRF antennas affects the tokamak central plasmas as well as the edge plasmas. This makes the problem strongly non-linear and very difficult to treat (as we already noted in the beginning of chapter 2 we apply a "first order" approach in the frameworks of this thesis trying to avoid the global plasma changes).

One comes to a logical conclusion that a specialized experimental device is required to model the antenna and to study the breakdown phenomena. The experiment should have a simple geometry, a defined voltage facing the SOL plasma, should be well-diagnosed

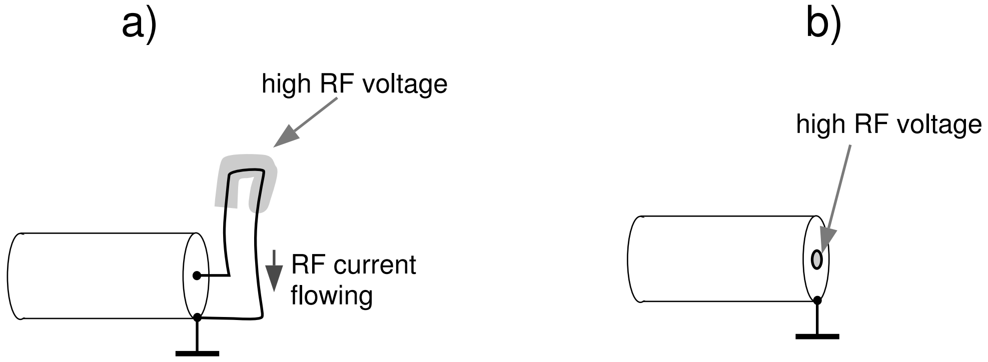

Figure 4.1: *Experimental modeling of the ICRF antenna high voltage region: a) inductive loop of the ICRF antenna, b) model: coaxial open end of a RF probe.*

and should not lead to the global plasma changes as occur during operation of the ICRF antennas.

This chapter is devoted to the description of an experimental device - an active ICRF probe which has been developed as a part of this thesis in order to gain data on the local effects taking place during the interaction of a high RF voltage with the SOL plasma.

4.1 Concept of the experiment

The ICRF antenna contains an inductive loop (a strap, Fig. 4.1a) and has a voltage distribution along the loop. The ICRF probe is the open end (Fig. 4.1b) of a resonant coaxial line to model the antenna high voltage region. The probe has a well-defined value of the RF voltage exposed to the plasma boundary.

In Fig. 4.2 a detailed concept of the experiment is shown. The experiment is built on the basis of a resonator. The matching of the system is realized by a change in frequency and a variable short (a stub tuner). The choice of materials for the RF conductors affects the Q-factor of the system. The initial requirements for the materials were defined from the requirements for the Q-factor and similarity with the AUG ICRF antennas:

1. achievement of high RF voltage ($\approx$60 kV) at moderate input RF power ($P < 500$ kW) that requires $Q >$150;
2. minimization the mismatch due to the load changes caused by changes of plasma, requires Q as low as possible;
3. ICRF antennas on ASDEX Upgrade have stainless steel electrodes.

Stainless steel electrodes were chosen. If ones uses equations (2.5), (2.6) from chapter 2 with $\sigma = 1.67 \cdot 10^6$ (Ω^{-1} m^{-1}) and geometrical parameters for the coaxial system of the probe which will be noted below in section 4.2 of this chapter, one gets $Q_{no\ load} = 261$. This value agrees reasonably with the experimental $Q = 230$ and shows that losses are mostly defined by the finite (and relatively low) electrical conductivity of stainless steel.

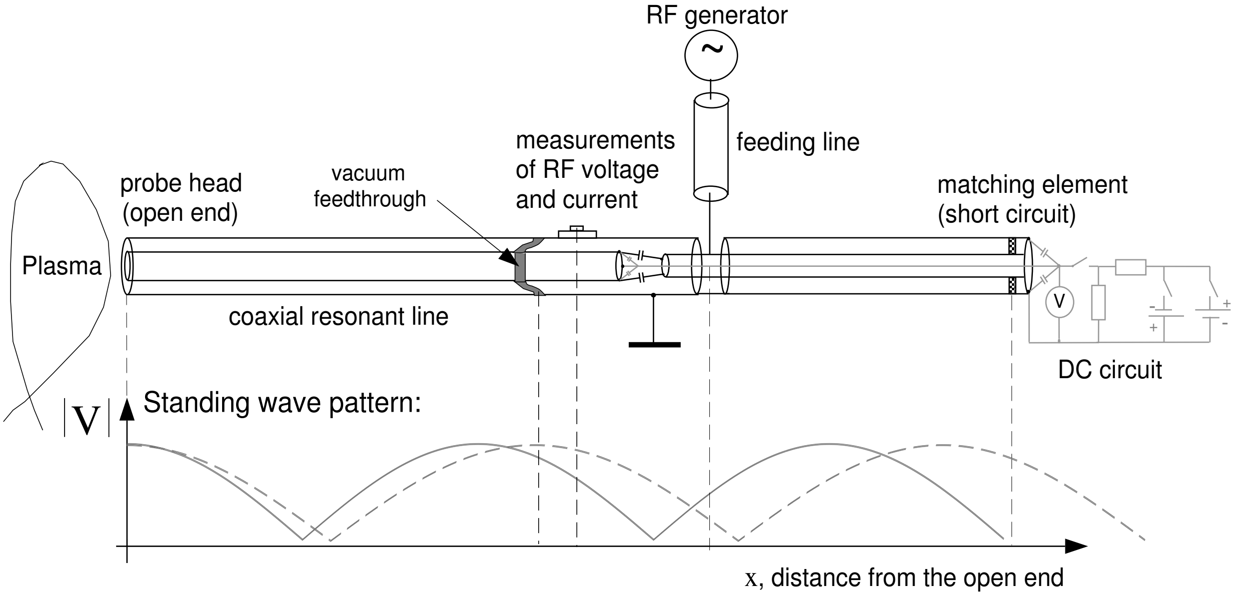

Figure 4.2: *Concept of the ICRF probe experiment. Two standing wave patterns correspond to two resonant frequencies for the resonator, the solid line corresponds to the frequency used for the matching.*

The matching of the resonant system uses the following scheme: by adjusting the frequency, the input impedance at the point of the connection of the feeding line is fitted to an impedance equal to $Z_0 + iY$, where Z_0 is the characteristic impedance of the feeding line, Y is the imaginary part of the impedance which is compensated by the stub tuner reactive impedance $Y_{stub} = -Y$ at the same location. Therefore the input impedance of the whole resonator equals to Z_0 which corresponds to the matching. The matching position can be changed only between RF pulses, therefore for a single RF pulse one is limited to one matching position.

In Fig. 4.2 two standing waveforms are shown. Both correspond to the matching of the resonator. Two frequencies can be used for the $\approx 5\lambda/4$ resonator with a difference of about 2 MHz. The highest frequency of 51.52 MHz (solid gray line) is chosen to have a lower RF voltage at the position of vacuum feedthrough (see also the next section for the description of the setup).

Because of the sheath effects described in chapter 3, it is important:

- to measure the DC (rectified) voltage appearing on the inner conductor or DC current flowing through the inner conductor;

- to have the possibility to apply a DC potential using an external power source.

Therefore the inner conductor facing the plasma is DC-disconnected from the rest of the resonant line by an inner DC break (a capacitor for the inner conductor). The stub tuner with the short circuit allows a cable connection from the inner conductor at the plasma side to an external DC circuit.

Measurements of the RF voltage and current are available $\lesssim \lambda/2$ from the open end. The directional couplers in the feeding line measure the forward power from the generator and the reflected power. A more detailed description is found in section 4.4.1.

Thus the concept for the RF probe working in the ion cyclotron range of frequencies allows for:

- measurements of the RF voltage, current and the phase between them;
- measurements of the rectified current (voltage);
- affecting the rectified current (voltage) by the DC boundary condition.

At first we describe the power generators used in the experiments. The experimental device of the ICRF probe is subsequently discussed in more detail.

4.1.1 RF and DC power generators

RF generator

One of the AUG RF generators was used both for experiments the RF probe in a test facility and in AUG with. The generator consists of four amplifier stages and is capable to deliver 2 MW of power for a pulse duration of 10 s.

A scheme of the generator with details of the final amplifying stage is shown in Fig. 4.3. The three stage pre-amplifying circuit is not shown in details. The final stage consists of the input matching circuit and a high power tetrode tube connected to a tunable grid circuit. RF power is coupled from the tetrode tube to a resonator. A variable short allows to adjust the resonator for a particular frequency. Power from the resonator is coupled to the output via a circuit which includes three coaxial lines with different characteristic impedances and adjustable lengths for the given frequency, so the output impedance equals the impedance of the transmission line (50 Ω).

The generator works in the frequency range 30-120 MHz and has a bandwidth of 200 kHz. A change of the frequency by a value larger than the bandwidth requires readjustment of the generator resonators and can be done automatically within a few minutes. The output power of the generator can be modulated with an arbitrary waveform. The modulation can be made with a response time of about 1 ms.

DC power supply

Four DC power supplies *KEPCO BOP 100-4M* [87] were used for experiments where the inner conductor was set at a certain DC bias. The supplies can work in pair in master/slave modes. One power supply generates 100 V DC voltage with a maximal current of 4 A.

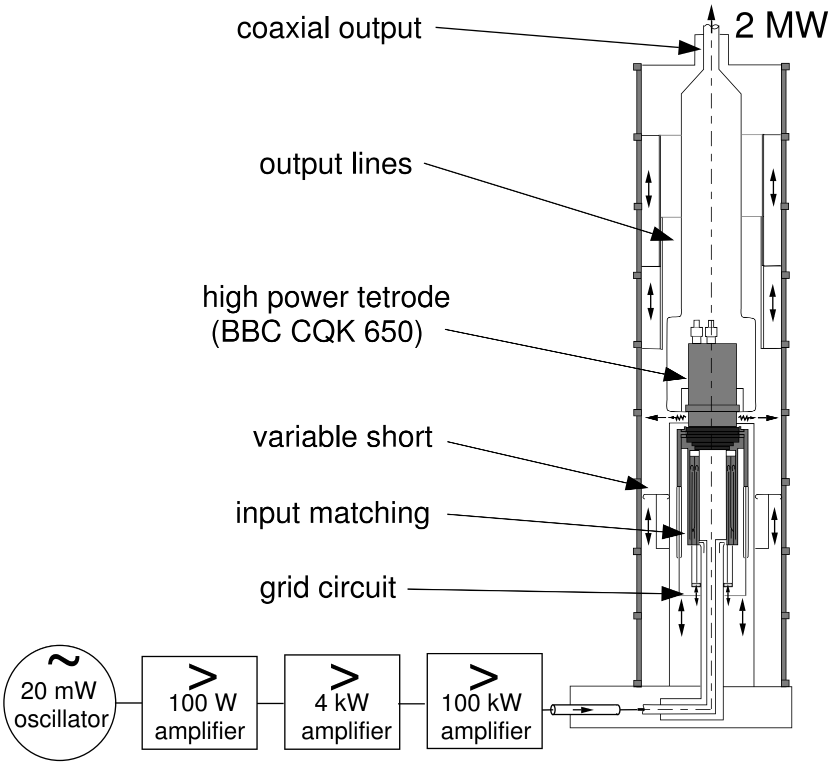

Figure 4.3: *Scheme of AUG ICRF generator.*

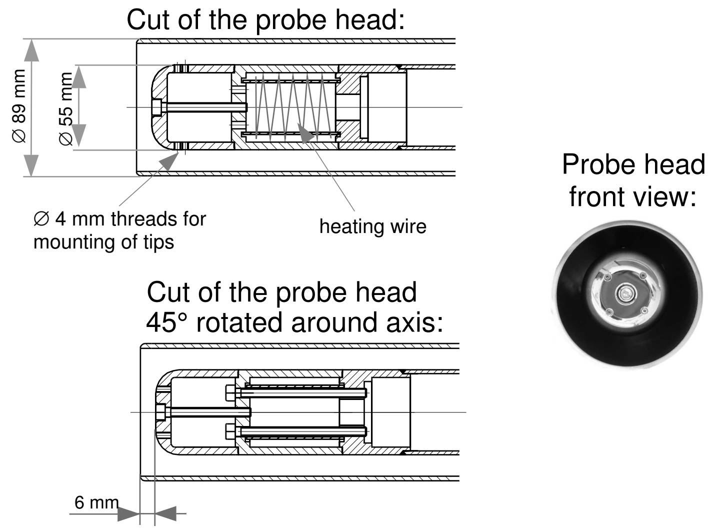

Figure 4.4: *ICRF probe head in details.*

4.2 Experimental device

The experimental device can be divided into five main parts:
1) probe head;
2) vacuum coaxial line;
3) DC cabling in RF resonator;
4) matching circuit;
5) feeding circuit.

We discuss each in the following sections.

1) Probe head

The drawing of the probe head is shown in Fig. 4.4. The probe head consists of a coaxial inner and outer conductor. The outer conductor is a 3 mm thick stainless steel tube with outer diameter of 89 mm. The inner conductor has a diameter of 55 mm. The corresponding characteristic impedance is 25 Ohm.

The inner conductor consists of an exchangeable head close to the plasma, the intermediate piece (stainless steel) with a heating wire for outgassing, and the long inner conductor (stainless steel tube) of the resonant part of the line.

The head was manufactured from stainless steel and was mechanically polished to the microroughness parameter $R_z < 0.5$ (see [86] for a detailed description). The head design allows for the installation of tips of different shape with a height of 4 mm for a local increase of electric field on the electrode surface. The tips were prepared in the same way as the head [86] and can be mounted with the help of a thread in 4 mm diameter holes in the head. The four holes are distributed evenly around the probe head (i.e. 90^o between each hole). The holes can be adjusted with respect to a direction of an external magnetic

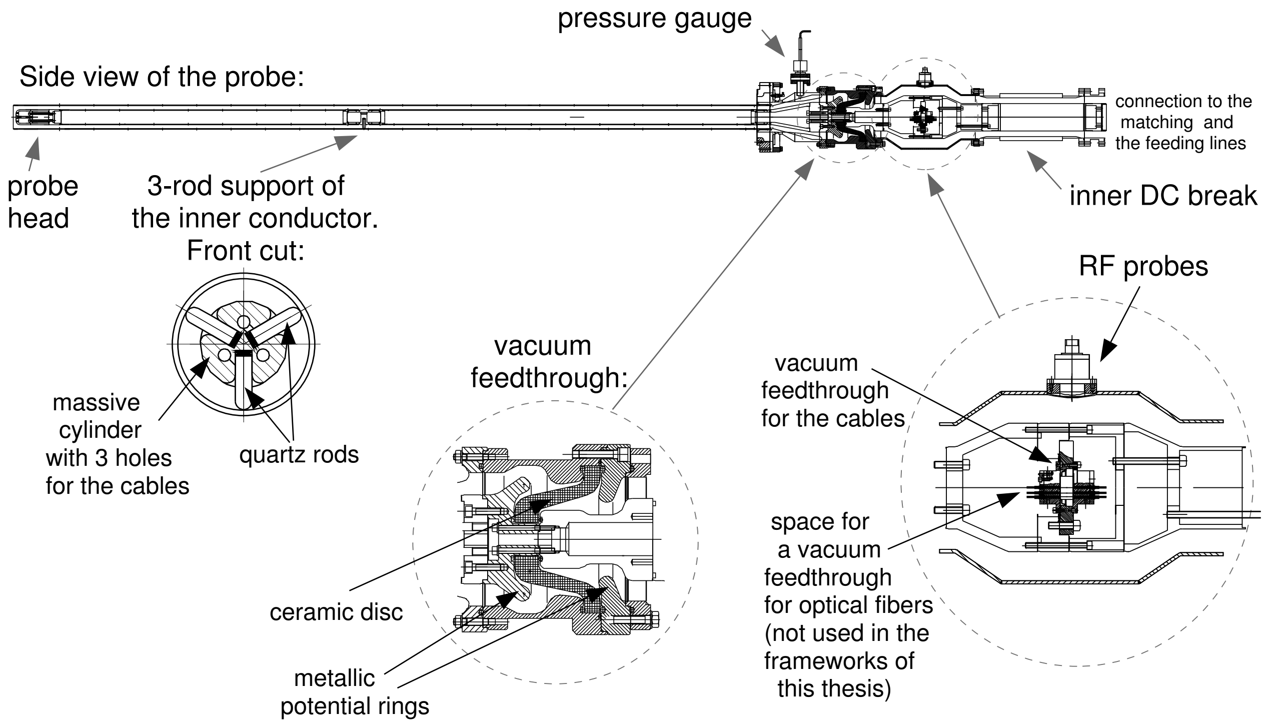

Figure 4.5: *ICRF probe vacuum and pressurized lines.*

field. The tips were not installed for the experiments in a magnetic field performed in the frameworks of this thesis.

2) Vacuum coaxial line

The vacuum part of the resonant line is illustrated in Fig. 4.5. The inner conductor has a length of ≈2.7 m from the head to the vacuum feedthrough. Because of this rather long length, the inner conductor is supported by a support of a special design. The support consists of a massive cylinder with a thread in it on both sides to connect two stainless steel tubes constituting the inner conductor, and three quartz glass rods. Quartz glass has a dielectric constant of $\varepsilon \approx 1.5$ which is one of the closest value to unity from commercially available dielectric materials. The low dielectric constant is required to have a high voltage stand-off (tested to be more than 35 kV) and minimal changes of characteristic impedance of the coaxial line. The massive cylinder has three holes between the quartz rod positions for the passage of the cables inside the inner conductor (Fig. 4.5).

A Penning pressure gauge is used to measure the pressure near the vacuum feedthrough. The vacuum feedthrough includes two parts. The first part is a ceramic disc for vacuum isolation between the inner and outer conductor of the coaxial line. The second part is placed inside the inner conductor and isolates the connections of the cables.

Stainless steel parts forming the system of the electrodes were finished by electrochemical polishing.

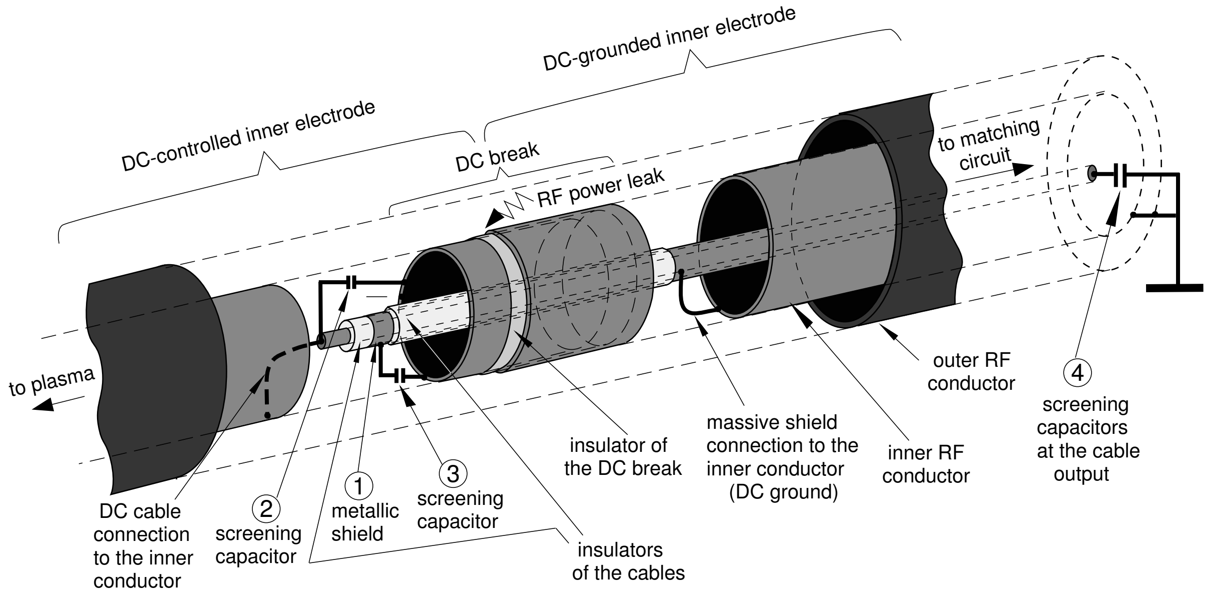

Figure 4.6: *Screening of the cable placed in the RF inner conductor to close the circuit for the RF power leak to the inner space of the DC break of the inner conductor.*

3) DC cabling in RF resonator

The voltage strength of the DC-break and the cables inside the inner conductor should be high (at least > 5 kV) to withstand the DC voltages. In addition there exists the problem that RF power can be coupled to the inner conductor of the main coaxial line through the inner DC break (Fig. 4.6).

The estimation of the RF power can be done as follows. We know that electrical field in a capacitor is proportional to a voltage on the capacitor electrodes. In our case the voltage across the capacitor is a voltage drop on the DC-break defined by the current flowing on the outer surface of the inner conductor and RF impedance of the capacitor $1/\omega_0 C_{DC-break}$, where $C_{DC-break}$=5 nF is the DC-break capacitance. The capacitance is relatively low for the frequency used and the RF voltage drop across the DC-break can be rather high. Furthermore due to geometrical restrictions and mechanical design the DC-break is located in the vicinity of the maximum of the RF current. The current maximum is estimated to be about 2.4 kA for 60 kV voltage maximum in the main probe line. The corresponding voltage drop on the DC-break is ≈ 1.5 kV. The voltage across the DC-break can be considered as the local voltage on the parasitic transmission line formed by the inner surface of the inner conductor and an electrical cable inside it. If the power reflected back from the parasitic line is assumed to be small and characteristic impedance of the cables is $\approx 50\ \Omega$, the resulting coupled power is somewhat higher than 20 kW (this is the upper limit estimation).

Even at a coupled power of a few kW, existence of a resonant condition inside the uncertain configuration of the electrodes in the inner conductor can lead to very high voltages and damage of the cables. Therefore the proper RF screening of the cable is very important.

The scheme of the screening is illustrated in Fig. 4.6. Several screening techniques were used (see the corresponding numbers in the figure):

1. the cable is screened by a metallic shield with a massive electrical connection to the DC grounded part of the inner electrode;
2. a RF filtering capacitor is mounted between the DC cable and the DC-controlled inner electrode at the boundary between shielded and unshielded cable;
3. a RF filtering high-voltage capacitor is mounted between the shield and the DC-controlled inner electrode at the boundary between shielded and unshielded cable;
4. RF filtering high-voltage capacitors are mounted at the output of the cable from the matching resonator line (a scheme of the short circuit is shown in Fig. 4.6).

In reality two DC cables are used in the inner space of the inner conductor which allow simultaneously to control the DC boundary condition and to heat the inner conductor head. One cable is connected directly to the DC-controlled side of the inner conductor, the other is connected to the same electrode through the heating spiral shown in Fig. 4.4. With this scheme the inner conductor can be heated by an AC 50 Hz current from an insulation transformer. At the same time one can control DC conditions or perform DC measurements with the help of the cable directly connected to the inner conductor. For the scheme of two cables the shield (number (1) in Fig. 4.6) was used for both cables (twisted pair) and two additional screening capacitors were mounted: one connecting the both wires of the cables at the boundary between shielded and unshielded cables and one connecting the second wire to the DC-controlled inner electrode.

When the RF power leak was not suppressed by the screening, arcing between the DC cables and the shield occurred as well as arcing between the shield and the inner side of the inner conductor was observed: the cables and the inner electrode were damaged. The arcing inside the DC cables occurred in the regions of the cable bending. After the described screening techniques were used, arcs did not appear and the cables were not damaged during the long term experiments. Also RF power was screened well at the input/output of the resonator matching circuit (RF amplitude was much less than 1 V on the end of DC cables disconnected from the external power supplies) and therefore RF power did not penetrate into the external DC power supplies which can be also damaged if the power level is high.

4) Matching circuit

A 9-inch line segment with a massive variable short is used as a matching element (see Fig. 4.7). The 9-inch line was used instead of a 6-inch line in order to increase the reliability of operation of the pressurized lines under high voltages. The matching concept allows for an output of the cables from the inner space of the inner conductor. The cables, after being RF filtered at this output, are connected to the DC measurement (control) lines (see section 4.4.2) and to the AC insulation transformer for heating respectively.

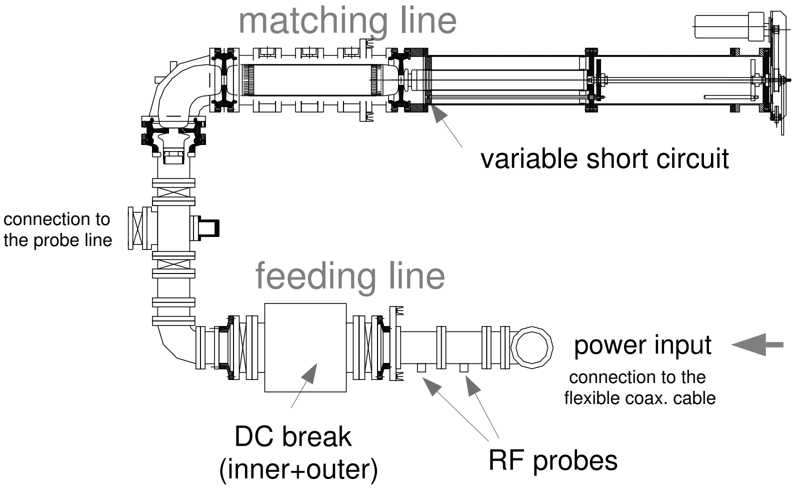

Figure 4.7: *Matching and feeding circuit of the probe.*

5) Feeding line

The feeding line is a line with 50 Ω characteristic impedance. The line is equipped with a DC-break for inner and outer coaxial conductors to avoid a ground loop between the grounds of RF generator and toroidal chamber. The RF pick-up probes mounted on the line allow for measurements of forward and reflected power. A 3-inch flexible high power cable of about 6 m long was used to allow some radial movement of the probe by midplane manipulator motor drives. A 6-inch transmission line to RF generator with iron inner conductors was used to maximize attenuation between the probe and the generator. The attenuation is used to minimize influence of the fast changes of the load of the probe on the generator.

4.3 Setup of the experiment

To use the described experimental device on ASDEX Upgrade, we first need to calibrate and test systems. For this reason the components of the device and then the completed device were mounted in a test facility without magnetic. This installation allowed not only to test the RF system and measurements, but also to gain an initial knowledge on the processes described in chapters 2, 3 that may be responsible for the power limitation on the ICRF antennas.

After the operation in the test facility the device was installed in ASDEX Upgrade where studies of the voltage stand-off in the real conditions of the SOL plasma were conducted.

Let us first describe the features of the installations of the ICRF probe in the test facility and subsequently in ASDEX Upgrade.

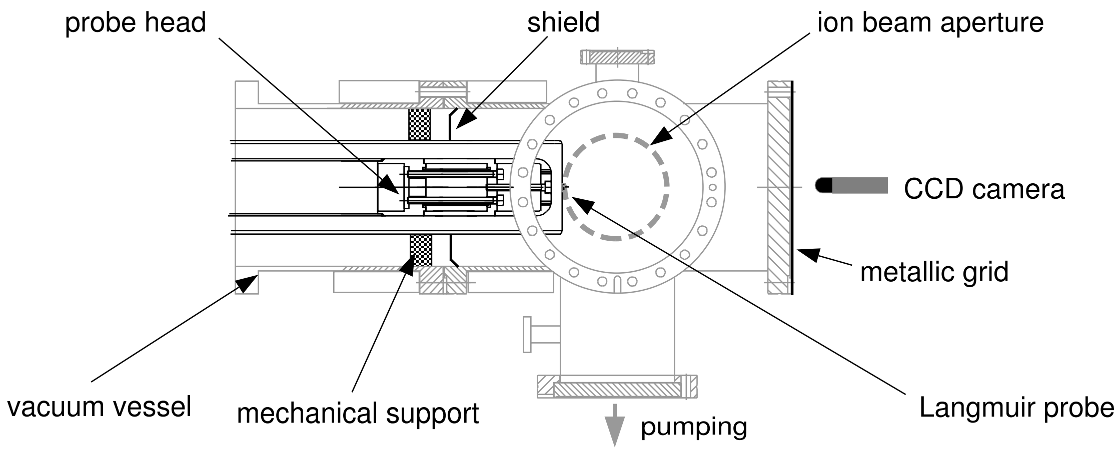

Figure 4.8: *Experimental setup in the test facility.*

4.3.1 Setup in the test facility

Calibration of the RF probes

The RF pick-up probes were calibrated using special lines. In the case of the RF probes mounted $\lesssim \lambda/2$ from the open end the same parts of the main coaxial lines were mounted separately and terminated by 50 Ω resistance as a load. The transmission measurements were conducted by a *Hewlett-Packard 8753D* [88] network analyzer in the frequency range 30-60 Mhz. The corrections were made for the line with the standing wave ratio k=2 (characteristic impedance of the probe lines used for calibration is 25 Ω). The coupling factors for the pick-up RF probes for the forward and the reflected power in the feeding lines were measured in a similar setup without the corrections for k since the characteristic impedance of the feeding lines equals 50 Ω and $k = 1$.

ICRF probe installation

The probe can be mounted in the test facility field (see Fig. 4.8). A 6-inch tube is used as a vacuum vessel. The outer conductor of the probe was supported by a support made of an insulator. The parasitic coaxial line between the outer conductor of the probe and the vacuum vessel (the tube) was screened from RF power by a shielding ring (shield in the figure). A vessel with multiple ports was installed for pumping, for the installation of a plasma source and for optical observation of the ICRF probe head. The port with a glass window in front of the probe head was screened by a metallic grid.

A Hall-type ion source was used as a plasma source. Ions in the source are accelerated by the anode layer of the axisymmetric discharge in crossed electric and magnetic fields [89]. The discharge exists in the circular electrode gap with 10 cm diameter and 4 mm thickness. The ion source produces a tubular beam with a total current of 5-300 mA, average current density 0.3-20 mA/cm^2, ion density 10^{14}-10^{16} m^{-3} and average ion energy 200-2000 eV. The tubular ion beam is injected perpendicular to the open end of coaxial line. The mode of operation allows to have the ion energy distribution function close to a maxwellian with the maximum at about 30% of the accelerating voltage.

The plasma density was measured near the ICRF probe head by a Langmuir probe collecting beam ions. The density was estimated from the ion saturation current using the ion velocity corresponding to the maximum energy of the initially known ion energy distribution function.

In addition a CCD camera was installed with a time resolution of 20 ms for observation of the ICRF probe head (see Fig. 4.8).

Data acquisition

A *Nicolet 460* oscilloscope system [90] measured the amplitudes of the RF signals with a time resolution of several tens of milliseconds using well-calibrated linear RF detectors. Fast *Acqiris DC 265* 8-bit digitizers [91] with a bandwidth of 150 MHz and a sampling rate of 500 Msamples/s allow to save the RF signals digitally. The RF amplitudes and the phase were obtained by fitting the waveform with sinusoidal functions of time.

When a RF breakdown leads to ignition of an arc, the arcing generates a noise with a broad spectrum of frequencies. A high fraction of the energy is carried by low frequency modes which often lead to saturation of the saved signals. To prevent the saturation, the RF signals passed through analog high-pass filters of the first order with a resonance frequency of 1 MHz.

4.3.2 Setup in ASDEX Upgrade

ICRF probe installation

The ICRF probe was designed to be mounted on AUG midplane manipulator (Fig. 4.9). The manipulators can also be used to mount Langmuir probes (see section 5.3.1).

The matching and the feeding lines (Fig. 4.7) are mounted vertically on a special movable supporting construction so they can provide a radial movement of 130 mm when the lines are connected. The radial position can be varied from 10 mm beyond the position of the ICRF antenna limiter (into plasma) to 120 mm behind the limiter (in the limiter shadow). The most used position coincided with the one of the ICRF antenna strap that is ∼35 mm in the antenna limiter shadow.

Signals transfer and data acquisition system on ASDEX Upgrade

Signals from the RF pick-up probes were transferred by coaxial cables from the ASDEX Upgrade experimental hall to a control room. In order to separate the RF cables in the hall and in the control room galvanically, DC-breaks were used. For the measurements of DC potential (or current) voltage-frequency converters were used to transfer the signals over the light fibers to the control room. The optical signals were converted back to electrical signals by frequency-voltage converters. The fiber optic-based lines have a bandwidth of 128 kHz.

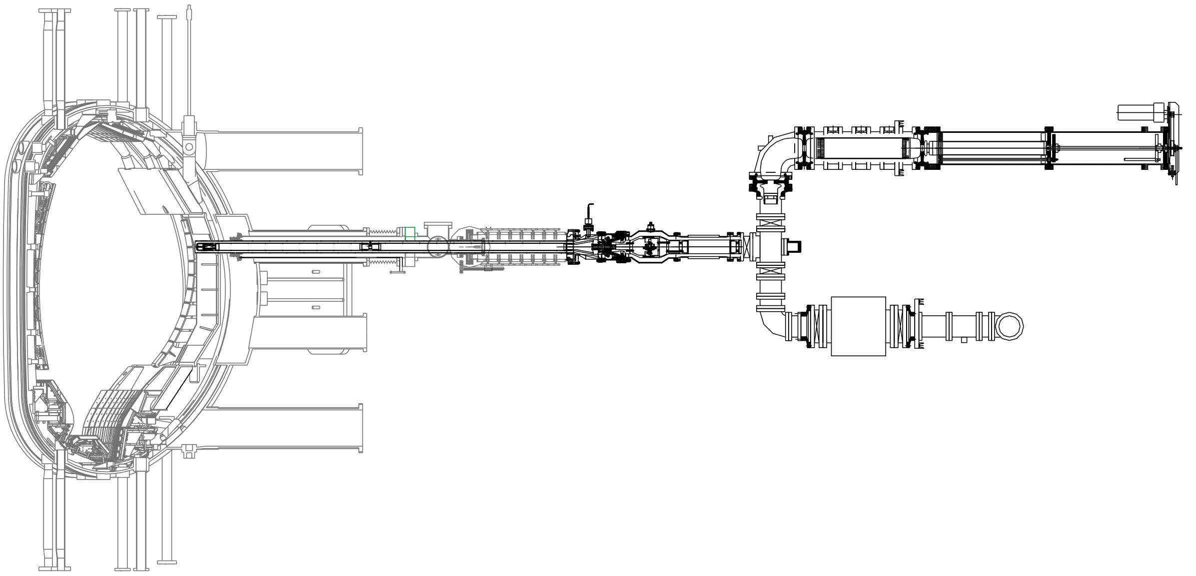

Figure 4.9: *Experimental setup in ASDEX Upgrade.*

The data acquisition system was saving the data of the RF detected signals and DC voltage/current and was integrated into the shotfile system of ASDEX Upgrade, except for the *Acqiris* system which was equipped with the high-pass filters and saved the last 2 to 4 ms of the RF voltage, current and power before a breakdown. The breakdown was detected by setting the critical reflected power level as the trigger for the data acquisition.

4.4 Measurements

To get an information on the processes occurring at the probe head a few options for the measurements are available. Measurements by RF probes and the DC circuit are the most important to characterize RF breakdown phenomena.

4.4.1 RF measurements

Because of geometrical constraints set by the construction of the midplane manipulator the RF voltage and current are measured only a distance of $\lesssim \lambda/2$ from the probe head. The location of the measurements is few tens of cm closer to the open end than the voltage maximum corresponding to $\approx \lambda/2$. This allows to measure RF current of a relatively high amplitude: one has no problem of a small signal.

However the values of the voltage and the current at the probe head should be reconstructed from these measurements. The reconstruction is done by calculating the standing wave pattern with a constant load impedance at the head. The load impedance for the ICRF probe in vacuum is modeled as: a resistive part R_r and a stray capacitance C_{stray} connected in parallel. If $R_r \gg Z_0$, where $Z_0 = 25\ \Omega$ is the characteristic impedance, the voltage standing wave pattern has the same form for any value of the input power and voltage at the probe head:

$$V_{rf}^{head} = A \cdot V_{rf}^{meas} \tag{4.1}$$

where V_{rf}^{meas} is the measured value of the RF voltage and $A = 1.359$ is a reconstruction coefficient. From the distant measurements of RF voltage and current it is possible to deduce the information on the load impedance of the open end. However when using the amplitudes of the RF signals, one needs to deal with a few problems. Values of RF voltage depend strongly on the matching position, hence one needs to account for the mismatch. Very fast processes resulting in fast load changes have a small influence on the RF voltage because a high reactive power is stored in the high-Q RF circuit.

The RF voltage on the open end is controlled by a waveform of the input power. Thus the resonator can be represented as a wide-band amplifier. For the wide-band amplifier transient characteristics are often described in terms of a rise-time t_{rise}, the time it takes the envelope of modulation to increase from 10% to 90% of its final value [92]. The rise time can be estimated from:

$$t_{rise} \approx \frac{0.7}{B_{3dB}} \tag{4.2}$$

where B_{3dB} is bandwidth of the amplifier [92] which can be expressed in terms of RF frequency f_0 and Q-value:

$$B_{3dB} = \frac{f_0}{Q} \tag{4.3}$$

Assuming a constant Q-factor, for the parameters noted above $t_{rise} \approx 3$ μs. This time resolution is not enough to resolve a vacuum arc.

The output power of the RF generator may be strongly affected if the reflected power on the generator side exceeds the critical level (2.7). For this reason the RF voltage often becomes an unreliable physical magnitude. A good option for a reliable measurement of the load impedance is to use the phase value between voltage and current at the point of measurement. For an electrotechnical model with a constant stray capacitance one can obtain a relation between the phase and the load resistance.

If we assume the stray capacitance to be $C_{stray} = 5$ pF, the voltage and the phase depend on the open end resistance according to Fig. 4.10. One can see that the phase has a low sensitivity to a change of the load resistance and the evolution of the load can not be detected by the phase measurements if the load changes too little. However we are interested in the effects connected to the change of the load resistance by orders of magnitude (transition to RF glow discharge, RF sustained arcing) and the phase measurements are applicable.

The method of time-resolved voltage and current measurements has been used in more simple systems to measure the power coupled to a discharge, see e.g. [93]. In our case it is convenient to use Q measurements to estimate the power coupled to the load.

To measure the power coupled to the plasma P_{coup} by the ICRF probe for load changes happening slower than the time (4.2), one can apply measurements of Q-factor and use the earlier measured Q without a load. This requires the assumption that the power going to the intrinsic losses in the conductors is the same for the same voltage for the cases with

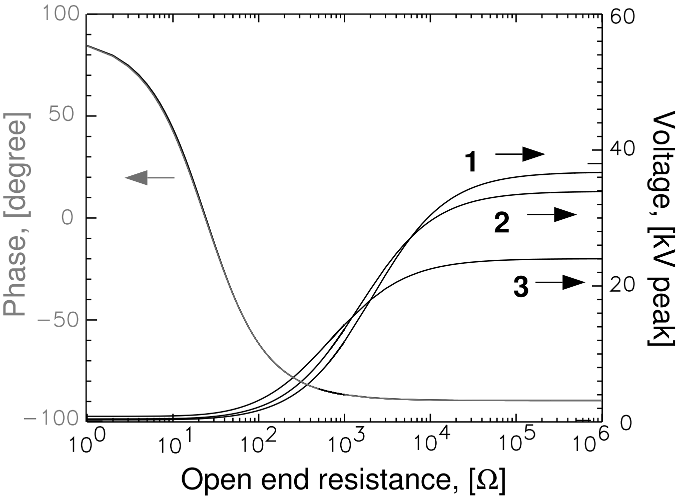

Figure 4.10: *Sensitivity at the point of measurements for 300 kW net power. Voltage curves: 1 - matched for 1 MΩ, 2 - matched for 5 kΩ, 3 -matched for 1 kΩ.*

the load connected and disconnected. A formula can be derived:

$$\frac{P_{coup}}{P_{net}} = 1 - \frac{Q}{Q_{no\ load}} \tag{4.4}$$

where Q is the Q-factor measured with the load, $Q_{no\ load}$ is measured without the load (in vacuum). This simple equation may be applied to the ICRF antenna as well. One can see here that the ideal case $P_{coup} = P_{net}$ (where P_{net} is the net RF power) corresponds to the case $Q_{no\ load} \to \infty$, since $Q \geq 1$. Equation (4.4) may be written in terms of energy conservation:

$$P_{net} = P_{coup} + P_{loss}\ , \qquad P_{loss} = P_{net}\ \frac{Q}{Q_{no\ load}} \tag{4.5}$$

meaning that the net RF power goes partly to the load and partly to the losses.

4.4.2 DC measurements

The DC external circuit may be changed as shown in Fig. 4.2: open DC circuit (inner conductor is DC floating), a low resistance can be connected (closed DC circuit) or a DC bias can be applied. The first configuration allows to measure the rectified voltage, the second - to measure precisely the rectified current, the third - to affect the current by connecting an external power supply with a certain polarity.

Most of the experiments in the test facility in the presence of plasma were performed with the inner conductor DC-floating. This configuration in the test facility allows one to have the measurement of the rectified current from the charging characteristics of the DC-break capacitor if the plasma conditions can be assumed constant.

Rectification effects were discussed in chapter 3. The rectified self-bias voltage can reach the value of the order of RF amplitude in the DC-floating configuration for the inner conductor when the plasma density is high. For the ASDEX Upgrade the high self-biasing voltage on the inner conductor is possible during the high density transient phases (e.g. ELMs). Technically it is not allowed to have voltages above 5 kV on the inner conductor. For this reason, the majority of experiments with the ICRF probe in ASDEX Upgrade were carried out with the resistance $R_{dc} = 10\ \Omega$ (see Fig. 4.2) connected setting the DC boundary condition to the DC short circuit. This configuration is very similar to that of the ASDEX Upgrade ICRF antennas.

The DC biasing experiments were conducted by connecting the DC power supplies (described in section 4.1.1) in series with a balast resistance $R_{bal} = 50 - 100\ \Omega$. The resistance R_{bal} was used to limit the DC current when an arc appears in the probe and transforms a high resistance load to a short circuit.

Chapter 5

Results and discussion

In the following chapter the experimental results both from the test facility and from ASDEX Upgrade are presented. The studies were performed in three steps:

1. experiments in the test facility;
2. experiments with a Langmuir and the ICRF probes on the midplane manipulator of ASDEX Upgrade;
3. studies of the high voltage operation of the AUG ICRF antenna and comparison with the ICRF probe.

5.1 Test facility results

The preliminary experiments in the test facility were conducted in order to find the main candidate processes causing the high-voltage breakdown on the ICRF probe as the model of the ICRF antenna. The vacuum arc and the glow discharges are studied in particular. Also the overall tests of the system were performed.

5.1.1 Operation at high voltage in vacuum

The vacuum arc is one of the mechanisms to limit the voltage, especially for a bad conditioned ICRF antenna. Arcing becomes less probable when a high voltage conditioning is applied according to section 2.5.2.

The ICRF probe was installed in the test facility and conditioned in vacuum ($p < 10^{-4}$ Pa) by high power pulses to reliable operation with 60 kV, 200 ms or 80 kV, 20 ms pulses. During the conditioning, vacuum arcs appear mainly at the probe head and are registered by the CCD camera.

The probe head for the most experiments in test facility was equipped with cone-like tips on the inner conductor which increase local electrical field approximately by a factor of 7.5 (the radius of curvature of the top of the tips is 0.5 mm). When the tips were mounted, the majority of the arcs in vacuum appeared in their vicinity (not only on the top). However the same values of voltages as for the probe without the tips were achieved by intense high-voltage conditioning in vacuum.

Since the energy is mostly dissipated in the system as intrinsic RF losses, the matching position changes during the pulse due to heating of the resonator components (section 2.6.3). RF pulses of 200 ms duration at a voltage of 50 kV are already critical for the system matching. Using the formula (B.6) in Appendix B, one can estimate the temperature increase of the conductors. The estimation results in about 50 ^{o}C for a current of 2 kA with a duration of 200 ms on a conductor with 3 mm thickness. The temperature coefficient of the resistance of the stainless steel is about $5 \cdot 10^{-3}$ $(^o\mathrm{C})^{-1}$. The surface resistance R_{sq} at 50 ^{o}C is 25% higher than the resistance at the room temperature. According to the theory briefly reviewed in section 2.2 the change of the phase along the transmission line due to the losses is assumed to be zero. If one assumes that the observed mismatch happens only because of the changed resistance of the stainless steel components and makes an estimation in terms of the above mentioned theory, the corresponding change in the absolute value of the input reflection coefficient $|\rho_{feed}|$ is $8 \cdot 10^{-4}$. This is too small to explain the experimentally observed increase of the reflected power of about 10-20% of the forward power at the feeding point that is proportional to $|\rho_{feed}|^2$. Thus the change of the reflected power is connected either to a change of the phase characteristics of the stainless steel lines between the open end and the feeding point or to a change of characteristics of the matching circuit. The change of the geometry (e.g. lengths) due to the heating of the electrodes can affect both. A further estimation of these effects is not considered in the frameworks of this thesis.

To minimize the reflected power level, the ICRF probe was operated in the test facility mostly with short pulses, while for the long pulses in the test facility and in ASDEX Upgrade the matching was chosen to minimize the reflected power level at the time when a RF breakdown was anticipated.

The other aspect of high voltage in the resonator with stainless steel electrodes, is a high gas desorption which leads to even higher importance of the pulse length during the conditioning and operation.

5.1.2 Vacuum arc ignition

For the well-conditioned electrodes, ignition of a vacuum arc is difficult during 20 ms pulse even at the 80 kV voltage. However the conditioning looses its effect after a period of a few hours. This results usually in a vacuum arc appearing at voltages $\approx$ 10 kV lower than the maximum voltage obtained right after the high-voltage conditioning. The conditioning effect may also be reduced for an operation after ignition of the arc. However a long term high-voltage conditioning in vacuum with the arcing sustained for less than 2 μs eventually results in an improved voltage stand-off.

In Fig. 5.1 the transients of forward and reflected power, voltage and phase are presented for a vacuum arc. One can see that a change of the phase starts about 300 ns before the vacuum arc develops. After the spark stage of the arc, the phase becomes close to 0^0 and then oscillates. According to the model from section 4.4.1 zero phase corresponds to the load impedance approximately equal to the characteristic impedance. The spark stage

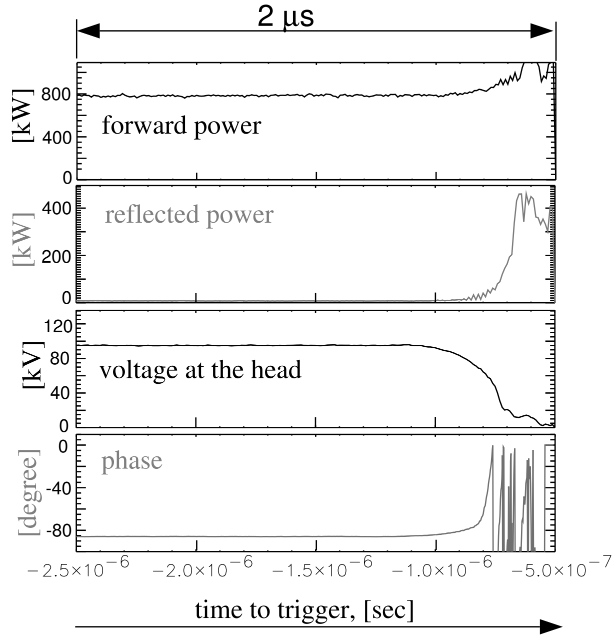

Figure 5.1: *Arcing phenomena in vacuum.*

follows the initial phase change and is finished when the arc is developed. The duration of the spark stage of a few hundred nanoseconds agrees with the expectations from the discussion in section 2.5.3.

In addition to the phase jump of about 90^0, the increase of the reflected power and an increased light emission observed by the CCD camera confirm the vacuum arc ignition at the probe head. It is also observed that the RF voltage degrades very fast during the arc development. For a constant Q-factor the time required for the voltage to change should be about 3 μs (see section 4.4.1). The observation of a faster change of voltage contradicts to the assumption Q=const and therefore indicates a fast decrease of Q. This means that the vacuum arc after the spark stage dissipates the energy very efficiently.

As was discussed in section 2.4.2, the evolution of the arc discharge is dependent on the Q-factor. For Fig. 5.1 the switch-off of the RF power by the generator corresponds to the time -0.5 μs. The increase of the reflected power and the decrease of the voltage before the switch-off is a demonstration of the self-adjusting mechanism of RF arc. It should be also noted that the RF voltage shown in Fig. 5.1 after the arc ignition may be overestimated since it includes the contribution from the arc produced noises in the broad frequency range. The plotted voltage is the amplitude of the sinusoidal fit to the data collected with the help of the fast data acquisition system (described in section 4.3.1).

For the whole series of experiments with vacuum arc (which also included variation of the critical power level for the RF generator switch-off), the damage of the electrodes was observed only as single points. Thus the vacuum arc for the ICRF probe is self-suppressed by a mismatch which follows the transformation of high resistance load to the short circuit.

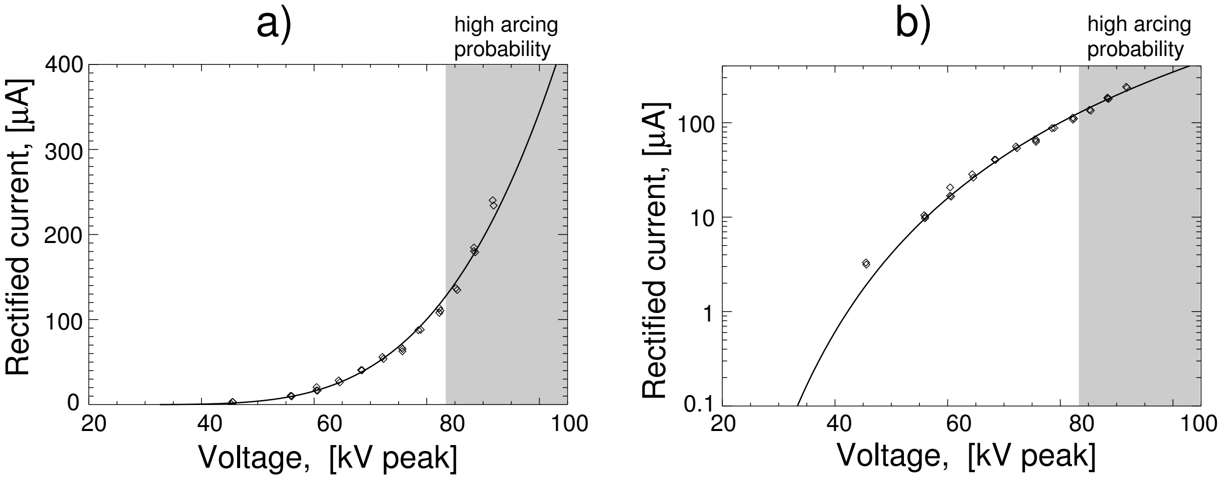

Figure 5.2: *Rectified field emission current:a) linear graph, b) logarithmic graph. Diamonds - measured current, solid curve - fit to the formula (2.14) by varying* A_{RF} *and* β_{RF}.

5.1.3 Definition of DC current direction

When the effects of self-biasing are discussed, it is convenient to use the following definition of DC currents. The current which charges the inner electrode to a positive self-bias (when the external DC circuit is opened) is defined as a *positive* rectified current. The current corresponding to a negative self-biasing is defined as a *negative* current.

We should note that though the DC circuit is often opened, the high value of the blocking capacitor (DC-break) (see chapter 4) allows for an evaluation of the DC currents from linear part of the charging voltage-time characteristic of the capacitor.

5.1.4 Field emission and dark currents

At a voltage higher than 40 kV, field emission dark currents in vacuum can charge the inner conductor to a positive self-bias when the external DC circuit is opened. The reason for the positive biasing lies in the asymmetry of the coaxial system. From the Fowler-Nordheim formula (2.14) one can easily show that the electron current emitted by the inner conductor in RF half-period is larger than the one by the outer conductor. The reason for that lies in the difference of the emissive area.

From [44] one knows that the RF field emission shows a more stable behavior of the emitted current than the DC field emission. The mounted cone-shaped tips with the amplification factor 7.5 on the probe head (sections 4.2 and 5.1.1) increase the emission currents which makes them easier to detect. A stable positive DC self-bias on the inner conductor was detected when the probe was conditioned to the high voltages. The rectified current deduced from the measured charging voltage-time characteristic of the blocking capacitor (DC-break) is shown in Fig. 5.2 by diamonds. The error on the measurements of the current is about 2 μA (and is due to the RF noise coupled to the measurement circuit).

The dependence on the voltage shows clear exponential behavior peculiar to the field emission (see Fig. 5.2a). The measured current is actually a time-averaged difference between the current emitted by the inner electrode and the current emitted by the outer. For the field amplification of 7.5 for the inner electrode one can neglect the contribution to the current by the outer electrode because of the exponential part dependence of the current on the electrical field in equation (2.14).

A standard fit [44] by the two parameters: the emitting area A_{RF} and the local amplification factor β_{RF} (see section 2.5.1) can be successfully applied to the experimental data when the amplification $\beta_0 \cdot \beta_{RF} = 7.5 \cdot \beta_{RF}$ is accounted for the inner electrode. A Poisson-weighted least-squares fit results in $A_{RF} = 1.99 \cdot 10^{-16}$ m^2, β_{RF}=334 and the corresponding solid curves in Fig. 5.2a,b.

For the voltages above 80 kV many RF pulses longer than 10 ms are terminated by arcing at the probe head. Before the data presented in Fig. 5.2 was taken the probe and the tips have been conditioned to have the arcing probability low enough for making about 10 consequent arc-free RF short (3 ms) pulses possible.

In section 2.6.2 of chapter 2 the focusing of the ions on the microprotrusions was discussed. The focused ion flux may in principle influence the emission characteristics of the protrusions and the rectified current. To look for this effect an externally sustained ion density (plasma) presence is required.

5.1.5 Influence of plasma at low neutral pressure

The operation with the Hall ion source (see section 4.3.1) allows for having relatively high plasma densities at relatively low neutral pressures. This means that a plasma density can be controlled externally when no glow discharge is ignited in the gap.

According to chapter 3, a rectified current should flow through the electrodes if a plasma is present in the electrode gap. If one takes into account that the area of the RF driven electrode of the probe (inner conductor) is smaller than the area of the grounded electrodes (outer conductor and the chamber wall) in the test facility, the current should correspond to a negative self-biasing of the inner electrode if the external DC-circuit is opened and therefore the charging current is negative (according to the definition in section 5.1.3). At the same time at high voltages one has a positive bias from the field emission current which can compensate the biasing connected to the plasma presence.

In Fig. 5.3 the measured rectified field emission current after the long term operation is shown by squares. The current was measured at a pressure of 0.1 Pa of helium gas was stable within 10 %. A fit for the current results in the solid black line in the figure and $A_{RF} = 9.96 \cdot 10^{-15}$ m^2 and β_{RF}=166.

In the same series of RF pulses and the same helium neutral pressure the ion source was switched on. This resulted in a plasma density, measured by the Langmuir probe, of $n_e^{He} = 7.5 \cdot 10^{14}$ m^{-3}. The measured rectified current with the ion source working is presented by stars in Fig. 5.3. A polynomial fit for the points below 60 kV is shown by the black dotted line. It should be noted that no increase of the light emission was observed during the RF pulses in the presence of the plasma neither in the vacuum chamber nor

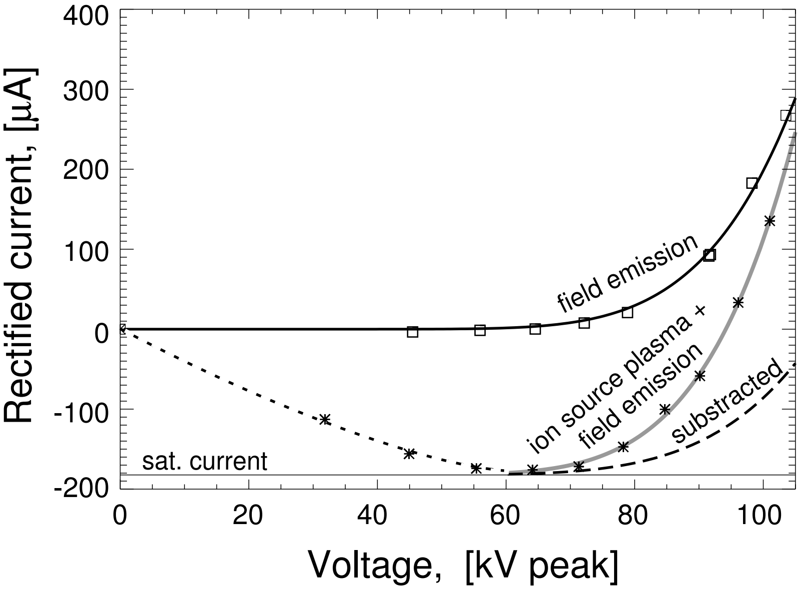

Figure 5.3: *Rectified field emission current and plasma current. Squares - measured rectified current, black solid curve - fit to the formula (2.14). Stars - measured rectified current in plasma of the ion source, black dotted curve - polynomial fit to stars, gray solid curve - fit to the formula (2.14) accounting the saturation current. Black dashed line - difference between the fits for the currents by a subtraction of the solid black and the solid gray curves.*

in the coaxial electrodes.

In the experiment the negative rectified current grows almost linearly at voltages below 46 kV and saturates at a voltage of about 60 kV. That is about the voltage threshold for field emission current for this case. We note that the saturation happens at relatively high voltages.

At a voltage of 50 kV and a density of quasineutral plasma $\simeq 7.5 \cdot 10^{14}$ m^{-3}, the sheath thickness according to equation (3.18) (substituting the Bohm ion current by the current of the ion beam as discussed in chapter 4) is 13 cm. That is larger than the dimensions of the vacuum chamber in the injection region (≈15-20 cm). Therefore we have the case of a thick sheath for the high voltages not only in the gap of coaxial electrodes, but also in the gap consisting of inner RF electrode and grounded vacuum chamber wall. From this point of view one can conclude that the collected current of charged particles increases until the voltage is increased so much that the rectified current (3.41) is reached.

The current at voltages higher than 60 kV contains already both plasma and field emission components. Using the experimental points for these voltages and taking the saturated plasma rectified current as a zero level, one can fit the current as a field emission current. The fit results in $A_{RF} = 1.27 \cdot 10^{-14}$ m^2 and β_{RF}=169 and the gray curve in Fig. 5.3.

Thus one sees an increase of the positive component of the rectified current. The increase is shown in Fig. 5.3 by the dashed black line which is the result of the subtraction of the positive component with plasma and the positive current without plasma. The increase is observed also with other plasma injection parameters. We can note that the positive rectified current is changed when an external plasma is present. However it is rather difficult to determine the exact reasons for the current increase since a few effects act simultaneously. At least three processes can contribute to the rectification current:

1. *Ion bombardment and modification of the surface.*
   Ions modify the surface structure (also due to focusing to the tops of microprotrusions (section 2.6.2)). Eventually this results in the decrease of the field amplification factor β_{RF}. However during the bombardment, an increased field emission yield may occur (charged particles can pre-heat the emission centers and excite metal electrons).

2. *Secondary ion-electron emission.*
   At high ion energies the emission has a yield comparable to or even higher than unity (see section 2.6.5). The total yield of the emission is proportional to the integral ion flow to the surface and is not directly connected to its density (or surface area). However in the gap between the coaxial electrodes, the electric field is higher near the inner electrode. If the injection of ions into the gap is assumed homogeneous, the ion flux is higher to the inner electrode due to the distribution of electric field. This may lead to the positive rectified current. Also an electric field distribution in the 3D geometry of the "parasitic electrodes" - vacuum chamber and the front surface of the inner conductor affects the rectified current by different total yields of the secondary emission.

3. *Volume ionization.*
   If only ionization by electron impact is considered, it is stronger in the RF period corresponding to the field emission from the inner electrode since electrons emitted by electric field contribute to the ionization in addition to externally injected electrons. In principle this can result in a contribution to the positive rectified current. On other hand an increase of the time-averaged plasma density results in the negative rectified current. Ion impact ionization should contribute more to the negative rectified current by producing charged particles in the volume.

An increase of the positive current is observed when one switches from the case of no external plasma to the case with plasma. Though the reasons of the increase can not be distinguished exactly (we can only say a contribution of ionization is less probable than a contribution from the processes occurring on the electrodes since also no light emission - no excited atoms were observed from the volume), this observation confirms that the processes of generation of charged particles in a high voltage electrode gap are significantly enchanced when an external plasma is supplied.

The existence of a plasma density of the order of 10^{15} m^{-3} at low neutral pressure $p_{He} \leqslant 0.1$ Pa does not influence the high voltage RF breakdown. Arcing is initiated with no detectable difference compared to the vacuum arc. Also the Q-factor does not change (the change is within the error bars, the error being about 10% for the Q-value). In Fig. 5.4 the measurements of voltage depending on the net RF power are presented by

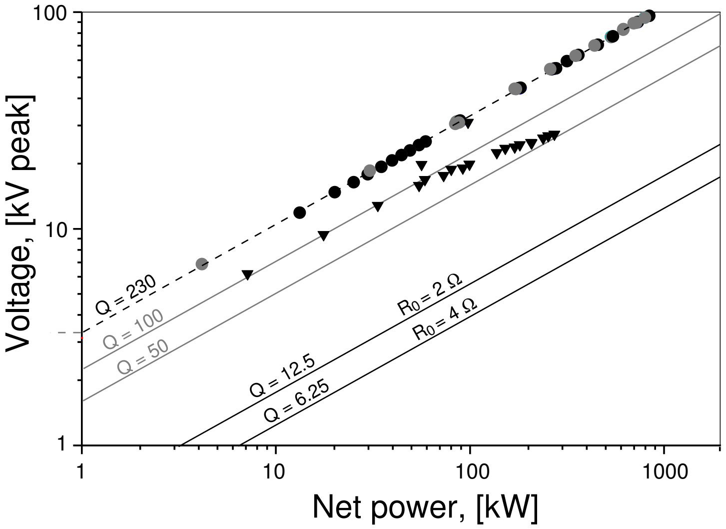

Figure 5.4: *Operation with and without ion source. Black circles - measurements in vacuum, black dashed line - fit for Q=230, gray circles - measurements at low neutral pressure with the presence of the external plasma, black triangles - measurements in the semi-self sustained RF glow discharge in He, black lines correspond to* $Q = 12.5$ *(ICRF antenna operation with* R_0*=2 Ω) and to* $Q = 6.25$ *(*R_0*=4 Ω).*

black circles for the vacuum case and by gray circles for the case with the external plasma presence at the pressures of helium below 0.15 Pa. For comparison with the voltages and powers of the real ICRF antenna operation, the maximal voltages on the antennas are shown for two values of the effective resistance R_0: $R_0 = 2\ \Omega$ and $R_0 = 4\ \Omega$.

5.1.6 RF breakdown at an increased neutral pressure

RF breakdown may be initiated if the neutral pressure is increased to the higher values (e.g. $p_{He} \geqslant 0.15$ Pa). Furthermore the pressure required to ignite a gas breakdown depends on the fact whether the external plasma is present or not.

The experiments with ignition of RF glow discharges were conducted at the closed (grounded) configuration of the DC circuit.

Self-sustained discharge

Ignition of a self-sustained RF glow discharge follows the Paschen curve. A stable threshold He pressure for ignition of a glow discharge can be obtained only by intensive conditioning in the He glow discharge at low RF voltages. The pressure required to ignite the glow discharge in He before the conditioning at 80 kV is $p_{He} = 0.5$ Pa. After the conditioning the threshold pressures for 80 kV are $p_{He} = 2$ Pa for He and $p_{air} = 0.18$ Pa for air.

The resonator of the ICRF probe does not allow for matching the high voltage self-sustained glow discharge. To reach the high voltages required for the glow ignition one

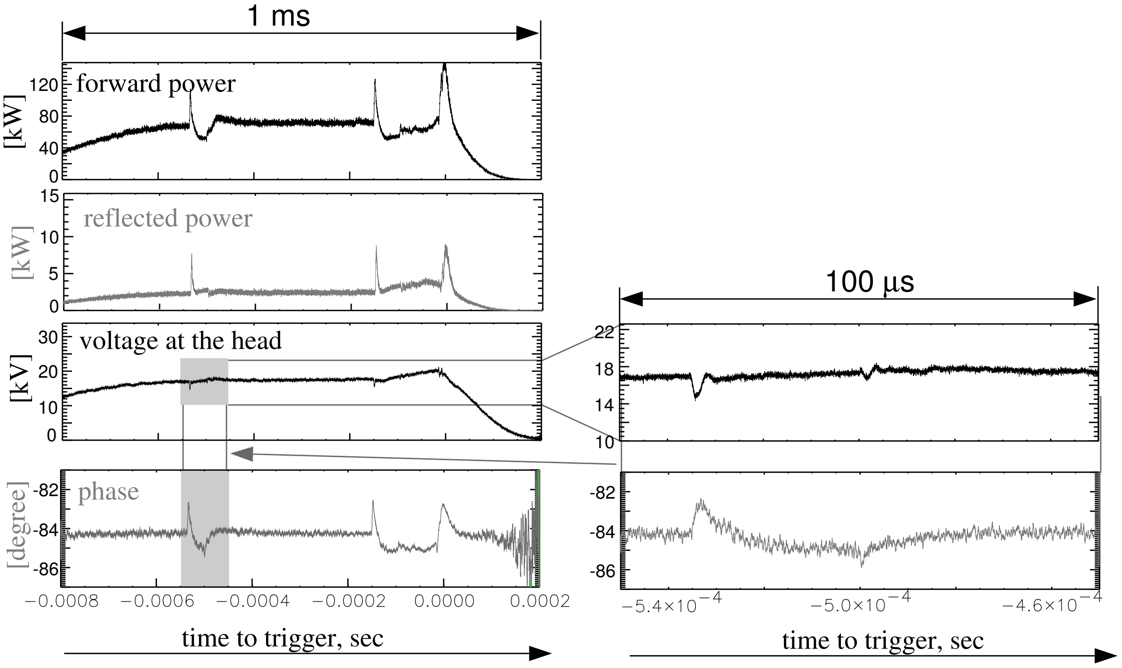

Figure 5.5: *Arcing phenomena in a semi-self-sustained RF discharge.*

needs the vacuum matching position, at which the ignition of the discharge results in almost total reflection of the power to the RF generator. The ICRF probe does not allow for fast change of matching position (see section 4.1). For this reason the transition of RF glow discharge to arc discharge can not be studied. However when an external plasma source is switched on, the semi-self-sustained discharge (see section 2.7.4) can be ignited which can be matched rather well.

Discharge with external ionization

At neutral pressures of $p_{He} = 0.15$ Pa and $p_{air} = 0.03$ Pa, and corresponding plasma densities $n_e^{He} = 9 \cdot 10^{14}$ m^{-3} and $n_e^{air} = 2 \cdot 10^{15}$ m^{-3} measured by the Langmuir probe, the semi-self-sustained RF glow discharge is ignited for the whole range of operational voltages: from 2 to 30 kV. The maximal achievable voltage is restricted by a mismatch of the matching circuit and its non-linear dependence on the power (see Fig. 5.4). No resolvable dependence of the threshold pressure on the voltage applied is observed in the above mentioned range of voltages. As expected from chapters 2 and 3, the ignition of the discharge is accompanied by a plasma density increase and leads to an increased negative charge collected by the inner conductor.

The Q factor of the semi-self sustained discharge is substantially lower than that in vacuum. Voltage measurements for the He discharge are presented in Fig. 5.4 by triangles. It is also observed that voltage dependence versus power does not fit the quadratic law (1.11)[1]. The quality factor of the resonance at a net power below 50 kW is about 100 and corresponds to the power dissipation of about 56 % of the net power at the open end according to equation (4.4). At a power of 300 kW $Q \approx 52$ corresponds to 77% power dissipation level. The non-linear dependence on the power is a typical feature of a glow discharge (see I-V characteristics in section 2.4.2).

The semi-self-sustained discharge has another interesting feature. Cathode spots appear on the inner electrode at RF voltage higher 5 kV. Furthermore for the voltage lower than 20 kV (peak) the cathode spots do not evolve into an arc discharge. In Fig. 5.5 measurements for this effect are shown. The measurements include forward power, reflected power, voltage at the probe head and the phase. The spots in the RF semi-self-sustained discharge have a characteristic time of formation from 1 to 3 μs. The phase change during a spot ignition is about 2°. This indicates a local character of the change of the increased discharge current. The system recovers from the first spike (corresponding to the cathode spot) to the initial value after 30 μs (see e.g. phase measurements in the figure). The last spike is probably an ignition of several spots which lead to a more pronounced reaction. However no full arc is developed for the pulse shown in Fig. 5.5. The damage of the electrodes after the appearance of the spots on the inner electrode is arc tracks (spread erosion) and can be observed by the CCD camera during the discharge as well as visually after the discharge.

5.1.7 Observation of multipactor

The multipactor (section 2.6.6) can be observed by an increase of the reflected power and a negative biasing of the inner conductor when the voltage on the probe is low enough for the resonance conditions to be fulfilled. These voltages exist usually when the power of the RF generator is ramped up to the eventual output power value or the RF power is decreasing to zero at the pulse end.

Multipactor in vacuum is better observed only at the initial stage of conditioning and is accompanied by a neutral pressure increase due to the charged particle stimulated desorption (section 2.6.4). The voltages corresponding to the multipactor in plasma lie in the range of 1-3 kV.

Even if the system is well-conditioned, the presence of the external plasma may lead to multipactor effects. As discussed in section 2.7.3, the multipactor plasma can exist at neutral pressures in the proximity of the Paschen curve. Furthermore, because of the electron-neutral collisions the voltage range for the multipactor existence is extended to the higher and the lower voltages. Precisely this extension of the voltage range is observed when the neutral pressure of helium is $p_{He} = 0.148$ Pa - a bit lower than the threshold for the ignition of the semi-self-sustained discharge. The measurements during the decrease of the power by the RF generator at the end of the pulse are shown in Fig. 5.6. The measurements were conducted with an open circuit when the scheme of the RF screening of the DC cable discussed in section 4.2 was not yet applied. One sees that at a voltage of about 10 kV the reflected power increases, and an increased DC current starts to flow

---

[1] the role of the effective resistance R_0 in (1.11) can be played by an effective RF conductance of the open end of the probe.

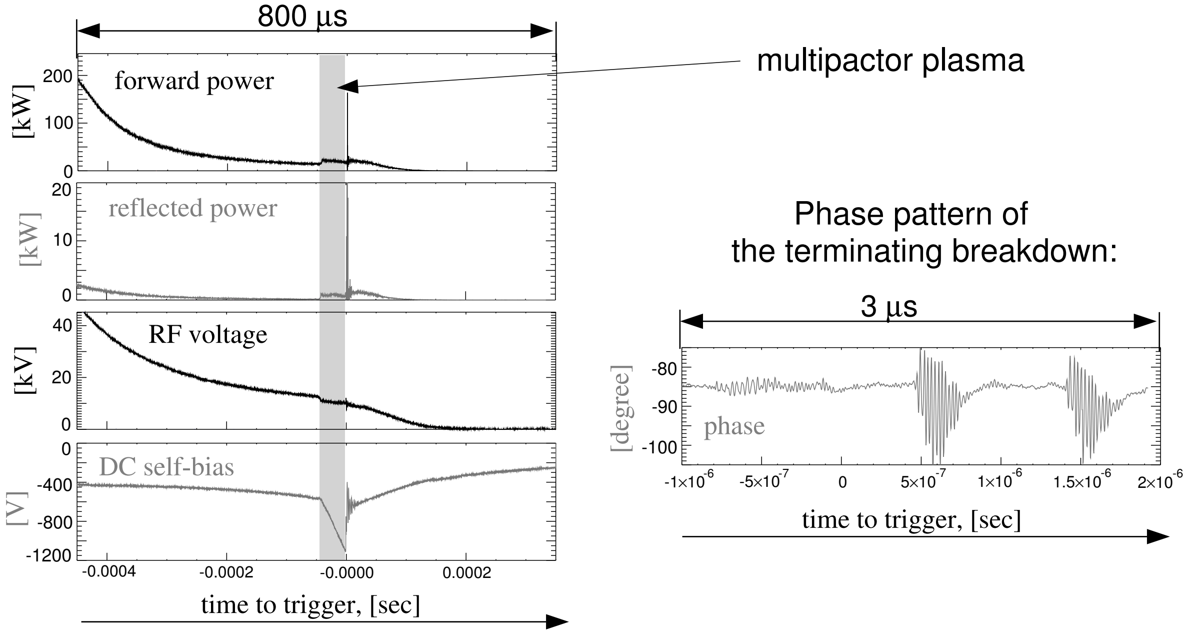

Figure 5.6: *Experiment with a high voltage multipactor plasma (gray region).*

through the inner conductor. This shows that the charged particles are either confined or generated by the multipactor effect. After the DC voltage reaches about 1 kV a breakdown occurs. This breakdown is accompanied by a noise pattern on the phase signal indicating that the breakdown does not occur in the electrode gap, but occurs on the insulation between the DC cable and the inner conductor at the grounded side.

The experiment illustrates that the multipactor plasma is already a high voltage phenomena when measured at increased neutral pressures with the plasma presence. It also shows that complications may arise with the parasitic RF power coupled to the DC circuit when an ICRF system with a varying DC boundary condition is developed.

5.2 Conclusions from the experiments in the test facility

The experiments in test facility showed that the ICRF probe system is suitable for experimental characterization of high voltage phenomena on ICRF antennas. These experiments allowed to perform overall tests of the system as well as reveal the basic candidate mechanisms which can lead to the RF breakdown on the antennas.

Field emission dark currents were observed by a positive self-biasing of the RF inner conductor at voltages corresponding to a probable ignition of vacuum arcs. Influence of plasma densities of the order of 10^{15} m^{-3} injected to the region of the coaxial electrode gap do not lead to a change in voltage stand-off if neutral pressure is kept below 0.15 Pa for helium and below 0.03 Pa for air as a working gas. However a modification of dark field emission currents (an increase) is observed in the presence of plasma. In this case the field emission currents compete with the currents carried to the electrodes by externally injected charged particles. At neutral pressures higher than the above mentioned values the semi-self-sustained discharge appears. The latter is a form of RF glow discharge and is ignited at pressures about one order of magnitude lower than a pressure required for ignition of a self-sustained glow discharge (discharge without external plasma injection). The semi-self-sustained discharge can be transformed into an arc discharge by formation of cathode spots on the surface of the inner conductor if the RF voltage exceeds 20 kV. At lower voltages the appearance of single cathode spots does not necessarily lead to the glow-to-arc transition.

5.3 Experiments in ASDEX Upgrade

The measurements on ASDEX Upgrade midplane manipulator were made in the 2001/2002 experimental campaign. The knowledge of the processes causing the high voltage breakdown in test facility was used. Availability of different diagnostics on AUG makes possible to look for correlation of the signals from the RF probe with different processes in the plasma edge.

Experimentally observed density profiles in the limiter shadow, where the ICRF antenna straps or RF probe head are situated, indicate that diffusion of particles is more enchanced than described by Bohm cross-field diffusion [80, 78] or from the neoclassical transport described briefly in chapter 1. Furthermore a description based on the diffusive model including increased diffusion coefficients can not reflect a burst-like particle transport and often non-exponential (flat) plasma density profiles in the SOL far from the last closed flux surface. These features are observed in many experiments, e.g. [94, 95, 96, 97, 99].

Therefore the transport should be described by combining both diffusion and convection models [100, 101] since the convection is a significant part of the total radial transport and it results in the higher plasma density in the SOL. The convection is often associated with $\boldsymbol{E_f} \times \boldsymbol{B}$ drift [17, 97, 102]. Here $\boldsymbol{E_f}$ is a an electrical field connected with turbulent plasma structures which may appear as a result of the development of a wide class of drift instabilities occurring in the SOL plasma [17]. The radial component of the electric field $\boldsymbol{E_f}$ is responsible for the poloidal drift of the turbulent plasma structures while the existence of poloidal component of the electric field moves plasma formations radially. The existence of a strong poloidal electrical field can be explained by a $\boldsymbol{\nabla} B$ polarization of a plasma formation (also called "blob" or "filament") [102, 103] which is initially detached from the edge of the main plasma after development of an instability. The presence of the high electrical poloidal fields in the SOL was treated in [16] where it was shown that the fields appear in the SOL from different electrostatic plasma potentials of the flux tubes, the latter being intersected by divertor and limiter surfaces. The different plasma potentials may exist due to the existence of the space charge sheaths which screen these potentials from the zero potential of the wall (see chapter 3). This effect is often referred as a "finite sheath resistivity".

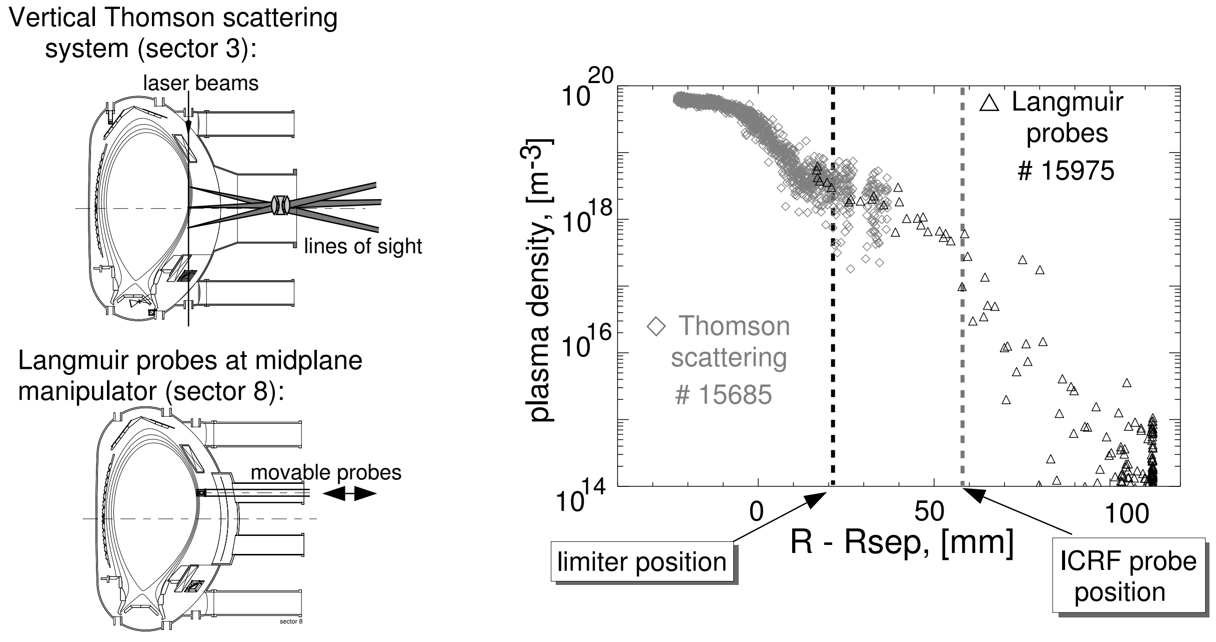

Figure 5.7: *Thomson scattering and Langmuir probe systems for measuring density and temperature profile of the edge plasma on AUG. Profile of electron density with respect to separatrix position.*

The turbulence in the SOL results in the convective $\boldsymbol{E_f} \times \boldsymbol{B}$ transport. The turbulent structures are sometimes also considered as a reason to increase the spatial scale of transport because the perturbed magnetic and electric fields can lead to an enhanced transport of charged particles (not trapped inside the turbulent structures) across these structures. An existence of coherent turbulent structures in the SOL and a plasma interchange between them may further increase the radial transport [101].

Edge localized modes (ELMs) [104, 105, 106] are observed at the plasma boundary in H-modes. ELMs are initiated by magnetohydrodynamic instabilities and lead to the very steep increase of the plasma density in the scrape-off-layer. ELMs are registered practically by every diagnostic system for the edge plasma, for example, Mirnov magnetic coils, D_α divertor radiation, Langmuir probes, etc.

Therefore the plasma density in the limiter shadow shows very non-stationary behavior. This affects the measured profiles of the edge plasma density and electron temperature which can be measured with the help of the diagnostics available on AUG.

5.3.1 Measurements of plasma density

In order to measure the plasma density at the radial position of the antenna strap a Thomson scattering system [107] and Langmuir probes may be used (see the schemes on left side of Fig. 5.7).

The Thomson scattering system deduces the density from scattering of the vertical

Nd:YAG-laser beam on the electrons of plasma. Measurements by the system show usually small gradients of plasma density behind the limiter but the plasma density values are very scattered because of the small sensitivity of the diagnostic to the typical densities present behind the limiter.

The second system is a set of Langmuir probes that can be mounted on the midplane manipulator [108]. Since the ICRF probe and Langmuir probes can not be mounted simultaneously on the manipulator, the same configuration of the AUG plasma and heating power was used to get information on plasma parameters for ICRF probe operation.

Though the measuring systems are situated in different toroidal sectors of ASDEX Upgrade (Thomson scattering - sector 3, midplane manipulator - sector 8, overall number of sectors - 16), we assume the axial symmetry of the tokamak with equal conditions and edge plasma parameters in the different tokamak sectors.

The profile of the electron density measured by the diagnostics is presented in Fig. 5.7 for the discharge with Edge Optimized Configuration (EOC) (see the description in chapter 1), 5 MW neutral injection heating power, 1.1 MW ICRH power, and a line-averaged plasma density of $9{\cdot}10^{19}$ m^{-3}. The measurements presented in Fig. 5.7 were made between ELMs. The measurements of electron temperature in the limiter shadow result in a value of ≈15-20 eV almost independent of the position in the region 30 mm $< R - R_{sep} <$ 60 mm.

One can see that in the limiter shadow ($R - R_{sep} >$ 22 mm) the density profile is rather flat to about $R - R_{sep} \approx$ 50 mm. The plasma density here is modulated by the intermittent transport by about 50 % (see also [98]). The plasma density for the positions $R - R_{sep} >$ 50 mm becomes even more scattered since it is sustained here mostly by the intermittent transport. Approximately at the position corresponding to the most frequently used position of the ICRF probe (Fig. 5.7), the averaged plasma density for this discharge starts to decay further. This is connected to the fact that other components of the wall start acting as limiters. At the probe position (taking into account about 5 mm uncertainty of the inner conductor collecting area) the density varies from $2 \cdot 10^{16}$ m^{-3} to $4 \cdot 10^{17}$ m^{-3}.

If one compares the measured densities with the diagram 3.2 from chapter 3 at the frequency of about 50 MHz, one finds out that the densities correspond mostly to the region when the sheath thickness is comparable or higher than the 14 mm interelectrode distance of the probe. This situation is changed when an ELM comes to the outer wall of the tokamak. During this time the plasma density in the limiter shadow increases by a factor of 10-100. The sheath thickness during ELMs becomes small compared to the gap. Therefore the plasma density during ELMs is increased to the values that correspond to the regime of the thin sheath ($s < d$, from section 3.3.2) while for the densities between ELMs, the regime of the thick sheath is mostly realized ($s > d$, from section 3.3.3).

As an illustration to the intermittent character of the density changes in the limiter shadow, the measurements by the Langmuir probe with a radial position almost constant in time are presented in Fig. 5.8. These were performed by H. W. Müller et al. [99] on the AUG midplane manipulator. The Langmuir probe was placed 3.6 - 4 cm behind the limiter in a plasma configuration with a distance of about 5 cm between the separatrix and the limiter.

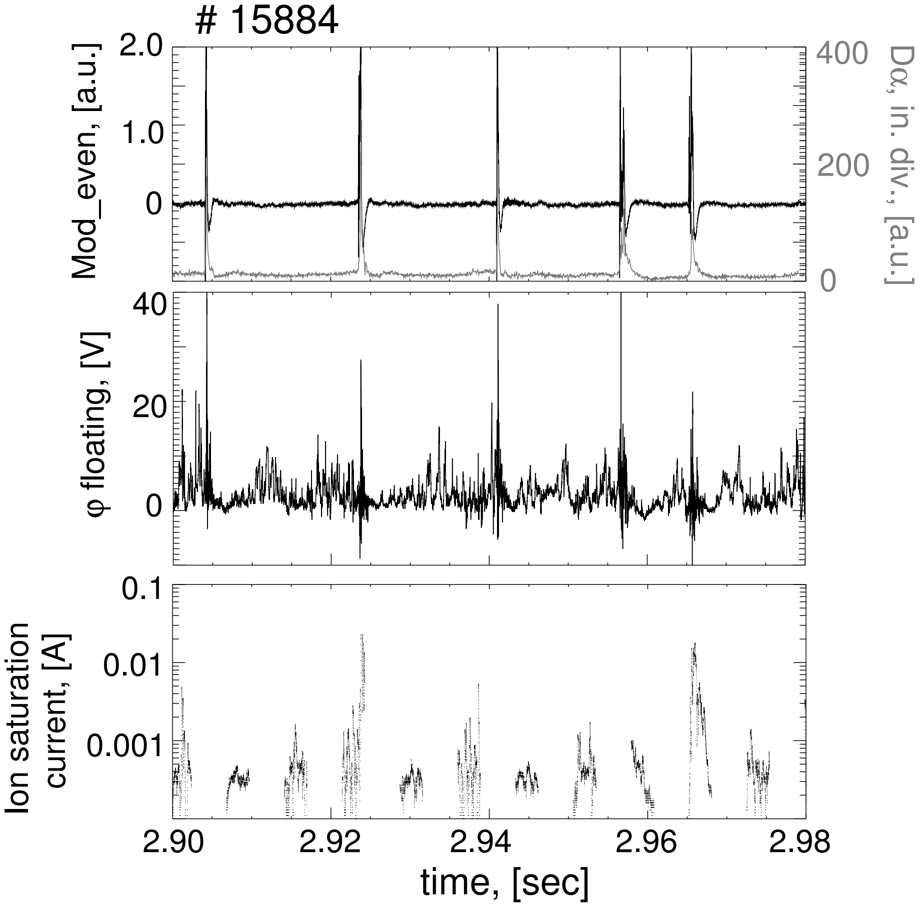

Figure 5.8: *Floating potential and ion saturation current from the Langmuir probe measurements in the limiter shadow performed in [99]. The measurements are shown together with magnetic probe (Mirnov coils) signal and D_α radiation from the divertor.*

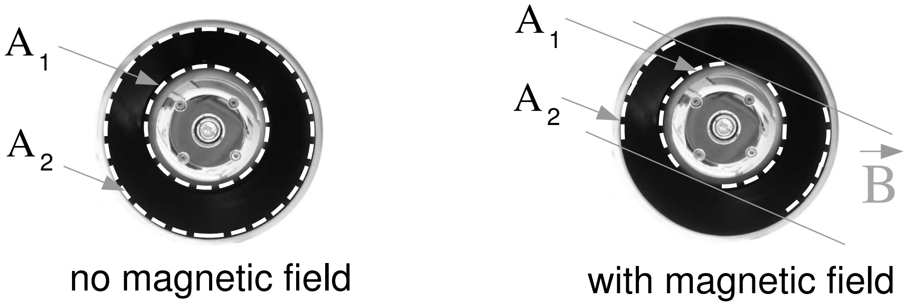

Figure 5.9: *Geometrical asymmetry of the probe without and with magnetic field.*

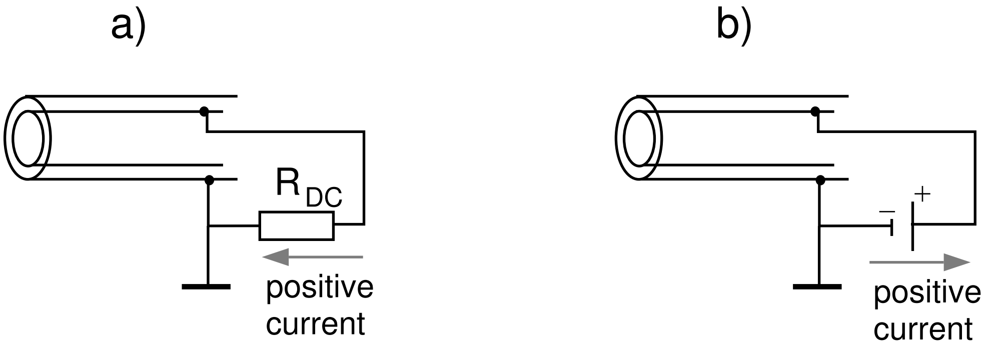

Figure 5.10: *Definition of direction of the DC currents in the external DC circuit: a) definition according to the self-biasing effects (section 5.1.3; b) - definition according to the Langmuir probe characteristic.*

5.3.2 Geometrical asymmetry of the probe

The probe geometry is cylindrical. However the conductors of the probe are not exactly coaxial because of the finite mechanical inaccuracy. There exists a displacement of the inner conductor head with respect to the outer conductor. The displacement of the probe head before the probe was mounted on the midplane manipulator was 2.5 mm to the upper side of the probe. This results in a modification of the electrode gap distance in the vertical direction from an initial value of 14 mm to 11.5 mm and 16.5 mm for the upper and the lower gaps respectively.

When the probe is used in a magnetic field, the effective collection of charged particles along the magnetic field lines changes as shown in Fig. 5.9. One can see how the effective areas A_1 and A_2 of the inner and outer conductor respectively change when the magnetic field is switched on. A big uncertainty exists in the displacement of the inner conductor and therefore A_1 and A_2 is not exactly known for the case with magnetic field. The best way to determine the real asymmetry is to measure the DC voltage-current characteristic and compare the branches of current saturation of the characteristic.

At first let us note that the negative and positive directions of the rectified current defined in section 5.1.3 are opposite to the current directions defined for a conventional DC-characteristic of a Langmuir probe. The latter has a definition of electron current as a positive. We separate the use of these two definitions as follows:

- if the DC circuit is closed and the rectified current is measured, the current directions are defined as in section 5.1.3 (Fig. 5.10a).

- if a DC power supply is connected to the DC circuit, the current direction are defined as for the conventional voltage-current characteristic of the Langmuir probe (Fig. 5.10b), i.e. opposite to the definition in section 5.1.3;

The DC I-V characteristic for the H-mode discharge of the same configuration as for the discharges used for the density profile measurements (Fig. 5.7) is presented in Fig. 5.11.

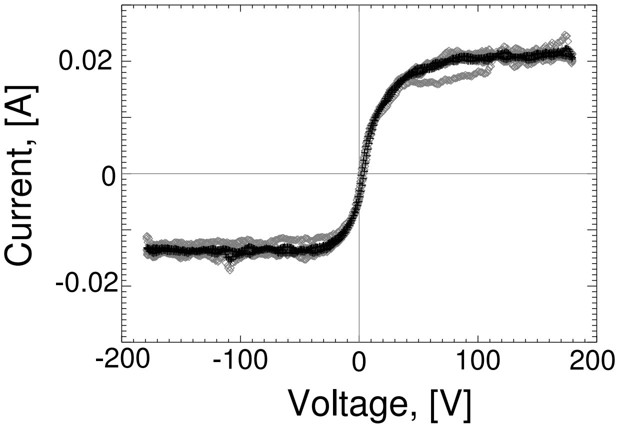

Figure 5.11: *DC voltage-current characteristic for the approximately coaxial probe in magnetic field. Gray - experimental data, black - the averaged data.*

The characteristic was measured between the ELMs. From the characteristic one can see that the saturation currents do not differ much. Therefore the characteristic is close to the characteristic of a double Langmuir probe and the probe asymmetry is rather small (A_1 and A_2 are close to each other). The value of negative (ion) saturation current 14 mA is less than the value of the positive saturation current of 20 mA. This indicates that the inner conductor area A_1 is still smaller than the outer conductor area A_2. From the overview of the asymmetries in chapter 3 one can anticipate that when an RF voltage is applied to the probe, the DC self-bias voltage will be negative in the case of the opened external DC circuit. In the case of the closed DC circuit, a negative DC current will flow from the large electrode to the small one according to the definition in Fig. 5.10a.

The measured characteristic gives an electron temperature of $T_e \approx 15$ eV in agreement with conventional Langmuir probe measurements (section 5.3.1). Taking a density of $2 \cdot 10^{16}$ m^{-3} one gets an ion saturation current density of about 17 A/m^2. For the 14 mA ion saturation current measured by the ICRF probe this results in the effective collecting area of the inner conductor A_{eff} $\approx$4 cm^2. For the cylinder of 1 cm height and 5.5 cm diameter one has about 35 cm^2. The small measured A_{eff} is obviously connected with the limiter configuration of the RF probe and the fact that charged particles are collected by the probe (a large Langmuir probe) and in this configuration the plasma density is decreased. The outer conductor plays the role of a limiter since the inner conductor is placed 6 mm deep inside the outer (see Fig. 4.4).

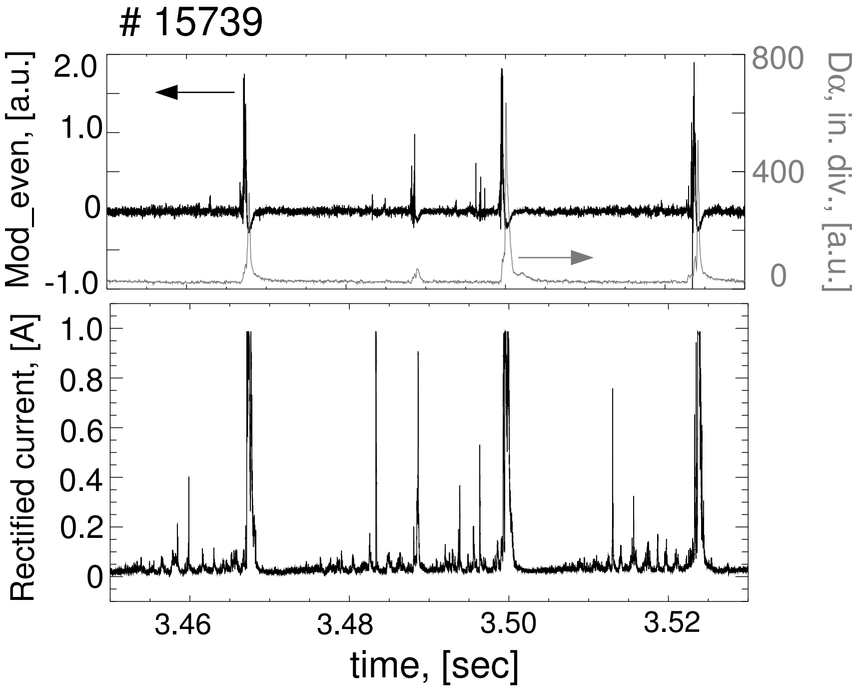

Figure 5.12: *Upper signals: Mirnov coils, D_α radiation level from the inner divertor, the rectified current of the ICRF probe.*

5.3.3 Asymmetry of RF currents

To characterize interaction of the ICRF probe and the SOL plasma we apply a RF pulse to the probe during AUG discharge.

Expectations and experiment

When the DC cable connected to the inner conductor is grounded through the resistance R_{DC}=10 Ω, the electrodes are considered to be DC-grounded and the rectified current is measured from the voltage drop on R_{DC}. From the discussion above we anticipate a negative current to flow (using the definition of Fig. 5.10a). However experimentally (Fig. 5.12) we observe that the rectified current is positive. The reason lies in the combination of the 3D geometry of the probe and the magnetic field to be discussed later.

Figure 5.12 shows a rectified current flowing in the direction from the inner conductor to the outer conductor (positive) that sometimes correlates with the signals from Mirnov coils and D_α radiation from the inner tile of the AUG divertor. The magnetic and D_α signals reflect the global changes of the plasma which happen due to ELMs or ELM-like events. The small events between ELMs are often observed only on the rectified current. This gives an indication that the probe is sensitive to local changes of the SOL plasma which are probably related to ELM precursors. These are also observed by the Langmuir probes [99] (see Fig. 5.8).

The intermittent transport and ELMs are usually associated with fluctuations in a broad frequency range. In Appendix D, frequency spectra for the signals of the rectified current and phase are presented for the type I ELM precursors and type I ELMs. A time resolved picture of ELMs is described below in section 5.3.7.

Hypothesis for positive rectified current

The reason for the positive rectified current can be explained on the basis of a hypothesis which takes into account the 3-dimensional geometry of the probe and the surfaces intersected by magnetic field lines at low angles α (Fig. 5.13).

We are interested in particles which reach the inner conductor. As is seen in Fig. 5.13a, in the probe we have a limiter configuration with the outer conductor as the limiter and the inner conductor 6 mm behind that limiter. When no RF voltage is applied, the geometry does not allow for electrons or low-energetic ions (perpendicular energy less than 5 keV for a magnetic field of 1.5 Tesla) to reach the inner electrode surface. In the limiter geometry at low α the component perpendicular to the electrode surface is defined by parallel connection length $l_{max,\|}$:

$$d_{e,i,\perp} = l_{max,\|} \cdot \sin\alpha \tag{5.1}$$

where $l_{max,\|}$ - is an actual distance between two limiters. The angle α is not equal to zero: a finite angle exists between the manipulator axis and the major radius of the torus. Mechanical errors, direction of the main magnetic field and presence of a ripple of the magnetic field between the poloidal coils of the tokamak can change the angle. The probe has also rather large dimensions which are not aligned with the curvature of the toroidal magnetic field and result in a relatively large α in some areas of the probe surface.

In particular, the estimation of α due to the plane front surface of the inner conductor and the finite radius of curvature of the toroidal field (major radius of the AUG tokamak) results in $\alpha \approx 1.5^o$ and $d_{e,i,\perp} = (r_{outer})^2/(4R_{major}) = 0.3$ mm (where r_{outer} is the outer conductor, R_{major}-major radius of the tokamak). This displacement is small and can be neglected. The difference in α due to the above described reasons is tolerable until α is higher than 3^o. This leads to $l_{max,\|}$ comparable to the radial distance of 6 mm between the inner and the outer electrodes. The latter statement is only valid if ions with high perpendicular energy (and gyroradius of few mm) are not accounted for.

We know that when an RF voltage is applied on the inner conductor, it is possible to use a drift approximation for electrons while for ions we need to account the full dynamics (section 3.4.1). Let us estimate the ratio of displacements between electron and ion plasma components that give a ratio of the corresponding fluxes.

Electrons suffer the polarization drift (3.46) that is proportional to the time derivative of the electric field. The displacement of the electron during half of an RF period is:

$$d_{e,\perp} = 2 \cdot \frac{m_e E_\perp}{eB^2} \tag{5.2}$$

We see that the displacement does not depend on the frequency.

For low RF voltages ($V_0 < 1$ kV) the ion displacement can be considered to be gyroradius:

$$\rho_i = \frac{m_i v_{Ti}}{eB} \tag{5.3}$$

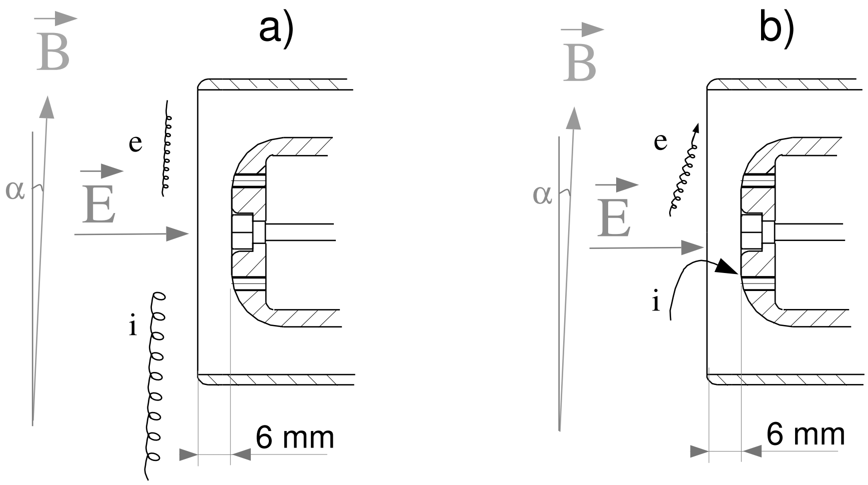

Figure 5.13: *Collisionless movement of charged particles to the front surface of the ICRF probe. a) case of DC voltage on the probe, b) case of high voltage RF voltage on the probe at* $\omega_0 \gtrsim \omega_{ci}$.

The ratio between 5.2 and 5.3 is:

$$\frac{d_{e,\perp}}{\rho_i} = 2 \cdot \frac{m_e}{m_i} \cdot \frac{v_{E\times B}}{v_{T_{i,\perp}}} \tag{5.4}$$

for deuterium the last formula is written:

$$\frac{d_{e,\perp}}{\rho_i} = 7.867 \cdot 10^{-4} \cdot \frac{E,\ [\text{MV/m}]}{B,\ [\text{Tesla}]\sqrt{T_{i,\perp},\ [\text{eV}]}} \tag{5.5}$$

The ratio is much less than unity for a realistic range of parameters: $E < 10$ MV/m, B=1-4 Tesla. However the ion gyroradius at $T_{i,\perp}$ <1 kV is smaller than 3 mm, so the ions do not pass the 6 mm distance to the inner conductor (if the angles α discussed previously are sufficiently low), and the outer conductor still works as a limiter.

Ions can be collected by the front surface of the inner conductor when higher RF voltages are applied to the inner electrode (Fig. 5.13b, see also [73]). The perpendicular ion energy is changed by the application of high RF voltages, because the electrical field is changing during the period of gyromotion. In this case we can not use the concept of ion gyroradius nor the concept of the perpendicular temperature $T_{i,\perp}$ (see also the discussion in section 3.4).

If the RF voltage is high enough, one can use an estimation of the ion displacement as a displacement without magnetic field according to equation (2.20). This kind of estimation can be applied if the displacement is much larger than ion gyroradius. In this case one neglects the change of the velocity direction of an ion due to the Lorentz force defined by the presence of the external magnetic field . The approximation is applicable for a voltage $V_0 > 10$ kV. Taking the displacement of the electron due to the polarization drift from 5.2, the ratio of electron and ion displacements during half of RF period is:

$$\frac{d_{e,\perp}}{d_{i,\perp}} = \frac{m_e}{m_i} \cdot \frac{\omega_0^2}{\omega_{ci}^2} \ll 1 \tag{5.6}$$

The ratio is also smaller than unity as the frequency of the RF probe is close to $\omega_0 \approx 4\omega_{ci}$.

Therefore for both cases we have the perpendicular ion current much larger than the perpendicular electron current. Furthermore, for high RF voltage the ion displacement can be of the order of 1 cm (see also Fig. 2.6). This allows ions far from the inner conductor to be collected by the probe. If ions are collected from a distance of more than 6 mm where the plasma density is higher (the outer conductor does not really work as a limiter in this case), then the ion flux to the probe should be further increased.

One should also consider that only ions can be collected which have a velocity $v_{i,\|}$ parallel to the magnetic field low enough to have the parallel displacement of ions during half of RF period smaller than diameter of the inner conductor d_{inner}:

$$l_{i,\|} = \frac{v_{i,\|}}{f_0} < d_{inner} \tag{5.7}$$

Assuming that the parallel velocity equals to the ion acoustic velocity v_{si}, for f_0=50 MHz and T_e=15 eV one can estimate $l_{i,\|} \approx 0.54$ mm for RF period. Therefore the plasma ions having v_{si} can be considered motionless during RF cycle in parallel direction if parallel electric fields are defined only by electron temperature. Also ions with high parallel energies can be collected: parallel energies below 100 keV result in the displacement $l_{i,\|}$ below 4.4 cm. However at high energies one needs to calculate the exact ion trajectories to account for collected ions.

Experimental observations show that at high RF voltage the background rectified current (without intermittent events) grows weakly when the RF voltage is increased. This is explained by rather low densities of the plasma present in the scrape-off-layer between the ELMs and the events. In the case of voltages above 10 kV most ions within a certain radial distance (approximately corresponding to the displacements from Fig. 2.6) from the plasma are gathered by the limited collecting surface - front surface of the ICRF probe. Furthermore no steep transition happens when the displacements of ions exceed (according to Fig. 2.6) the radial distance between the inner and the outer electrodes. This indicates that the ions from the region in front of the probe have more complicated trajectories which cannot be quantitatively described in terms of the displacements calculated without magnetic field.

Thus the existence of the positive ion current can be explained by the fact that the front surface of the inner electrode collects predominantly ions. Furthermore the ions can be collected from the regions of higher densities. Therefore the time-averaged current is higher than the negative contribution of the rectified current expected from the DC measurements.

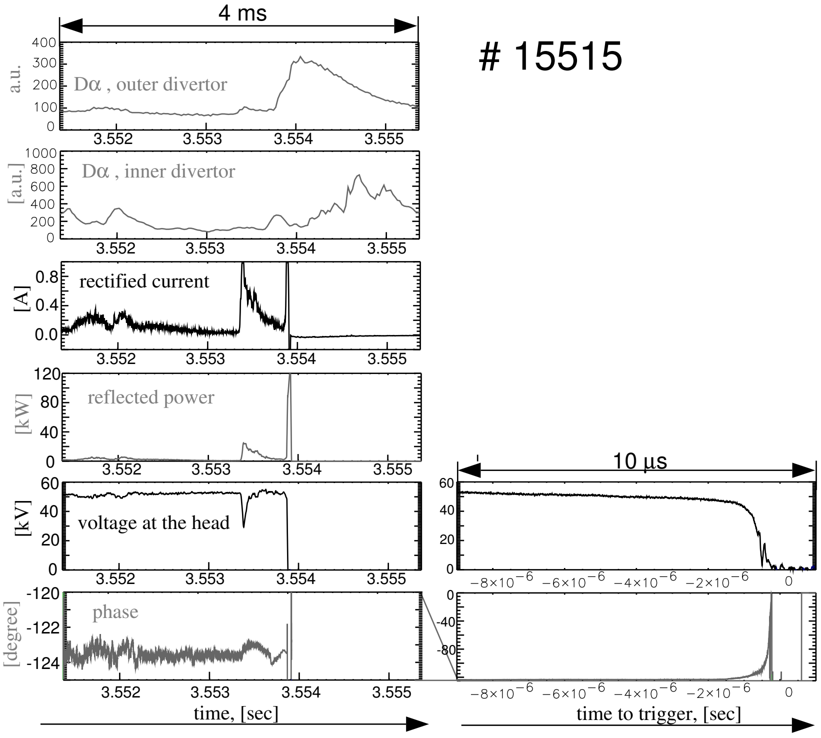

Figure 5.14: *High-voltage RF breakdown triggered by ELM instability.*

5.3.4 Measurements of the voltage limit

A strong influence of the plasma is seen experimentally on the voltage limitation. The breakdown correlates with ELM activity for most of the pulses.

The breakdown voltage is measured by making a linear power ramp. Two types of ramps are used: a fast one going from 0 to 750 kW in 50 ms and a slow one, from 0 to 750 kW in 300 ms. The matching is adjusted to have minimum reflected power in the middle of the power ramp (RF voltage of about 50 kV peak). The fast ramp has the advantage that the conductors of the probe are not heated substantially and the amount of gas desorbed (measured by the vacuum gauge) is rather low. On the other hand the fast ramp is not good for the precise measurements of the voltage limit which correlates with type I ELMs, since the time between ELMs can be a substantial fraction of the 50 ms ramp time. Therefore the second ramp was mainly used. Sometimes parasitic discharges can be ignited inside the coaxial system due to high gas desorption. This problem was solved by a very intensive conditioning in vacuum.

5.3.5 Influence of ELMs on voltage stand-off

Initially when the RF probe is not well-conditioned, the breakdown may correlate with any ELM activity observed on the signals from the magnetic probes or from D_α. After few conditioning shots with plasma the breakdown is caused mostly by type I ELMs.

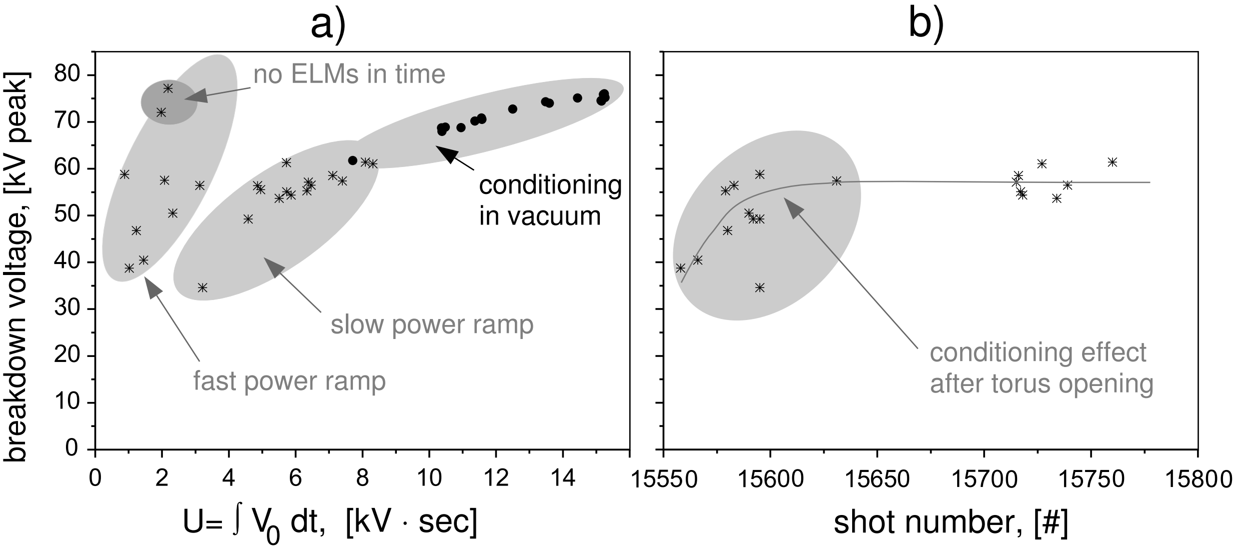

Figure 5.15: *Operation in vacuum and plasma. Stars - maximum voltage limited by plasma, circles - voltage limit in vacuum. a) Voltage limit versus voltage exposure parameter U; b) voltage limit in plasma versus shot number (after torus opening).*

In Fig. 5.14 the influence of type I ELM in the discharges with EOC plasma shape (see chapter 1 and section 5.3.1 for the description) is presented. The positive rectified current can rise up to few amperes during the type I ELMs. The phase transient of an arc after the ELM is very similar to that during the cathode spot formation in the semi-self-sustained RF glow discharge (Fig. 5.5) and develops in a characteristic time of 2 μs. We consider the first RF breakdown and corresponding maximal voltage before ELM to be the voltage limit of the system.

In Fig. 5.15a the voltage stand-off in AUG discharges (all breakdowns correlate with type I ELMs) and in vacuum is shown. We define the voltage exposure parameter as: $U = \int_0^{t_b} V_0 \cdot dt$, where t_b - time of the breakdown counting from the ramp start. The parameter U is shown on the x-axis of Fig. 5.15a.

The fast power ramp duration of 50 ms used for the voltage limit measurements is of the order of only a few typical ELM periods. Thus the voltage limit associated with the ELM appearance can be overestimated, because it is probable that there is no ELM at the time when the voltage on the probe corresponds to the limit. The second, slower power ramp is better suited for the measurements of ELM-correlated RF breakdown, though additional measures need to be applied to control gas desorption in the vacuum lines.

For the majority of points in Fig. 5.15a the early measurements correspond to lower breakdown voltages. The conditioning effect in vacuum can be observed in the beginning of each day of operation. Between the pulses of the ICRF probe in AUG plasma, the voltage stand-off in vacuum was sustained at the level higher than 75 kV by intense high-voltage conditioning between AUG discharges. One observes the conditioning effect for the maximal voltage in the presence of the AUG SOL plasma from shot to shot. The

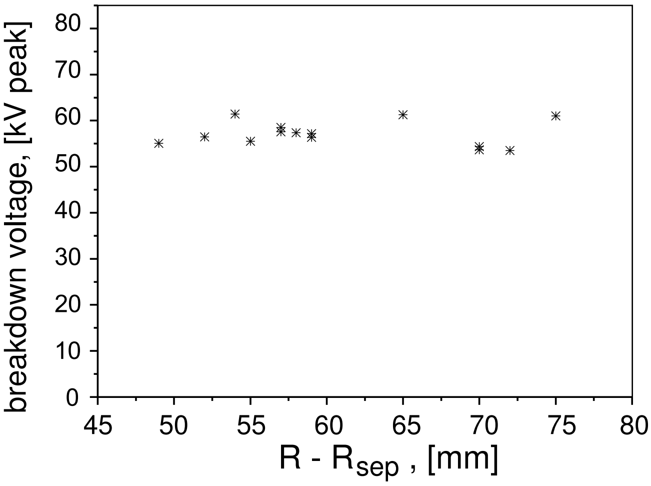

Figure 5.16: *Dependence of the voltage limit of the ICRF probe conditioned well in plasma versus radial position* $R - R_{sep}$.

conditioning effect with the plasma is more emphasised after the AUG torus opening (Fig. 5.15b). Therefore the surface state is important for the breakdown caused by ELM activity, and the intense conditioning of the probe in vacuum is a necessary but by far not sufficient measure to improve the voltage limit in the presence of plasma. Conditioning with plasma is required.

Variations of the distance between the well-conditioned ICRF probe head and the separatrix do not affect the voltage stand-off considerably if the breakdowns on the probe are triggered by ELMs. In Fig. 5.16 the dependence of the voltage limit associated with ELMs versus the radial position of the probe with respect to the separatrix is shown.

For the specific experiments (see below) only AUG discharges with EOC plasma shape are used.

5.3.6 Affecting voltage stand-off of the probe in AUG

A specific experiment was conducted to find out the influence of the DC biasing of the inner conductor on the voltage limited by the plasma presence. The probe was preliminary conditioned in vacuum and with plasma in 6 discharges. A series of very similar EOC discharges was made in sequence. For each discharge the same power ramp (from 0 to 750 kW in 300 ms) and a unique DC were applied. A balast resistance of 50 Ohm was used. To decrease the uncertainty connected with the probe conditioning the DC bias was changed in a non-monotonical sequence of voltages. The measurements are presented in Fig. 5.17. It shows that an application of DC voltage affects the maximum voltage which correlates with the time-averaged rectified current. The voltage limit of 55 kV without DC bias could be increased to 63 kV by suppressing the rectified current and reduced to 49 kV by increasing the current. Because of the finite ELM period, the real voltage limitation should lie between the voltages corresponding to the two last ELMs (in the

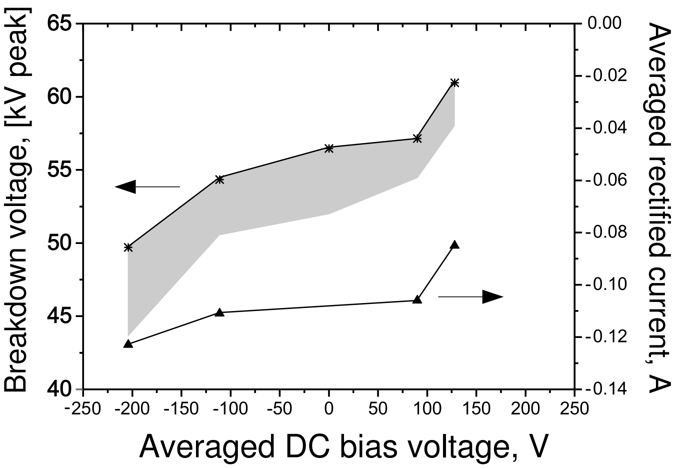

Figure 5.17: *Affecting the voltage stand-off by controlling the rectified current (the direction of the current is defined as in Fig. 5.10). Stars - voltage of the breakdown correlated with an ELM, gray regions - uncertainty of the voltage limit due to the finite ELM frequency, triangles - rectified current averaged between the two last ELMs.*

gray region in Fig. 5.17).

The experiment demonstrated that not only the voltage plays the decisive role in the RF breakdown development but also the particle fluxes to the electrodes, in particular the ion flux. From the discussion in section 5.3.3 one knows that the rectified current is a measure of the time averaged ion flux perpendicular to magnetic field and collected by the probe. Biasing the RF electrode to the voltages of the order of 100 V changes the ion time-averaged current by approximately 10%. This means that 10% of the time averaged ion current is carried by ions with low perpendicular energy (low in terms of high RF voltage).

We understand the effect of the change of the voltage limit as follows. As is shown in chapter 3, the presence of the ion density in the electrode gap is beneficial for the values of the electric field on the surface. The latter is the most important parameter for initiation of RF breakdown on the electrode surface, if the surface effects are eliminated. Therefore to regulate the surface electric field, one should regulate the ion density in the gap between the coaxial electrodes of the probe as the first measure (electric field is more strongly dependent on ion density than on voltage). A change of the time-averaged rectified current indicates that the amount of ions penetrating into the electrode gap is changed respectively. If one does not use the simple assumptions from section 5.3.3, then ion trajectories in the RF electrical and static magnetic fields are rather complex. The application of relatively small radial DC electric field changes the perpendicular component of the ion trajectories. On the other hand the application of the DC electric field does not influence the penetration of electrons radially into the electrode gap since electrons can drift in the poloidal direction. Therefore DC biasing of the inner conductor influences the rectified current and the ion density injected perpendicular into the electrode gap. By applying a positive bias, the rectified current is decreased. This allows for having noticeably higher voltages for the same value of electric field, hence an increase of the power that can be launched by the ICRF antenna (voltage increase from 55 kV to 63 kV corresponds almost to 30 % increase in a possible power launched by the antenna).

Thus the influence of the DC biasing on the voltage stand-off stresses the role of the electrode surfaces which face the plasma and are oriented nearly parallel to the magnetic field. A decrease in the area of these surfaces can lead to a reduction of the number of the ions displaced by strong radial RF electric fields towards the antenna. If these ions are not collected by the antenna electrodes they oscillate in the radial electrical fields and can easily move along magnetic field lines during the time of several RF periods. Therefore by a reduction of the number of these ions, the density in the gaps between the electrodes oriented not parallel to the magnetic field can be reduced. The reduction of the plasma density favors the increase of the voltage stand-off.

The RF breakdown occurs during the injection of ELMs - very unstable, intermittent events (see below section 5.3.7). Each ELM is unique and introduces a high degree of uncertainty. Therefore it is still unclear whether the effect of the change of voltage limit is assigned to some changes of the fluxes during single ELMs that may provoke the breakdown or the voltage limit changes as a result of a change in total number of charged particles collected by the surface of the probe during the power ramp.

5.3.7 Measurements by the probe during ELMs at voltages below the limits

Measurements for voltages below the limits are discussed in this section to have a more detailed knowledge about the operation of the RF systems during ELMs.

Influence of ELMs on the Q-factor

One of the further confirmations of the fact that not only the RF voltage is critical for the breakdown on the probe is found in Fig. 5.18a. The dependence of the Q-factor averaged for 200 μs during ELMs on the RF voltage between ELMs is shown in the figure. We see that the Q-factor tends to increase with the voltage.

Fig. 5.18b shows dependence of the power coupled to the plasma (calculated according to equation (4.4)) versus the net power (the difference between the forward power and the reflected power). The dashed lines correspond to the absolute level of the coupled power. The solid lines are the coupled power normalized to the net power.

At a power higher than 150 kW the absolute coupled power depends on the net power non-linearly for the majority of pulses. The normalized coupled power is decreased when the RF voltage is increased. This means that the effective RF resistance of the load (the open end of the probe) is a function of the RF voltage. The power does not fit the quadratic law (1.11) (as for some experiments in the test facility, section 5.1.6). Therefore there should be a non-linear mechanism responsible for the dependence of the load resistance on voltage.

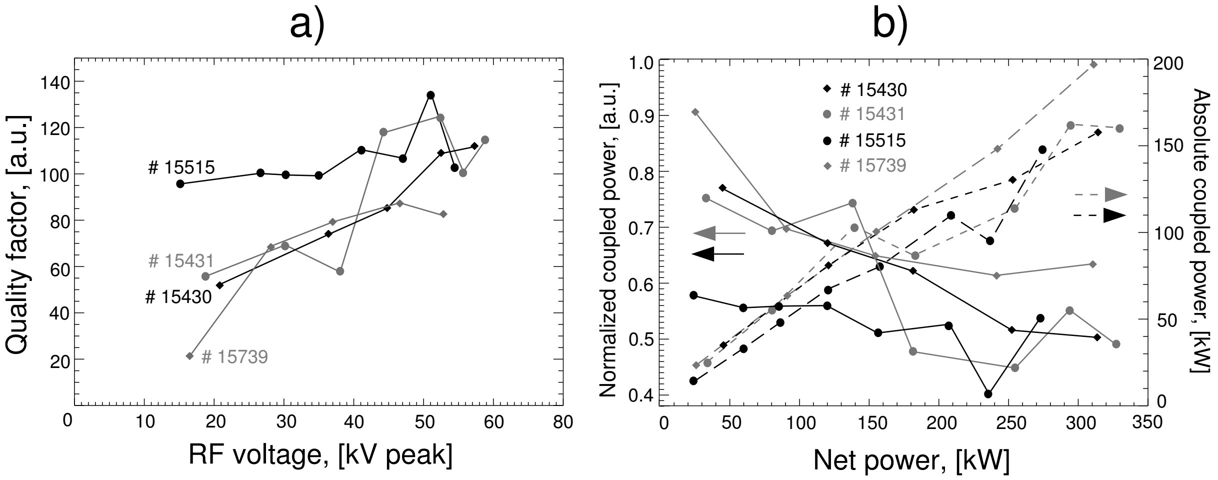

Figure 5.18: *a) Minimal value of time-averaged quality factor during ELMs versus RF voltage on the probe between ELMs; b) the coupled power versus the net power, the solid lines – the coupled power normalized to the net power, the dashed lines – the absolute coupled power.*

The increase of the Q-factor (and the decrease of the normalized coupled power) with voltage can be explained as a consequence of the following effects:

1. The power coupled to the plasma may include a certain fraction corresponding to the power launched by the waves. The power can have a non-linear relation to the RF voltage since a variety of wave modes can be launched by the probe (including waves that can be under some conditions transformed into the non-linear ion Bernstein mode in front of the probe [109, 110]).

2. The RF probe reduces the particle flux during a part of the ELM phase at high RF voltages as described in section 3.3.3 for the case of the thick sheath.

Clarification of the role of the excited waves that propagate from the probe inside the torus chamber and an associated change in the RF resistance of the open end requires taking into account the variety of the wave types that can be excited by the probes. Theoretical treatment is not considered in the frameworks of this thesis. The experimental observations on the propagation of the waves are briefly discussed below in section 5.4.

The effect of the density reduction described in sections 3.3.3 and 3.3.4 gives a consistent explanation of the picture of the coupled power presented in Fig. 5.18. Both the regime of the thin sheath and the regime of the sheath thickness comparable with the electrode gap take place during ELMs. The regimes are present during the ELM due to the intermittent character of the radial transport of plasma during this phase. The thick sheath regime will lead to a reduction of the charged particle fluxes towards electrodes and a decrease of the power fraction which is dissipated locally.

Thus the change of the Q-factor can be related to the mechanisms of the local power dissipation, i.e. the interaction of charged particles with the RF fields and electrodes of the probe.

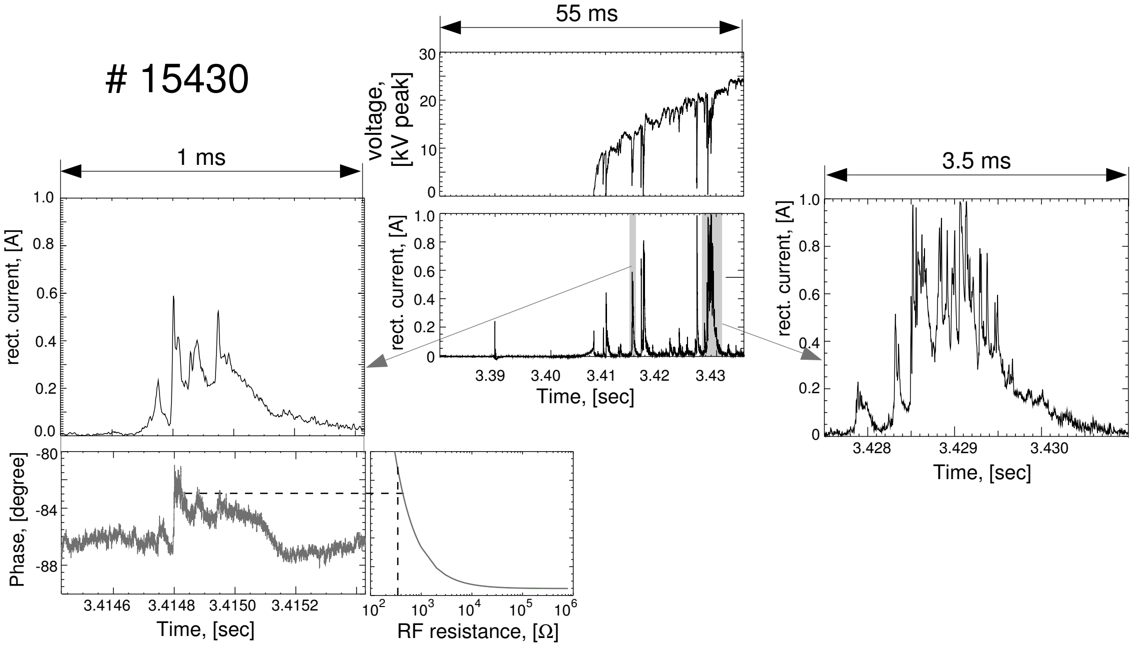

Figure 5.19: *ICRF probe reaction on ELM: plasma density bursts.*

Time resolved picture of the probe reaction to ELMs

Fig. 5.19 shows a typical reaction of the ICRF probe to the type I ELMs on the example of two ELMs (left and right sides of the figure) during a power ramp (center of the figure).

Measurements of the rectified current and phase (left side of Fig. 5.19) were taken for a single event identified from D_α and magnetic measurements (not shown in the figure) as a "small" type I ELM . The "small" ELM appears prior to a normal type I ELM. The rectified current as well as the phase during the small ELM shows a burst-like behavior. The rectified current reaches 0.6 A while the phase measurements correspond to a rather low RF resistance of the open end of $\approx 350\ \Omega$ when the model for the phase from section 4.4.1 is used.

The right side of Fig. 5.19 shows a time-resolved measurement of the rectified current during a normal type I ELM. The bursty behavior of the rectified current indicates the bursty nature of the plasma density injected radially towards the probe head. Compared to the measurements from the left side of the figure, the number of bursts is increased and their amplitude increased to about 1 A. The phase measurements were also conducted for a typical standalone type I ELM but are not shown in the figure since these are very similar to the measurements presented in the left side of Fig. 5.19. However the measurements during type I ELMs are often characterized by a somewhat smaller modeled RF resistance though the value of the resistance is typically above $\approx 200\ \Omega$ for single bursts.

The measurements confirm that the plasma density in front of the RF probe has the intermittent character during ELMs.

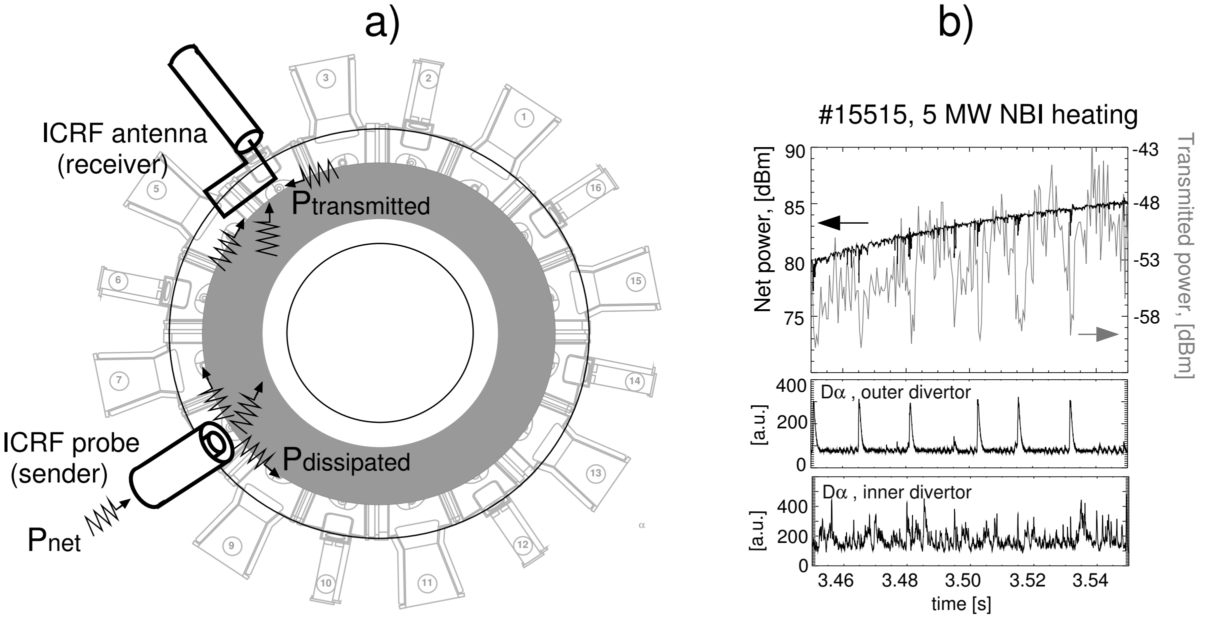

Figure 5.20: *a) Scheme of the measurements of the coupled and the transmitted power; b) measurements of the power transmitted from the ICRF probe to AUG ICRF antenna.*

5.4 RF power coupling/transmission by plasma in AUG

The probe is actually an antenna that has no current carrying straps, but a high RF voltage electrode. For propagation of waves in plasma in external magnetic field the orientation of the electric field with respect to the magnetic field is important. Because of the coaxial geometry, electric field of the probe has high and equal parallel and perpendicular electric field components in the poloidal plane. A high radial electric field is also present. The broad variation of electric field orientation with respect to the external magnetic field allows for the existence of many wave modes that can in principle carry power away from the RF probe operating at $\omega_0 \sim 4\omega_{ci}$ and propagate inside the toroidal chamber of the fusion device (see, for example, [110]).

Coupling of the wave modes to the plasma is strongly dependent on the plasma density near the antenna. From the previous sections we know that ELMs lead to very fast changes of plasma density in front of the antenna. The power from the RF probe may be carried by a wave which propagates inside the scrape-off-layer or by a wave propagating through the core plasma.

In Fig. 5.20a the scheme of measurements of the coupled power and the power transmitted from the ICRF probe to the ICRF antenna functioning as a pick-up probe is shown. The ICRF antenna is screened by a Faraday screen, hence this pick-up probe is sensitive mostly to the electrical field perpendicular to the magnetic field. Therefore contribution of the power carried by slow waves is reduced at the side of the RF receiver. RF trans-

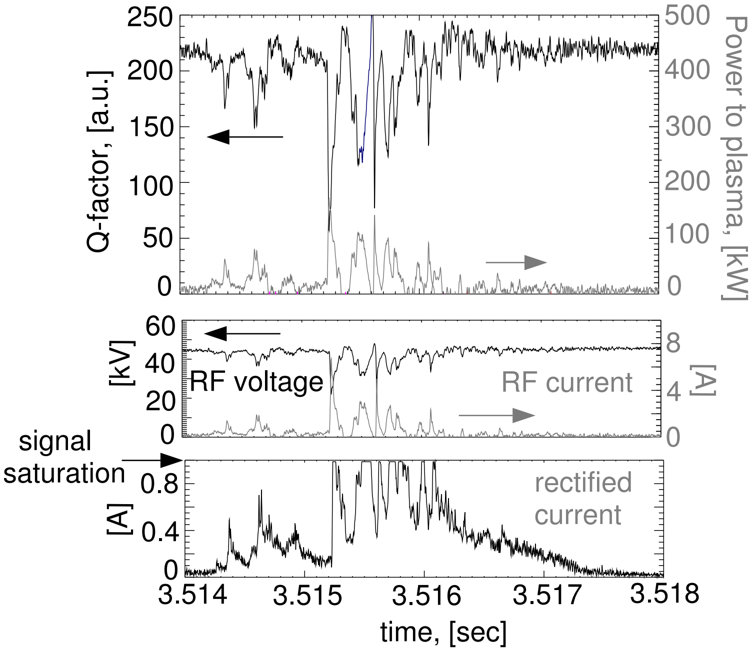

Figure 5.21: *The coupled power measurements, AUG shot #15515 (see also Fig. 5.20).*

mission signal above a noise level of -60 dBm (about the detectable power threshold) can be detected by a frequency analyzer with a time resolution of 500 μs.

Transmission measurements in vacuum

A finite transmitted power in vacuum without magnetic field and plasma was measured. A time-averaged level of the transmitted power is below -60 dBm for a net power level of 80 dBm (100 kW) and is about -56 dBm for a net power level of 85 dBm (≈316 kW). The transmitted power measured in vacuum has a scattering of about 2 dBm.

Measurements in AUG H-mode discharge

The transmitted power during the net power ramp in plasma is presented in Fig. 5.20b on the dBm (logarithmic) scale together with the net power for an AUG plasma discharge (#15515). The signals of D_α radiation from the inner and outer divertors are also shown for the shot.

At the net power level of 85 dBm, the time-averaged transmitted power is increased from -56 dBm without the plasma to about -48 dBm with the plasma between ELMs. This increase of more than one order of magnitude in the power received by the antenna proves that the waves are launched and transmitted through the plasma (the central plasma or the edge plasma).

One observes a strong decrease in the transmitted power (practically down to the noise level of -60 dBm) during ELMs in Fig. 5.20b. The decrease can not be explained by a mismatch during ELMs. Indeed the net power signal, which is on the same relative scale in Fig. 5.20b as the transmitted power, only decreases by ≈3 dB (by a factor of ≈2). However, the relevant power, which is the absolute power coupled to the plasma, as we will see below, actually increases. A mismatch of the directional coupler of the ICRF antenna used as the receiving probe can also be ruled out. Between the ELMs one observes a scattering of the value of the transmitted power by more than 10 dBm. This is larger than the scattering of the power in vacuum (2 dBm). Thus the transmitted power is very sensitive not only to the ELMs but to any changes at the edge plasma, which can be qualitatively observed on the D_α signal from the inner divertor tile.

In Fig. 5.21 the Q-factor, the coupled power calculated according to (4.4), the RF voltage, the RF current and the rectified current are shown during the ELM phase. The figure shows a strong increase of the coupled power of up to 200 kW during an ELM. The power increase is confirmed by changes of the RF voltage and of the RF current as well as by an increase of the rectified current.

The measured reduction of the transmitted power, despite the increase of the coupled power, indicate that a larger fraction of the power is absorbed during ELMs between the sender (ICRF probe) and the receiver (ICRF antenna). This absorption can occur either at the plasma edge or in the plasma center.

Two hypothesis can explain this reduction of the transmitted power:

1. Most of the power is transmitted through the edge and the absorption in the edge changes (increases during ELMs).
2. Only a fraction of the transmitted power comes through the edge and another through the center. If now the change of the edge parameters (during ELMs) increases the fraction of the power traveling through the center (where it can be efficiently absorbed), then a reduction of the transmitted power can occur even without an increase in absorption of the power in the edge.

A drastic increase of the rectified current during ELMs supports rather the first hypothesis: the power dissipated in the edge is increased. Furthermore this increase of the rectified current indicates that the power is absorbed locally, near the head of the ICRF probe. A rough estimation of the local power absorption at the plasma boundary can be made. We assume that the RF current carried by charged particles is of the order of the rectified current, i.e. we neglect the secondary electron emission effects (section 2.6.5) and the rectified current component due the asymmetry of the surfaces not nearly parallel to the magnetic field (sections 3.3.2 and 3.3.3). We assume also that ions are accelerated to energies of the order of eV_0. An estimation for a maximum value of the power dissipated locally in a time window from 3.514 to 3.515 seconds from Fig. 5.21 results in a value of $\simeq$ 30 kW. The measured maximal coupled power in this time window is $\simeq$ 80 kW. Thus the estimation confirms that a significant fraction of the absorbed power is dissipated locally, though we cannot make a conclusion that the power does not dissipate in the central plasma.

The hypothesis of the local power dissipation fits also well to the measurements presented in section 5.3.7 where the coupled power normalized to the net power was found to be affected by the high RF voltage on the probe.

5.5 Conclusions from the ICRF probe experiment in ASDEX Upgrade

It was found that the inner conductor of the ICRF probe collects a time averaged ion current when an RF voltage is applied to it. This result stresses the role of the surfaces oriented at small angles with respect to the external magnetic field as ion collection surfaces (see also [73]). The net rectified current follows transient changes of the plasma density in the limiter shadow that is to a large extent sustained by an intermittent transport associated with the dense plasma formations injected radially towards the probe head.

During type I ELMs the injected plasma formations often lead to a RF breakdown: a transition of the high resistance load of the open end of the probe to the low resistance load typical for arcing and accompanied by a drastic increase in the power reflected back to the RF generator. The explanation of the breakdown may rely on the description in sections 3.3.2 and 3.3.4 – the amplification of the electric field on the surface of the electrodes under the conditions for the thin sheath in the electrode gap.

Experiments with DC biasing show that the RF voltage limit can be affected and correlates with a change in the time-averaged rectified current between ELMs. A decrease of the rectified current correlates with an increase of the voltage limit. Since the time-averaged rectified current is a measure of the plasma density injected radially, the increase of the voltage limit can be assigned to a decrease of the plasma density in a region of the probe head.

Measurements of the Q-factor during ELMs show that the coupled power normalized to the net power decreases when RF voltage applied to the probe is increased. The most probable mechanism which favors this change in Q is a reduction of the plasma density when the applied voltage is so high that the sheath thickness is comparable with the interelectrode distance.

When the power transmitted away from the ICRF probe is registered by means of the ICRF antenna functioning as a RF pick-up probe, a decrease in the transmitted power by almost 20 dB (two orders of magnitude) is observed during ELMs. In addition the transmitted power is very sensitive to the changes of the edge plasma. High values of the coupled power and rectified current during ELMs and other intermittent events show that the power is efficiently absorbed by the plasma and the power transmitted to the pick-up antenna is almost zero. A simple estimation shows that a significant fraction of the power can be absorbed locally at the plasma boundary.

5.6 High voltage operation of the ASDEX Upgrade ICRF antenna

In parallel to the experiments with the ICRF probe, the ICRF antennas of ASDEX Upgrade were studied. AUG ICRF antenna and the ICRF probe are different RF systems and the specific properties of each should be taken into account when the RF breakdown is discussed. At first let us summarize the differences.

5.6.1 Comparison of the ICRF antenna and the RF probe

Different voltages facing the SOL

As the antenna strap length is comparable to a quarter of the vacuum wavelength, the RF voltage on the ICRF antenna varies along the strap. The voltage is zero at the position of the short circuit in the AUG antenna - the most distant position from the RF generator. The voltage increases along the antenna strap to a maximal value at the position corresponding to about $\lambda/4$ from the short circuit. The strap is positioned in poloidal direction, therefore the whole range of voltages from zero to the maximal value is present at approximately the same radial position close to the SOL plasma.

In the ICRF probe only one RF voltage value instantaneously is exposed to the SOL plasma. The voltage changes according to the standing wave pattern radially away from the plasma.

Differences in coupled power and voltage sensitivity

The ICRF antenna is designed and operated such as to deliver as much power as possible to the plasma. A coupling resistance $R_0 = 2\ \Omega$ determines a Q factor of $Q_{ant} = 12.5$. For this Q-factor a voltage of $V_{ant} = 25$ kV on the antenna strap corresponds to a power of $P_{ant} = 2$ MW (see Fig. 5.4). On the other hand in vacuum the Q-factor is high ($Q_{ant}^{vac} \approx 200$). Therefore, according to equation (4.4) most part of the input power is transferred to the plasma.

The probe aims to expose high voltages for a relatively low input power. Therefore it the has high Q for operation with and without plasma. The value without load $Q_{probe}^{vac} = 230$ (see section 4.1) is close to Q of the antenna operated in vacuum. Experiments described in section 5.3.7 showed that the Q-factor of the ICRF probe during operation with the plasma stays close to 200 and is down to the values of 20-100 during ELMs. This is considerably higher than Q_{ant}.

The relative change of the RF voltage on the probe or antenna during fast changes of the load (e.g. caused by ELMs) may be critical in terms of comparison of the breakdown evolution in the RF systems. The relative change of the voltage can be represented as:

$$\delta V = \sqrt{\frac{Z_0}{2}}\left[\sqrt{\frac{P_{net}}{Q}}\,\delta Q + \sqrt{\frac{Q}{P_{net}}}\,\delta P_{net}\right] \tag{5.8}$$

The change in voltage is associated with the change in the Q-factor δQ (first term) and the mismatch in terms of the net power δP_{net} (second term). Generally δP_{net} is a function of the resonant line parameters (the absolute Q value), a change of the load impedance, matching position and matching circuit characteristics. The value of δQ is only dependent on the change of the load. One can use experimental data to test the validity of the last expression.

Let us estimate a difference in δV for a voltage of V=25 kV and changes δP_{net} and δQ during the type I ELMs (which do not trigger arcing) in the same discharge, for the radial position of the ICRF probe close to that of the antenna.

For the ICRF probe: $Q \approx 200$, $P_{net} = 200$ kW, $\delta P_{net} \approx 100$ kW, $\delta Q \approx 100$.

For the ICRF antenna: $Q \approx 12$, $P_{net} = 1500$ kW, $\delta P_{net} \approx 400$ kW, $\delta Q \approx 5$.

As a result one gets a relative change of the voltage on the probe 2.1 times higher than on the antenna. The difference in δV between the probe and the antenna is confirmed by the voltage measurements. The ratio $\delta V_{probe}/\delta V_{antenna}$ normally lies in the range 1.5-4 for high voltages depending on the discharge parameters.

For the EOC plasma shape the voltage on the probe during ELMs can drop from 50 kV to about 25 kV, while on the antenna the voltage decreases from about 23 kV (for the case of P_{net} $\approx$1.8 MW per antenna) to 15 kV.

Therefore, during ELMs, the ICRF probe may operate at higher voltages than the AUG ICRF antennas. The Q-factor of the probe is high during ELMs (as shown in Fig. 5.18, section 5.3.7, Q grows with the RF voltage) compared to Q of the antenna (Q_{ant} tends to 1 due to the transiently increased R_0). This explains the relatively high RF voltage on the probe during ELMs though the mismatch $\delta P_{net}/P_{net}$ of the probe can be large compared to the mismatch of the antenna.

We conclude that at high RF voltages on the probe between ELMs (>50 kV), the RF voltage on the probe is higher than 20 kV during type I ELMs. If an RF breakdown correlates with type I ELMs, the breakdown processes initiated at this RF voltage are similar to those on the ICRF antenna which operates near its voltage limits (25 kV between ELMs and 15 kV during ELMs) under the same plasma conditions.

Different concepts of matching and arc detection

The connection of the AUG ICRF heating antennas to the generators is shown schematically in Fig. 5.22a.

Two antennas are connected to two generators by 3 dB hybrid couplers (combiner and splitter in Fig. 5.22a) which allow for a significant reduction of the reflected power at the generators if both antennas are similarly mismatched. The reduction only works if the reflection coefficients at the points of the matching circuit (described below) connection are approximately equal. Thus the reflected power at the generators is a measure of asymmetry in mismatching between the two antennas. The hybrid couplers avoid the influence of fast changing loads of the antennas on the generators. For example, ELMs which do not trigger arcing cause approximately symmetric mismatching in two antennas but do not lead to a strong increase of the reflected power at the generator. Therefore the system of ICRF antennas at AUG is ELM-tolerant, though mismatch during ELMs

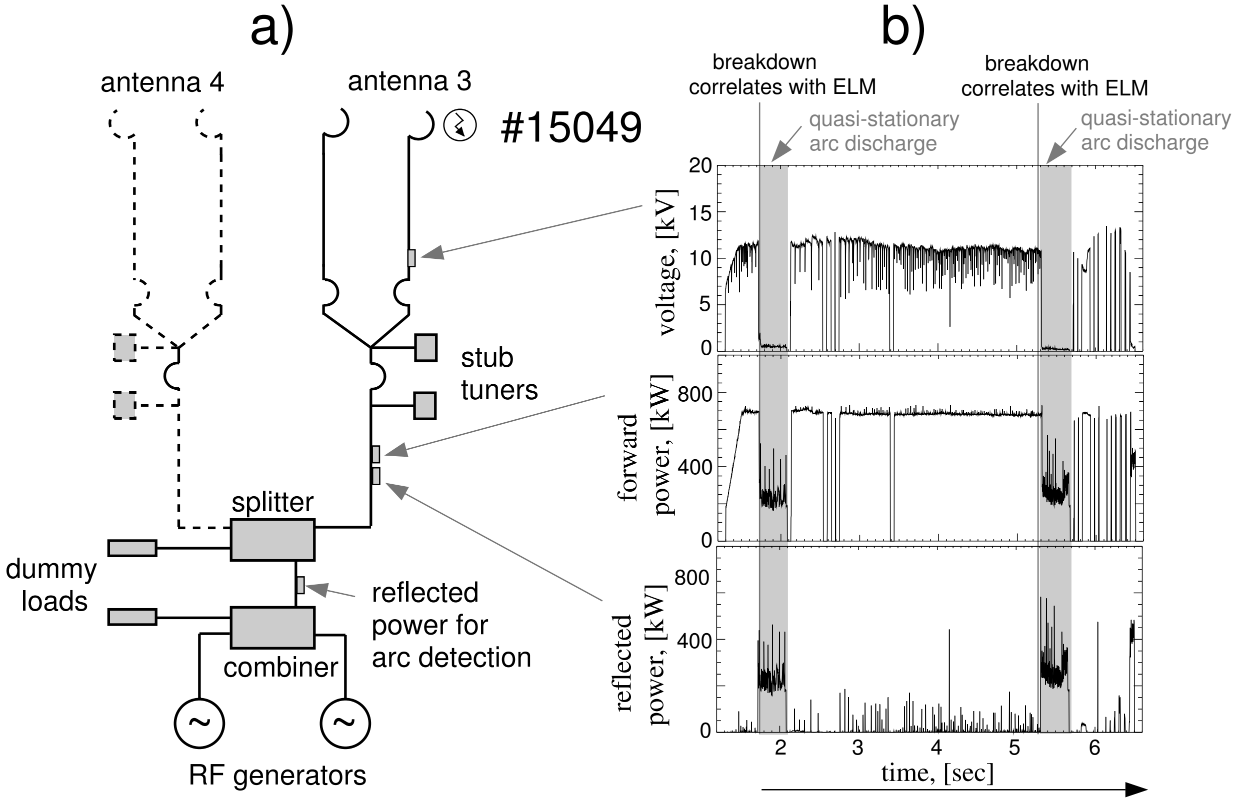

Figure 5.22: *a) Scheme of the ICRF system of two antennas at AUG, b) time traces od RF voltage, forward and reflected power for a shot with breakdown associated with ELMs.*

leads to a decrease of the power delivered to plasma during ELMs.

The ICRF antenna has two straps corresponding to two resonant lines. The power from the RF generators is divided between these two lines at about $9\lambda/4$ (30 MHz) from the antenna straps. Two stub tuners are connected in parallel to the power transmission line and constitute the matching circuit. The ICRF probe has only one stub tuner. The number of connected parallel circuits to the resonant line between the load and the feeding point of the antenna system introduces a big uncertainty in detection and localization of arcing.

Both the ICRF antenna and the RF probe detect the RF breakdown from an increase of the reflected power in the matched circuit. Because of its bad coupling of power to plasma, the ICRF probe allows for a reliable detection of arcs by the reflected power signal. The situation with the ICRF antennas is different. For the 2001/2002 experimental campaign, breakdown in ICRF antenna was detected from the signal of the reflected power measured between the hybrid power coupler and splitter (see Fig. 5.22a). The signal shows a differences in loads of two antennas. This signal is used for arc detection because of the difficulties in distinguishing between ELMs and arcs on the antennas with the complicated parallel connections described above. While ELMs are global events and the difference in loads between two antennas is rather small, arc usually appears on a single antenna and should lead to an asymmetry of the loads and substantial increase of the measured reflected power. However two antennas are not quite equal and one needs to regulate the critical level of the measured signal to be sure it is due to an arc, but not to the ELMs that do not trigger an arc.

5.6.2 Breakdown types

Three breakdown types are observed on the ICRF antenna:

1. vacuum arc breakdown which happens at the location of the voltage maximum on the strap and does not correlate with a plasma activity;

2. breakdown at the voltage maximum of the strap triggered by ELM, detected as a sharp increase of the reflected power (close to the total reflection);

3. breakdown at the location of the strap at a certain distance from location of the voltage maximum, triggered by ELM, poorly detected by the arc detection system and leading to a quasi-stationary (from 100 μs to 1 s duration) arc discharge.

The type (1) and type (2) breakdown have about the same scales and characteristics as vacuum arc and ELM-correlated breakdown on the ICRF probe respectively. The type (1) is the same breakdown as in vacuum without the plasma. The type (2) breakdown is a RF breakdown caused by a drastic increase of the surface electric field during the increase of the plasma density in the gap between the antenna strap and the antenna box.

The type (3) breakdown is followed by a quasi-stationary arc discharge. Appearance of the latter on the antenna is shown in Fig. 5.22a by the gray vertical lines. Our understanding of this phenomena is the following. The breakdown is associated with the ignition of an arc at a location far from the voltage maximum since the reflected power is increased to the values lower than the typical values for the type (1) and type (2) breakdowns. Ionization of the desorbed gas by the external plasma injection during ELMs leads to formation of the semi-self-sustained discharge (see sections 2.7.4 and 5.1.6). The latter increases the power absorption (it is a quite non-local effect) which is poorly detected by the arc detection and a consequent glow-to-arc transition happens at the location not necessarily coinciding with location of the voltage maximum. The sequence of the events may be "transparent" for the arc detection system used and described in the previous section.

The arc discharge phases which follow type (3) breakdown are shown by the gray regions in Fig. 5.22a. If the breakdown is not detected at the right time, an arc discharge occurs which leads to a reduced voltage stand-off of the system. Repeated breakdowns of type (1) which are detected (the power is switched off often, Fig. 5.22a) follow the quasi-stationary arc discharge. These breakdowns seem to recondition the system. A good detection of the ELM-correlated breakdowns is critical since the overall performance of the RF antennas is affected by the significantly reduced voltage stand-off after ignition of these quasi-stationary arc discharges. The conditioning of the antenna conductors and transmission lines required after the ignition of the arcs can be partly performed in vacuum operation.

The ignition of the arc discharges after ELMs is less frequent when the antennas are well-conditioned. However even few arc discharges may lead to damage of the electrodes which may set permanent voltage limits of the system lower both for vacuum and plasma operation.

It is important to understand the movement of the cathode spots of the quasi-stationary sustained arc discharge. Motion of the cathode spots sustained by RF power should be treated differently from the motion of spots constituting a DC arc.

5.6.3 Arc self-screening

It is known from optical observations that if the RF generator is not switched off after the arc ignition, the arc moves [2] along the strap towards the generator. This movement can be understood from a simple model shown in Fig. 5.23 and some knowledge on the arc structure [111, 112].

An arc is a conductive channel where the current is transported by the charged particles produced by combined thermal-field emission of electrons and ionization of vapors of the electrode material. The arc has some impedance Z_{arc} (see Fig. 5.23) that has a low resistive part and an inductive reactive part. The current channel is associated with the formation of a cathode spot. The cathode spot has a structure containing multiple discrete elements [111] which in turn are often observed to have a discrete structure [112]. The structure of the spot depends on the surface material and surface properties (e.g. contamination etc.). The discrete elements are sometimes called fragments, cells or spots of different (I, II, III) type. A surface can have certain features in terms of the cathode spot structures. The common thing for any surface is that the integral arc current is carried by small channels. Let us further call them spots for simplicity. One such a spot has an average impedance Z_{spot}.

During the development and existence of the arc, the spots are born, disappear and respawn constantly. With respect to the connection of an equivalent Z_{arc} (a center of the spot group), new spots appear both to the side of the RF generator and to the side of the antenna short circuit (respectively left and right directions in Fig. 5.23). The four stages of the arc evolution are also shown in Fig. 5.23:

1. single cathode spot ignition (onset of the spark stage);
2. ignition of the two equivalent other spots to the different sides of the initial spot;
3. the right spot is screened by the left ones and disappears because the power is dissipated on the left side or is reflected back to the generator before it reaches the right spot;
4. the effective movement of the arc towards the RF generator.

---

[2] We mean the movement of the cathode spots and consequently the movement of the arc discharge.

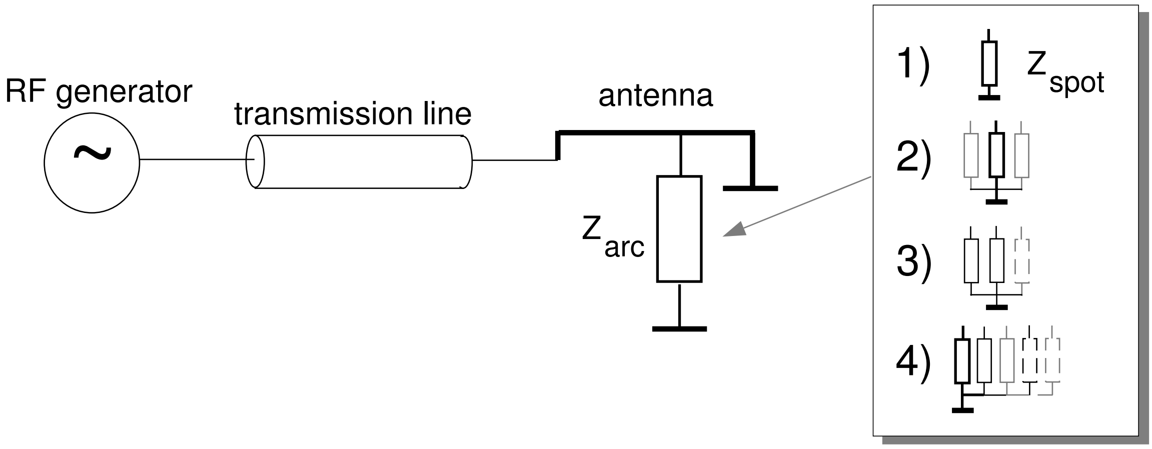

Figure 5.23: *Explanation of the arc self-screening, different stages of the arc evolution.*

The total power which the external circuit can deliver sets the number of spots. The spots appear and disappear constantly and predominantly the spots to the generator side survive, so we see the movement of the arc towards the generator.

5.6.4 Arcs tied to electrodes

The self screening of the arc described in the previous section is not the only mechanism which influences the arc motion. Observed arc tracks show that arc may stop at certain electrode locations, i.e. may become tied to the electrodes. This happens probably due to the counteraction of a few arc movement mechanisms. The arc stopping leads to severe damage of the electrodes and to a significant reduction of the voltage stand-off.

In-situ video observations of the ICRF antenna on ASDEX Upgrade and experiments on other machines (e.g. [115]) confirm that the arc is ignited along the magnetic field lines. An arc is excited between the strap and antenna box. Locations of the arcing tied to the electrodes were observed on the antennas. In particular, the regions of the electrodes where the straps are connected to the coaxial lines are damaged by repetitive, quasi-stationary, local arcing.

A fully developed RF arc may exist on both electrodes, because the spots on one electrode can be powered during half of RF period (see section 2.5.3). The RF period is short compared to the density decay time of the arc plasma which is defined by the typical ion time $t_{ion} = 2\pi/\omega_{pi}^{metal}$, where ω_{pi}^{metal} is ion plasma frequency for the arc plasma of the heavy ions of the electrode material. In such model of a RF sustained arc, current of the arc is a purely RF currrent. However the capability of the dense arc plasma to rectify the current (described in the chapter 3) should not be excluded. The current of the RF sustained arc may include a DC fraction.

In addition to the arc self-screening, one can consider at least three factors which can affect the arc motion:

- *geometry*: arc often tends to be sustained in an electrode gap with a minimal interelectrode distance;

- *sustaining of arc in magnetic field*: in a strong external magnetic field the arc tends to have the current column aligned parallel to the magnetic field;
- *movement in magnetic field*: in the external magnetic field an arc can move in a direction perpendicular to the field and to the arc current.

The last point requires a separate discussion. Even for a DC sustained arc the picture of the arc motion in a transverse magnetic field is not well understood. The motion can change the direction from the retrograde[3] [112, 113] to the amperian [113] when, e.g. the magnetic field is increased for a given interelectrode distance and a given neutral pressure (we consider a low-pressure arc). For example, in the experiments [113] the critical magnetic field for the reversion of the arc motion was found to be about 1 Tesla. If the magnetic field has an acute angle to the surface, the arc velocity can sometimes also have a component in the direction of the angle. Sometimes the movement associated with this velocity component is called *Robson drift* [114].

For an arc sustained by the RF power one can initially consider both the RF and the DC components of the arc current when the arc motion in the magnetic field is discussed. However, if we use the results of the experiments (e.g. [111, 112, 113]), the maximal velocities (perpendicular to the magnetic field) a DC arc can have, are of the order of 100 m/sec. If we take the values of the velocity from these DC measurements for an arc with a pure RF current, then the arc does not move to a distance larger than the width of the current channel in half of a RF period. Therefore if a mechanism of the RF arc motion is assumed to be similar to that of the DC arc motion, one should consider the DC component of the arc current as the first candidate which can explain the motion.

A counteraction of the properties of the arc motion described in the list above and the self-screening effect described in the previous section, can lead to an arc tied to the particular regions of the electrodes due to, for example, a specific geometry of the conductors and/or due to a specific distribution of the magnetic field.

In addition to the poorly understood picture of the currents in a RF sustained arc, other factors, such as complex geometry, uncertain finite ferromagnetic properties of the stainless steel electrodes (even more so in the regions of welding of the coaxial tube to the plate of the antenna return conductor) make the interpretation of the arc tracks observed in the antennas an outstanding issue.

---

[3] The term "retrograde" is applied to the arc motion in a direction opposite to the amperian (parallel to $(\boldsymbol{j} \times \boldsymbol{B})$) direction.

5.7 Conclusions from studies of RF breakdown on AUG ICRF antennas

Operation of the ASDEX Upgrade ICRF antennas demonstrates that the maximal RF voltage on the antenna straps is often limited by the plasma. The breakdown often correlates with ELMs. Despite some technical differences between the the ICRF antenna and the ICRF probe, the observed picture is very similar to that observed during the probe operation in type I ELM plasmas. However the breakdown on the antenna provoked by ELMs is not always detected properly by the arc detection system. This is partly connected to the fact that the breakdown correlated with type I ELMs does not necessarily occur at the location of the voltage maximum in the antenna. If the breakdown is not detected in time, a possibility exists for an arc discharge to produce a significant damage of the electrodes. This degrades the performance of the ICRF antennas because of a decrease of the voltage stand-off. However the number of the breakdowns which are poorly detected is decreased with conditioning in plasma.

A first step to understanding of the arc motion sustained by RF power in the antenna and in the transmission line was made. Severe electrode damage caused by arcs tied to the particular regions of the electrodes were observed.

Chapter 6

Summary and conclusions

6.1 Most important results

Measurements from the ICRF probe in a test facility and on ASDEX Upgrade and observations from the ICRF antennas show that the following breakdown mechanisms are the reason for the reduced voltage stand-off:

- vacuum arc (ICRF probe in the test facility and on AUG, AUG ICRF antenna);
- arc initiated due to a high surface electric field when plasma presence in an electrode gap amplifies external electric field on the surface of the RF electrodes (both for the AUG ICRF antenna and the ICRF probe in AUG during plasma injection which accompanies ELMs);
- semi-self sustained glow discharge with consequent glow to arc transition (ICRF probe in test facility and sometimes in the AUG ICRF antenna during type I ELMs);
- more frequent vacuum arc ignition after electrode damage by preceding quasi-stationary phases of arc discharges (AUG ICRF antenna).

One of the most frequently observed phenomena is the breakdown following the transient change of the plasma parameters in the scrape-off layer of the tokamak, e.g. ELMs. ELMs and more local intermittent events which can be seen by the RF probe are accompanied by the drastic increase of ion flux to the probe. Therefore the plasma density is increased during the events in the electrode gaps of the ICRF probe and ICRF antennas. This leads to amplification of the surface electric field and consequent arcing. For ICRF antenna operation, ELMs can sometimes lead to the formation of a semi-self sustained discharge involving gas ionization. Therefore ELMs serve as a trigger for the self-sustained discharge arc discharge both for the ICRF probe and the ICRF antennas. The arc discharge in AUG ICRF antennas can sometimes be poorly detected and leads to a need of reconditioning of the electrodes.

A high increase of the power coupled to the plasma and a good absorption of this power (the power transmitted from the ICRF probe to the ICRF antenna functioning as a pick-up probe decreases essentially) is observed during the ELM phase. Simple estimation shows that the power can be efficiently absorbed at the plasma edge. Therefore the role of ELMs and intermittent transport in the SOL should be considered when parasitic absorption of RF power coupled to the plasma by the ICRF antennas is studied. The measurements of the averaged Q-factor of the probe during ELMs show that the fraction of coupled energy normalized to the net power is significantly reduced with an increase of the RF voltage. This is a further confirmation that the RF voltage affects the charge particle flux which is essential for a RF breakdown.

The maximal voltage on the ICRF probe in the presence of plasma increases by conditioning the probe with plasma. Despite the intensive conditioning in vacuum, plasma operation is a necessary measure to bring up the voltage limit in the presence of the plasma. The additional mechanisms connected to the presence of plasma and accompanying charge particle fluxes, such as gamma-processes on the electrodes, particle stimulated desorption, and an eventual increase of the electrical fields on the electrode surface, make the operation with plasma very critical if the electrodes are not trained in these conditions. The operation of AUG ICRF antennas becomes also much more reliable when the antennas are well conditioned in the presence of the AUG plasma. The existence of the conditioning effect in plasma stresses the role of the surface state of the electrodes. The surface state has consequences both for vacuum and plasma operation of the probe. The same holds true for the antennas.

It was shown experimentally that the voltage stand-off of the well-conditioned ICRF probe with the plasma presence can be affected by regulating the time-averaged ion flux into the probe.

In parallel to studies related to the voltage limits, measurements of the rectified current and of the power transmission and dissipation provided a better understanding of the interaction of high voltage RF fields with the plasma boundary. The measurements are also a monitor for the transient changes in plasma edge parameters.

6.2 Measures to improve the voltage stand-off of the ICRF antennas

One can formulate a few points to improve the voltage stand-off of the ICRF antenna:

- screening of the antenna from the external plasma: use of an optically closed Faraday shield;

- improving the surface conditions on the antenna electrodes: development of a new conditioning technique using a glow discharge inside the antenna (including a gas puff system);

- regulate particle fluxes to the antenna electrodes facing the plasma: improvement of the geometrical shape of the antenna (more symmetrical electrodes with surfaces intersecting magnetic field at high angles, electrodes of less area intersecting the surface at low angles) and design a DC biased ICRF antenna;

- reduce neutral density in the antenna neighborhood: improvement of the vacuum conditions (pumping) for the ICRF antennas;
- reduce number of arc detection failures: improve the reliability of the RF breakdown detection system.

6.3 Further work

The work made in the frameworks of this thesis raises new questions which should be answered for a better understanding of the phenomena taking place during interaction of the ICRF antenna with the edge plasma. Let us review the more important ones.

It follows from the thesis that surface effects are very important when high voltage RF breakdown is studied. Therefore a proper choice of special materials for the electrodes of the antenna and transmission lines can help in improving the voltage stand-off of the RF components and a reduction of the time required to condition electrodes. This can be done by deposition of specific coatings [86] on the same low-cost stainless steel based electrodes. However for this issue a reliable arc detection system is required since a coating can be removed by a long term sustained-arcing on the electrodes.

A reliable arc detection system is one of the most important issue for improvement of the voltage stand-off as it allows to avoid electrode damages which require a long time for reconditioning. It is also a difficult issue, because the RF breakdown often correlates with ELMs - transient plasma changes.

When RF power is coupled to the plasma, it is not always clear where the power goes. If a dominant absorber exists inside the central plasma (a wave-particle resonance), a big fraction of power can be absorbed at this central location. However there exists always a parasitic absorber at the plasma edge which can be dominant if the conditions for the good absorber in the central plasma are not fulfilled. The parasitic absorption includes the effects of the particle interaction with the electrical fields at the plasma boundary described in the chapter 3. From the experiments with the ICRF probe one observed a drastic increase of the locally absorbed power during intermittent plasma events in the limiter shadow. This may be a hint for a theoretical work that should aim to explain a reduction of the Q-factor in the system "plasma - torus wall". Existing theories are mostly based on the description by surface waves and resonant solutions for RF fields (standing wave patterns) at the interface plasma-wall and do not describe experimental observations consistently. A series of specific experiments is required to make a theoretical modeling easier. The modeling can give some hints for a minimization of the parasitically absorbed power and an understanding of the energy balance between the central and the edge absorption.

A distribution of DC electric field in the neighborhood of the antenna may affect radial transport of charged particles that may result in a higher plasma density near the antenna straps. A big difference exists between the antenna with an open DC circuit and the antenna with a closed DC circuit.

In the first case the equipotential (in terms of time-averaged potential) are the surfaces of the electrodes and the magnetic field lines connected to the electrodes. Furthermore, the time-averaged potential of plasma existing between the surfaces of the antenna strap and the grounded vacuum vessel can be rather low (see table 3.3.2). The strap is charged to a potential which is the result of a trade-off of the charge brought by the sheath rectification (see 3.2) and the ion charge brought perpendicular to the magnetic field (see 5.3.3). Since the strap is equipotential the time-averaged potential exists on any location of the strap.

In the case with the closed DC circuit the plasma between the strap and the vacuum vessel is charged to a relatively high potential. The surfaces which are intersected by magnetic field lines at small angles collect ion current. The plasma is strongly charged locally only due to the local sheath rectification. Therefore the distribution of DC electric field is completely different.

To our knowledge there exists no data about these two configurations working in the similar conditions. The ICRF probe did not allow for experiments with the opened circuit at AUG because of the technical restrictions connected with very high self-bias voltages. However an effort should be made to study effects of DC boundary condition and electrode geometry on plasma convection inside and in front of the ICRF antenna.

Appendix A

Abbreviations

RF	Radio Frequency
DC	Direct Current
ICRF	Ion Cyclotron Range of Frequencies
SOL	Scrape-Off-Layer
ICRH	Ion Cyclotron Resonance Heating
AUG	ASDEX (Axially Symmetric Divertor EXperiment) Upgrade
EOC	Edge Optimized Configuration (describes a type of the plasma shape in AUG)
ELM	Edge Localized Mode
ESD	Electron Stimulated Desorption
ISD	Ion Stimulated Desorption
FFT	Fast Fourier Transform

Appendix B

Solution of a heat conduction equation for the skin-layer of the antenna strap

A heat conduction equation is used to describe the temperature rise on the surface of the antenna strap due to Joule heating by RF currents. Let us assume that the strap surface corresponds to ($x = l$) and a value of ($0 < x < l$) corresponds to a position inside the antenna strap (Fig. B.1). The RF current with peak value I_0 (peak) flows perpendicular to x on the surface of the strap and decays exponentially inside the conductor (when $l - x$ is increased). The heat conduction equation with the volume heat sources is written for temperature T as:

$$\frac{\partial T}{\partial t} = \kappa \, \frac{\partial^2 T}{\partial x^2}, \tag{B.1}$$

where $\kappa = \lambda_T/(\rho_m \cdot c)$, λ_T is specific heat conductivity, c is heat capacitance and ρ_m is the mass density of the strap material. RF current flows in the skin layer δ. If we assume that the skin layer is small ($\delta \ll l$), the heating of the strap can be assumed to be provided by a heat flux to the strap surface:

$$q_0 = \frac{Q_0}{\kappa}, \qquad Q_0 = \frac{I_0^2}{2h^2\delta \; \sigma} \tag{B.2}$$

where δ is the skin layer, σ is the electrical conductivity, h is the strap width. We do not account for losses by a radiation from the surface of the strap nor for the temperature dependence of the electrical conductivity (these two effects partly compensate each other). A boundary condition at the surface ($x = l$) is therefore:

$$\left.\frac{\partial T}{\partial x}\right|_{x=l} = Q_0 \tag{B.3}$$

If the strap has a thickness of $2l$ and is symmetrically heated from both sides, the boundary condition of heat insulation can be applied at the middle of the strap thickness:

$$\left.\frac{\partial T}{\partial x}\right|_{x=0} = 0 \tag{B.4}$$

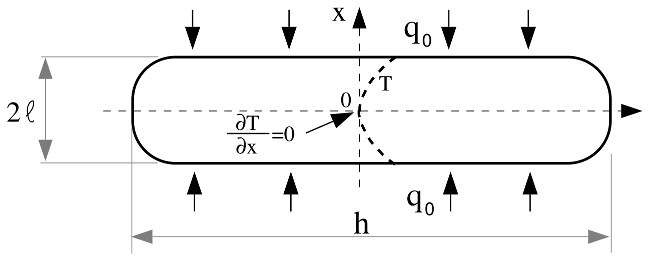

Figure B.1: *Model of a symmetricaly heated antenna strap. Dashed curve - qualitative temperature distribution inside the strap.*

Material	density, ρ_m, kg/m^3	specific heat, c_m, J/kg	specific heat conductivity, λ_T, W/(m·K)	electrical conductivity, σ, $1/(\Omega \cdot m)$
OFC copper	$8.94 \cdot 10^3$	384.9	50.0	$5.85 \cdot 10^7$
stainless steel, AIS 430	$7.7 \cdot 10^3$	460.3	18.0	$1.67 \cdot 10^6$

Table B.1: *Properties of materials used for the calculation of the temperature rise in the antenna strap due to the Joule heating.*

Let us set the temperature T_0 constant across the strap as the initial condition:

$$T(x)\Big|_{t=0} = T_0 \tag{B.5}$$

The equation B.1 with the boundary conditions B.3, B.4 and initial condition B.5 is solved by the method of Laplace transforms [116]. The solution is written:

$$T(x,t) = T_0 + \frac{Q_0\, t}{\rho_m\, c\, l} + \frac{Q_0\, l}{\lambda}\left[\frac{3x^2 - l^2}{6\, l^2} - \frac{2}{\pi^2}\sum_{n=1}^{\infty}\frac{(-1)^n}{n^2} e^{-\kappa n^2 \pi^2 t/l^2} \cos\left(\frac{n\pi\, x}{l}\right)\right] \tag{B.6}$$

Since the real heat source is distributed in the skin later on the surface, the solution B.6 does not reflect the real temperature profile in the surface layer. This is even more important as we are mainly interested in the surface temperature. However the error in the solution is not big and can be estimated.

If one accounts for the volume heat sources instead of using the external flux Q_0 on the surface, the surface temperature should decrease. The estimation of a maximal error can be done assuming a flat temperature profile in the "real" skin layer. In this case the maximal error is:

$$|\Delta T| \approx \frac{1}{\lambda}\left|\frac{\partial T}{\partial x}\Big|_{x=l}\right| \cdot \delta = \frac{Q_0\, \delta}{\lambda_T} = \frac{I_0^2}{h^2\, \sigma\, \lambda_T} \tag{B.7}$$

The maximal error is for the material with the lowest thermal and heat conductivity. For the working parameters I_0=1 kA, h=0.2 m, stainless steel $\Delta T \approx 0.83$ K which can be considered negligible.

The material properties from the table B are used for calculations. The results of the calculation of the surface temperature are presented in chapter 2 for the ICRF antenna and in chapter 4 for the ICRF probe.

Appendix C

Summary of data for collisional and ionization processes

The mean free pass of electron in a gas is defined by:

$$l_{en} = \frac{1}{n_n \ \sigma_{en}} = \frac{kT_n}{p \ \sigma_{en}} \tag{C.1}$$

where σ_{en} – total cross-section of electron-neutral collisions. When the temperature of the gas is assumed to be equal to the temperature of the walls of vacuum vessel which we consider to be 30^0C, the last expression is transformed to the formula:

$$l_e, \ [\mathrm{m}] = \frac{4.18 \cdot 10^{-21}}{p \ \sigma_{en}}, \qquad p \text{ in Pa}, \ \sigma \text{ in m}^{-2}. \tag{C.2}$$

For very low electron energies (ε_e <30 eV) the experimental data for total cross sections of collisions of electrons with neutrals is available [64, 65]. The table C presents the electron mean free pass in gases.

Gas	Ionization potential, V^{ion}, V	mean free pass at V^{ion}, l_e^{max}, m	energy of max. cross section, ε_e^{max}, eV	mean free pass at ε_e^{max}, l_e^{max}, m
$H^{a)}$	13.60	0.095 (at 12 eV)	$\lesssim 1$	0.0183
H_2	15.6	0.063	3.5	0.028
He	24.59	0.182	2.3	0.076
N	14.53	0.077 (at 10 eV)	≈ 7.5	0.059
N_2	15.51	0.038	2.6	0.016
Ar	15.76	0.020	12.3	0.017

Table C.1: *Ionization potentials and mean free pass of electrons colliding with neutrals at 1 Pa at low energies (<30 eV).* $^{a)}$ *- taken from elastic collisions, other - taken from total collision probability.*

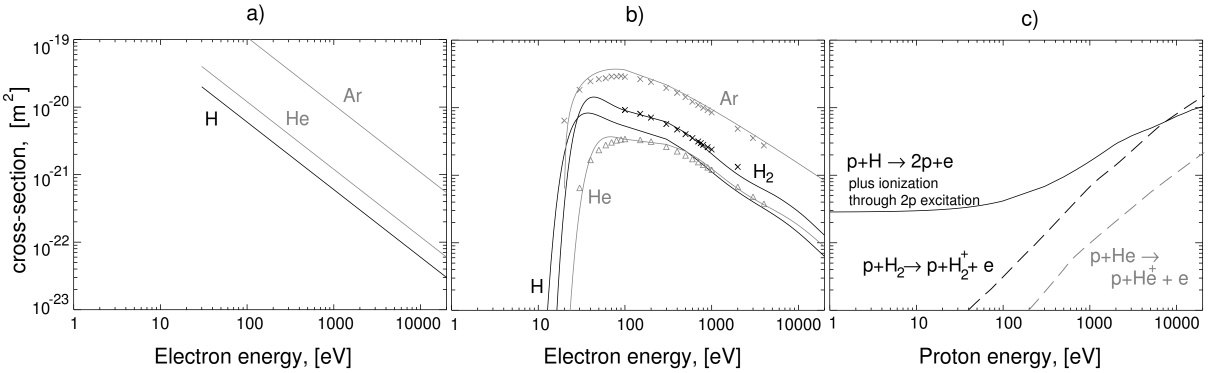

Figure C.1: *Cross sections of charge particle - neutral collisions: a) elastic cross-sections estimated from eq. C.3; b) total electron impact ionization cross-sections, crosses and triangles - averaged experimental data for H_2, He, Ar from [66], curves for H, H_2, He - numerical fit from [118], Ar - from Lotz fitting equation C.4 with $N = 2$; c) proton impact ionization for H, H_2 and He from [118].*

At the low electron energies the total collision cross-section is determined by elastic collisions. For an electron energy ε_e >30 eV one can estimate the cross-section of elastic scattering of electrons on an atom with nuclei charge Z_n by the approximate formula:

$$\sigma_{en},\ [\mathrm{m}^{-2}] \approx 6 \cdot 10^{-19}\ \frac{Z_n^{4/3}}{\varepsilon_e} \tag{C.3}$$

The last equation can be used to estimate elastic collision cross-section for the high electron energy range.

For the estimation of the ionization cross-section of Ar an empirical fitting formula is used [117]:

$$\sigma_{en}^{i} = \sum_{i=1}^{N}\ a_i q_i \frac{\ln(\varepsilon_e/V_i^{ion})}{\varepsilon_e\ V_i^{ion}} \left[1 - b_i\ \exp\Big(- c_i(\varepsilon_e/V_i^{ion} - 1)\Big)\right] \tag{C.4}$$

where i – number of the electron shell counting from the outermost one, a_i, b_i, c_i – tabulated empirical constants from [117], V_i^{ion} – ionization potential, q_i – number of electrons in the (sub)-shell. The last formula gives a reasonable agreement with experimental data and the gases listed in the first column of the table C and energies less than 10 keV. However we use it to extrapolate the cross-section to 20 keV.

Cross sections for elastic collisions estimated by the equation C.3 are shown in Fig C.1a.

Electron impact ionization cross sections are presented in Fig C.1b using the data from [66, 118] and the fitting formula C.4.

Proton impact ionization cross sections from [118] are found in Fig C.1c. In addition to the information on the fugure we note that the cross section of ionization of atomic hydrogen by proton impact has a maximum of $1.5{\cdot}10^{-16}$ m^2 at an energy of 50 keV [119].

Appendix D

Frequency spectra of the ICRF probe signals

Fast Fourier transform (FFT) analysis was performed for two signals: signal of the phase between RF voltage and current, and the rectified current. The analysis allows to look for the frequency spectrum of the signals.

The phase and the rectified current were averaged for the shots #15515, #15538, #15539 for the last 4 ms before the breakdown. Since the breakdown correlates with an ELM, the signals reflect the frequency spectrum of the ICRF probe reaction to the ELM pre-cursors and intermittent events of higher frequency.

The results are presented in Fig. D.1. An amplitude of the FFT analysis for the phase signal is shown in Fig. D.1a. To get a noise level for the phase signal three RF pulses were made in vacuum and the FFT spectrum was averaged. The noise level of the phase deviations is shown by a gray curve in Fig. D.1a. A power spectrum of the rectified current is presented in Fig. D.1b. Both spectra of Fig. D.1 show a flat signal distribution over the range of frequencies presented in the figure. The measurements of the rectified current are limited in speed by the fiber-optics based signal transfer system (see the section 4.3.2) with the 128 kHz bandwidth. Therefore artifacts are observed for the higher frequencies.

A spectrum of the rectified current averaged for shots #15430, #15431 is shown for a wide range of frequencies in Fig. D.2. The frequency range includes also ELM frequencies (150-300) Hz for the discharges.

The observations by the ICRF probe confirm the intermittent character of the radial transport in the scrape-off-layer. Similar frequency characteristics are observed by many diagnostics at the plasma edge of different machines (see discussions in [94, 95, 96, 97, 98, 100, 103]). Therefore the ICRF probe can be used as a tool to monitor the plasma edge activity.

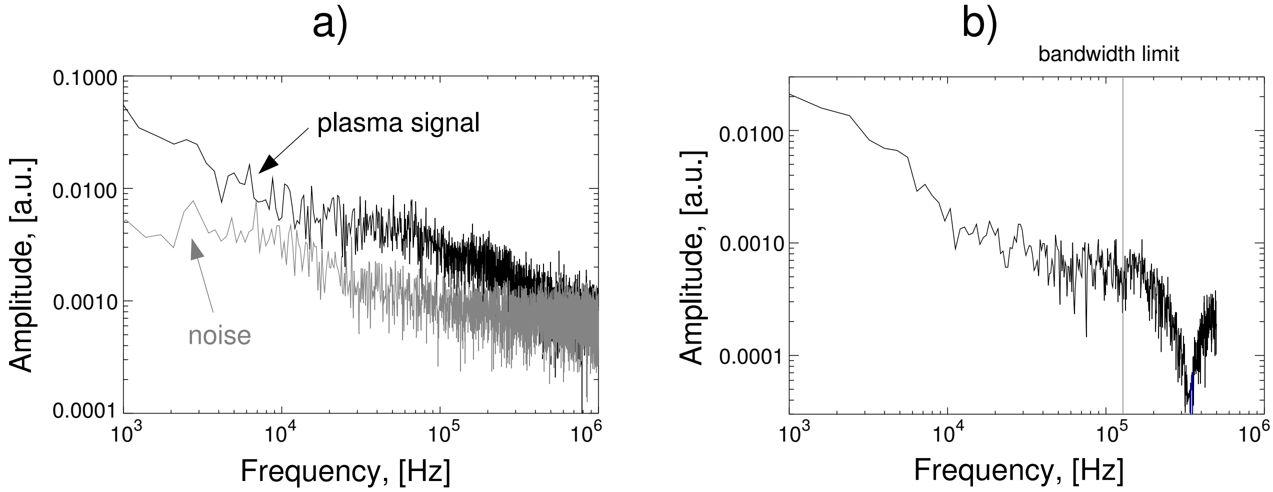

Figure D.1: *Frequency characteristics of the phase signal (a) and the rectified current (b) collected for 4 ms before the breakdown averaged for the shots #15515, #15538, #15539.*

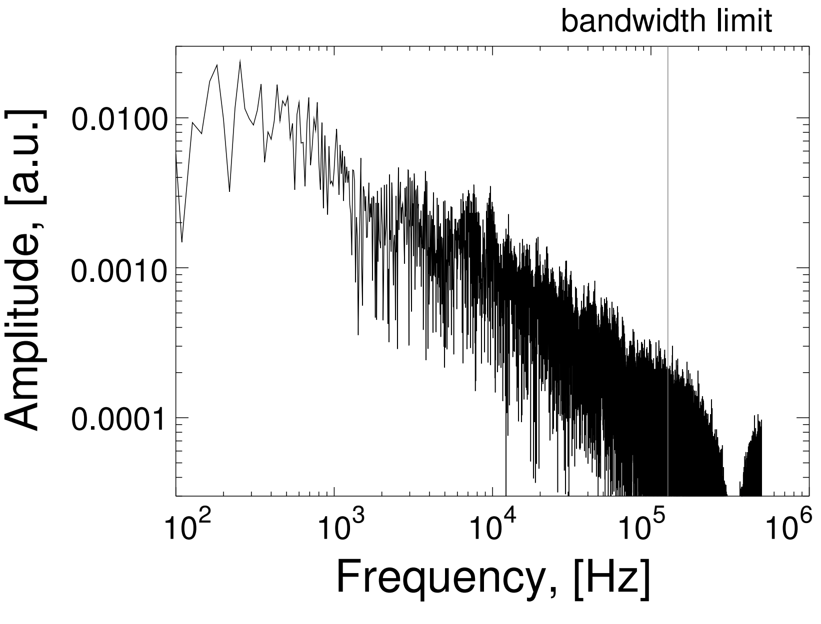

Figure D.2: *Frequency characteristics of the rectified current collected for 110 ms during the power ramp averaged for shots #15430, #15431.*

Bibliography

[1] Lawson J. D., Some criteria for a power producing thermonuclear reactor, *Proc. Phys. Soc.* **B70**, 6-10, 1957.

[2] Dolan T. J., Fusion research, Pergamon Press, New York, 1982.

[3] Wesson J., Tokamaks (second edition), Clarendon Press, Oxford, 1997.

[4] *http://fusedweb.pppl.gov*

[5] Rosen M. D. The physics issues that determine inertial confinement fusion target gain and driver requirements: A tutorial, *Phys. Plasmas* **6** (5), 1690-1699.

[6] Lindl J., Development of the indirect-drive approach to inertial confinement fusion and the target physics basis for ignition and gain, *Phys. Plasmas* **2** (11), 3933, 1995.

[7] Artsimovich L. A., Tokamak devices, *Nucl. Fusion* **12**, 215-252, 1972.

[8] Spitzer L., The stellarator concept, *Phys. Fluids* **1**, 253-264, 1958.

[9] Volkov E. D., Suprunenko V. A., Shishkin A.A., Stellarator, Naukova Dumka, Kiev, 1983, in Russian.

[10] Greenwald M. et. al., A new look at density limits in tokamaks, *Nucl. Fusion* **28** (12), 2188-2207, 1988.

[11] Greenwald M., Density limits in toroidal plasmas, *Plasma Phys. Control. Fusion* **44**, R27-R80, 2002.

[12] Jacquinot J., and the JET Team, Deuterium-tritium operation in magnetic confinement experiments: results and underlying physics,*Plasma Phys. Control. Fusion* **41** (3A), A13-A46, 1999.

[13] Aymar R., Chuyanov V. A., Huguet M., Shimomura Y., ITER Joint central Team, ITER Home Teams, Overview of ITER-FEAT - The future international burning plasma experiment, *Nucl. Fusion* **41** (10), 1301-1310, 2001.

[14] Schumacher U., Status and problems of fusion reactor development, *Naturwissenschaften* **88** (3), 102-112, 2001.

[15] Hartmann D., Plasma heating, in *Summer University for Plasma Physics, September 17-21, 2001, Garching, ed. Könies A., Krieger K.* 185-200, 2001.

[16] Nedospasov A. V., Petrov V. G., Fidel'man G. N., Plasma convection in the poloidal limiter shadow of a tokamak, *Nucl. Fusion* **25**, 21-27, 1985.

[17] Endler M., Turbulent SOL transport in stellarators and tokamaks, *J. Nucl. Mater.* **266-269**, 84-90, 1999.

[18] Nedospasov A. V., Petrov V. G., Unipolar arcs as impurity source in tokamaks, *J. Nucl. Mater.*, **93** & **94**, 775-779, 1980.

[19] Behrisch R., Surface erosion by electrical arcs, *Physics of Plasma-Wall Interaction in controlled Fusion*, NATO asi Series, Series B: Physics **131**, 1984.

[20] Wolff H., Arcing in magnetic fusion devices, *Atomic and plasma-material interaction data for fusion, Suppl. to Nuclear Fusion* **1**, 93-107, 1991.

[21] Raizer Yu.P., Gas Discharge Physics, Springer, 1997.

[22] Höhn F., Multipactor discharges and their interaction with surfaces, *PhD Thesis*, 1997, in German.

[23] Latham R.V., High voltage insulation: The physical basis, Academic Press, 1981.

[24] Noterdaeme J.-M., Wesner F., Brambilla M., Fritsch R., Kutsch H.-J., Soell M., The ASDEX Upgrade ICRH antenna, *Fusion Eng. Des.* **24**, 65-74, 1994.

[25] Hofmeister F., Braun F., Wesner F., The RF system and matching procedure for ASDEX and ASDEX Upgrade, *Fusion Eng. Des.* **24**, 83-89, 1994.

[26] Wedler H., Wesner F., Becker W., Fritsch R., Vacuum insulated antenna feeding lines for ICRH at ASDEX Upgrade, *Fusion Eng. Des.* **24**, 75-81, 1994.

[27] Braun F., Hofmeister F., Wesner F., Becker W., Faugel H., Hartmann D., Noterdaeme J.-M., ICRF system enhancements at ASDEX Upgrade, *Fusion Eng. Des.* **56** (7), 551-555, 2001.

[28] Noterdaeme J.-M., Wukitch S., Hartmann D. A., Brambilla M., Braun F. et al., ICRF heating results in ASDEX Upgrade and W7-AS, *Fusion Energy* (Montreal, 1996) **3**, IAEA 335-342.

[29] Wesner F., Becker W., Braun F., Faugel H., Fritsch R. et al., ICRF operation during H-mode with ELMs: Development and Status at ASDEX Upgrade, *Fusion Techonlogy* (Lisbon, 1996), (C. Varandas and F. Serra ed.), North-Holland Publ., Amsterdam 537-540.

[30] Noterdaeme J.-M., Hartmann D. A., Stäbler A., Brambilla M. et al., Comparing high power ion cyclotron resonance frequency heating with neutral injection in ASDEX Upgrade: differences, similarities and synergies, *Fusion Energy* (Yokohama, 1998), IAEA.

[31] Arnold W., De Grassie J.S., Remsen D.B., Pivit E., Russel R., Braun F., Ferrite hybrid system for generator matching in the ICRF, *Fusion Techonlogy* (Marseille, 1998), (B. Beaumont, P. Libeyre, B. de Gentile, G. Tonon ed.), EURATOM-CEA, Cadarache, 427.

[32] Wesner F., Becker W., Brambilla M., Braun F., Faugel H. et al., Status and planning for ICRF at ASDEX Upgrade, *Radio Frequency Heating and Current Drive of Fusion Devices* (Brussels, 1998; J. Jacquinot, G. Van Oost and R.R. Weynants ed.) **22A**, Europ. Phys Society 13-16.

[33] Fast J. D., *Philips Res. Repts* **2**, 382, 1947.

[34] Lieberman M.A., A.J. Lichtenberg, Principles of plasma discharges and materials processing, John Wiley & Sons, Inc., 1994.

[35] Godyak V.A., Khanneh A.S., *IEEE Trans. Plasma Sci.* **14**, 112, 1986.

[36] Godyak V.A., *Soviet Radio Frequency Discharge Research*, Delphic Associates Inc. Falls Church VA, 1986.

[37] Godyak V.A., Piejak R. B., Alexandrovich B. M., *IEEE Trans. Plasma Sci.* **PS-19**, 660, 1991.

[38] Lisovskii V.A., Features of the α-γ transition in a low-pressure rf argon discharge, *Techn. Phys.* **43** (5), 526 - 534, 1998.

[39] Polozhiy K., α–γ transition in a high Q circuit, private communication, September 2002.

[40] R.H. Fowler, L. Nordheim, Proc. R. Soc. **119**, 173-181 (1928).

[41] Loew G. A. and Wang J.W., RF breakdown studies in room temperature electron LINAC structures, *SLAC-PUB-4647*, 1988.

[42] Loew G. A. and Wang J.W., RF breakdown and field emission, *SLAC-PUB-4845*, 1989.

[43] Tan J., *PhD Thesis*, *Université Pierre et Marie Curie* (Paris), 1989.

[44] Luong M., Safa H., Bonin B., et al., A comparison of enchanced field emission from broad surfaces in DC and RF regimes, *J. Phys. D: Appl. Phys.* **30** (8), 1248-1251, April 1997.

[45] Paulini J., Klein T., Simon G., Thermo-field emission and the Nottingham effect, *J. Phys. D: Appl. Phys.* **26**, 1310-1315, 1993.

[46] Fomenko V. S., Podchernyaeva I. A., Emission and adsorption properties of materials. Handbook, Atomizdat, Moscow 1975.

[47] Padamsee H., Knobloch J., The nature of field emission from microparticles and the ensuing voltage breakdown, *High Energy Density Microwaves, 1998* (AIP Conference Proceedings, edited by R. M. Phillips) **474**, 212, AIP, NY, 1999.

[48] Werner G. R., Betzwieser J. C., Knobloch J., Padamsee H., Qureshi M., Shipman J. E., Investigation of voltage breakdown caused by microparticles, *Particle Accelerator Conference, 2001 Chicago*, 1071-1073, IEEE, 2001.

[49] Latham R. V., Prebreakdown electron emission, *IEEE Trans, Elec. Insul.* **EI-18** (3), 1983.

[50] Halbritter J., On contamination on electrode surfaces and electric field limitations, **EI-20** (4), 1985.

[51] Cuneo M.E., The effect of electrode contamination, cleaning and conditioning on high-energy pulsed-power device performances, *IEEE Trans, Elec. Insul.* **6** (4), 469-485, 1999.

[52] Noer R. J., Electron field emission from broad-area electrodes, *Appl. Phys. A* **28**, 1-24, 1982.

[53] Mesyats G.A., Proskurovsky D.I., Pulsed electrical discharge in vacuum, Springer Series on Atoms and Plasmas, 1989.

[54] Gruszka H., Moscicka-Grzesiak H., Conditioning process of electropolished electrodes by field emission current in vacuum, *IEEE Trans. Elec. Insul.* **20** (4), 605-708, 1985.

[55] Charbonnier F. M., Strayer R. W., Swanson L. W., Martin E. E., Nottingham effect in field and T-F emission: heating and cooling domains, and inversion temperatures, *Phys. Rev. Lett.* **13** (13), 397-401, 1964.

[56] Niayesh K., Influence of electrode surface microstructure on the state of short vacuum gaps after interuption of high frequency currents, *J. Phys. D: Appl. Phys.* **33**, 2189-2191, 2000.

[57] Schmoll R., Analysis of interaction of cathode microprotrusions with low-temperature plasmas, *J. Phys. D: Appl. Phys.* **31**, 1841-1851, 1998.

[58] McCracken G.M., Stott P.E., Plasma-surface interactions in tokamaks, *Nucl. Fusion* **19** (7), 889-981, 1979.

[59] Karetnikov M.D, An origin of RF breakdown in vacuum, *Particle Accelerators* **57**, 189-214, 1997.

[60] Bruining H., Physics and applications of secondary electron emission, Pergamon Press Ltd, London, 1954.

[61] Thomas E. W., Particle induced electron emission, *Atomic and plasma-material interaction data for fusion, Suppl. to Nuclear Fusion* **1**, 79-91, 1991.

[62] Rusic D., Moore D., Manos D., Cohen S., Secondary electron yeilds of carbon-coated and polished stainless steel, *J. Vac. Sci. technol.* **(**20) (4), 1313-1316, 1982.

[63] Höhn F., Jacob W., Beckmann R., Wilhelm R., The transition of a multipactor to a low-pressure gas discharge, *Phys. Plasmas* **4** (4), 940-944, 1997.

[64] McDaniel E. W., Collision phenomena in ionized gases, edited by S. C. Brown, John Wiley & Sons, Inc., New York, London, Sydney, 1964.

[65] Brown S. C., Basic data of plasma physics, sec. edition, the M.I.T. press, 1966.

[66] Märk T. D., Dunn G. H. ed., Electron impact ionization, Springer-Verlag, Wien New York, 1985.

[67] Henrikse B. B., Keefer D. R., Clarkson M. H., Electromagnetic field in electrodeless discharge, *J. Appl. Phys.* **42** (13), 5460-5464, 1971.

[68] Raizer Yu.P., Shneider M. N., Yatsenko N. A., Capacitively coupled RF discharges, CRC Press, Boca Raton, London, Tokyo, 1995.

[69] Baity F. W., Barber G. C., Bobkov V., Goulding R. H., Noterdaeme J.-M., Swain D. W., *14th Topical Conference on Radiofrequency Power in Plasmas, Oxnard 2001*, AIP Conference proceedings **595**, AIP Press, Melville, NY 2001, 410-513.

[70] Shoji M., Sato M., Breakdown measurement of a capacitive radio frequency discharge with insulated electrode, *Appl. Phys. Lett.* **71** (23), 3362-3363, 1997.

[71] Lisovskiy V. A., Yegorenkov V. D., RF breakdown of low-pressure gas and a novel method for determination of electron-drift velocities in gases, *J. Phys. D: Appl. Phys.* **31**, 3349-3357, 1998.

[72] Raizer Yu.P., Shneider M.N., Near-electrode sheath dynamics, current anharmonicity and battery effect in asymmetrical, low-pressure radio-frequency discharges, *Plasma Sources Sci. Technol.* **1**, 102-108, 1992.

[73] Verplancke P., Langmuir probes at high frequencies in a magnetized plasma: theoretical and experimental plasma: a theoretical and experimental study, *Ph. D. Thesis, Max-Planck-Institut für Plasmaphysik*, 1997.

[74] Riemann K.-U., The Bohm criterion and sheath formation, *J. Phys. D: Appl. Phys.*, **24**, 493-518, 1991.

[75] Riemann K.-U., The validity of Bohm's sheath criterion in RF discharges, *Phys. Fluids B*, **4** (9), 2693-2695, 1992.

[76] Lieberman M. A., Analytical Solution for Capacitive RF sheath, *IEEE Trans. Plasma Sci.*, **16** (6), 638-644, 1988.

[77] Chodura R., Neuhauser J., Energy gain of plasma ions in a strong high frequency electric field between two target plates, *16th EPS Conference on Controlled Fusion and Plasma Physics* (Venice, 1989) **13B** III, 1089.

[78] Chen F. F., Introduction to Plasma Physics, Plenum, New York, London, 1984.

[79] Van Nieuwenhove R., Koch R., Van Oost G., Observation of plasma expulsion from a powered screenless ICRF antenna, *21st EPS Conference on Controlled Fusion and Plasma Physics* (Montpellier, 1994) **18B** II, 976.

[80] Bohm D., Characteristics of Electrical Discharges in Magnetic Fields (ed. Cuthrie A., Wakerling R.K.), Mc Graw-Hill, N.Y., 1949.

[81] D'Ippolito D. A., Myra J. R., Scrape-off layer profile modifications by convective cells, *Phys. Plasmas* **3** (2), 699-701, 1996.

[82] D'Ippolito D. A., Myra J. R., Rogers J. H., et al., Analysis of rf sheath interactions in TFTR, *Nuclear Fusion* **38** (10), 1543-1563, 1998.

[83] Bécoulet M., Colas L., Pécoul S. et al., Edge plasma density convection during ion cyclotron resonance heating on Tore Supra, *Phys. Plasmas*, **9** (6), 2619-2632, 2002.

[84] Riyopoulos S., Chernin D., Dialetis D.,Theory of electron multipactor in crossed fields, *Phys. Plasmas* **2** (8), 1995.

[85] Wesner F., Becker W., Multipacting in magnetic field, private communication, May, 2002.

[86] Bobkov V., Azarenkov M., Bizyukov A., Bobkov Vl., Noterdaeme J.-M., Wilhelm R., Development of coatings to improve RF voltage stand-off, *8th International Conference on Plasma Surface Engineering*, Garmisch-Partenkirchen, 2002.

[87] *http://www.kepcopower.com*, *http://www.kepcopower.com/specs/bopspecs.pdf.*

[88] *http://www.agilent.com*, *http://cp.literature.agilent.com/litweb/pdf/5962-9770E.pdf*, Product discontinued.

[89] Zhurin V.V., Kaufmann H.R., Robinson R.S., Physics of closed drift thrusters, *Plasma Sources Sci. Technol.* **8** (1), R1-R20, 1999.

[90] *http://www.niti.com*, *http://www.niti.com/oscilloscopes_pro.html.*

[91] *http://www.acqiris.com*, *http://www.acqiris.com/Products/DC265.html.*

[92] Terman F. E., Electronic and radio engineering, McGraw-Hill Book Company, Inc., 1955.

[93] Guo W., DeJoseph C. A. Jr, Time-resolved current and voltage measurements on a pulsed rf inductively coupled plasma, *Plasma Sources Sci. Technol.* **10**, 43-51, 2001.

[94] Endler M., Niedermeyer H., Giannone L., Holzhauer E., Rudyj A., Theimer G., Tsois N., ASDEX TEAM, Measurements and modelling of electrostatic fluctuations in the scrape-off layer of ASDEX, *Nucl. Fusion* **35** (11), 1307-1339, 1995.

[95] LaBombard B. et al., Cross-field plasma transport and main-chamber recycling in diverted plasmas on Alcator C-Mod, *Nucl. Fusion* **40** (12), 2041-2060, 2000.

[96] Antar G. Y., Devynck P., Garbet X., Luckhardt S. C., Turbulence intermittency and burst properties in tokamak scrape-off layer, *Phys. Plasmas* **8** (5), 1612-1624, 2001.

[97] Boedo J.A., Rudakov D., Moyer R., Krasheninnikov S. et al., Transport by intermittent convection in the boundary of the DII-D tokamak, *Phys. Plasmas* **8** (11), 4826-4833, 2001.

[98] Neuhauser J.et al., Transport into and across the scrape-off layer in the ASDEX Upgrade divertor tokamak, *Plasma Phys. Control. Fusion* **44**, 855-869, 2002.

[99] Mueller H.W., Bobkov V., Haas G., Jakobi M., Laux M., Maraschek M., Neuhauser J., Reich M., Rohde V., Schweinzer J., Wolfrum E., and ASDEX Upgrade Team, Profile and transport studies in the outer scrape-off-layer at ASDEX Upgrade, *29th conf. on Controlled Fusion and Plasma Physics*

[100] Sarazin Y., Ghendrih Ph., Intermittent particle transport in two-dimensional edge turbulence, *Phys. Plasmas* **5** (12), 4214-4228, 1998.

[101] Maslov V.I., Coherent structures at the plasma edge, private communication, May 2002.

[102] Krasheninnikov S., On scrape off layer plasma transport, *Phys. Lett. A* **283** (5-6), 368-370, 2001.

[103] D'Ippolito D. A., Myra J. R., Krasheninnikov S. I., Cross-field blob transport in tokamak scrape-off layer plasmas, *Phys. Plasmas* **9** (1), 222-233, 2002.

[104] Zohm H., Edge localized modes (ELMs), *Plasma Phys. Control. Fusion* **38**, 105-128, 1996.

[105] Suttrop W., The physics of large and small edge localized modes, *Plasma Phys. Control. Fusion* **42**, A1-A13, 1996.

[106] Porter G. D., Casper T. A., Moller J. M., Edge localized mode particle losses from the DII-D tokamak, *Phys. Plasmas* **8** (12), 5140-5150, 2001.

[107] Murmann H., Goetsch S., Salzmann H., and Steuer K.-H., The Thomson scattering systems of ASDEX Upgrade tokamak, *Rev. Sci. Instrum.* **63**, 4941-4943, 1992.

[108] Rohde V., Laux M., Bachmann P., Herrmann A., Weinlich M., and ASDEX Upgrade team, Direct measurements of the plasma potential in the edge of ASDEX Upgrade tokamak, *J. Nucl. Mater* **241-243**, 712-715, (1997).

[109] Golant V. E., Fedorov V. I., Radiofrequency methods of plasma heating in toroidal thermonuclear devices, Energoatomizdat, Moscow, 1986, in Russian.

[110] Stix T. H., Waves in plasmas, American Institute of Physics, New York, 1992.

[111] Juettner B., Cathode spots of electric arcs, *J. Phys. D: Appl. Phys.* **34**, R103-R123, 2001.

[112] Juettner B., and Kleberg I., The retrograde motion of arc cathode spots in vacuum, *J. Phys. D: Appl. Phys.* **33**, 2025-2036, 2001.

[113] Robson A. E., The motion of a low-pressure arc in a strong magnetic field, *J. Phys. D: Appl. Phys.* **11**, 1917-1923, 1978.

[114] Laux M., Drift of the cathode spots in a magnetic field, private communication, February 2003.

[115] Wukitch S. J. et al., ICRF operation experience on Alcator C-Mod, *Workshop on Outstanding Issues in ICRF Technology, Oxnard*, 2001.

[116] Carslaw H.S., Jaeger J. C., Conduction of heat in solids (second edition), Oxford University press, 1959.

[117] Lotz W., An empirical formula for the electron impact ionization cross section, *Z. Physik* **206**, 205-211, 1967.

[118] Janev R. K., Langer W. D., Evans K. Jr., Post D. E. Jr., Elementary processes in Hydrogen-Helium Plasmas, cross sections and reaction rate coefficients, Springer - Verlag Berlin Heidelberg New York London Paris Tokyo, 1987.

[119] Janev R. K., Smith J. J., Cross sections for collision processes of hydrogen atoms with electrons, protons and multiply charged ions, *Atomic and plasma-material interaction data for fusion, Suppl. to Nuclear Fusion* **4**, 1993.

Acknowledgements

Here I would like to thank everybody who made it possible to conduct and to complete this work. Especially I am grateful to Prof. Dr. R. Wilhelm and Dr. J.-M. Noterdaeme who gave me a chance to carry out this PhD project and supervised me during the work. I thank them for the scientific and the organizational discussions which helped me to find solutions in the situations where I could not see any way out at first.

I thank kindly Mrs. W. Sinz, Mrs. H. Martin and Mrs. C. Alberter for helping to solve a huge number of problems including organizational and personal ones.

I thank Dr. F. Wesner, Dr. D. Hartmann, F. Braun, J. Kneidl, H. Faugel, W. Becker and F. Hofmeister for the enormous help and support during design of the electrical part of the experimental device and during tests and operation of the device in the test facility and on ASDEX Upgrade.

I would like to thank separately G. Heilmaier and P. Leitenstern for working on the design of the experimental device. I thank G. Heilmaier, P. Leitenstern, G. Siegl and P. Angene for assembling the device and mounting it in the test facility and on the midplane manipulator of ASDEX Upgrade. I would also like to thank them for their patience when we found out that assembling and mounting the device more than once is required.

I thank M. Münich for the help with the capacitors which eventually solved the problem of the RF screening of the diagnostic cables in the experimental device. I would also like to thank other members of ECRH and NBI groups of the Technology division of IPP in Garching for their help in many situations.

I am grateful to Dr. J. Neuhauser for numerous discussions on physics and the ways of doing the things. I thank Dr. Rohde, Dr. H. Maier, Dr. H.-W. Müller and Dr. M. Laux for the discussions which helped to conduct the experiments on ASDEX Upgrade. I feel grateful to Dr. O. Gruber and the experimental leaders of ASDEX Upgrade for giving me the experimental time and coordinating the work with the diagnostics involved in the experiments. I thank the ASDEX Upgrade Team for technical support and for providing the data from different diagnostics as well as giving me answers on different questions about these diagnostics.

I thank Dr. D. Swain, Dr. R. Goulding and Dr. F. Baity from the Oak Ridge National Laboratory for cooperation and discussions about physics and the RF technology.

I would like to thank Dr. A. Lyssoivan for the discussion about the aspects of interaction of the RF power with the plasma.

I thank Dr. A. Bizyukov and Dr. V. Maslov from Kharkov National University for many helpful discussions about non-linear plasma physics. A lot of ideas which raised from these discussions were used in this thesis. I want to thank Prof. Dr. M. Azarenkov and Dr. I. Girka for promoting me as a promising post-graduate student and for the administrative support.

Especially I want to thank my father Dr. Valentyn Bobkov for his parental support and supervision, and also for the successful scientific cooperation. I want also to thank all my family, in particular my wife, for their support though the geographical distance between us was large most of the time.